POLITECNICO
MILANO 1863

SCUOLA DI INGEGNERIA INDUSTRIALE
E DELL'INFORMAZIONE

Executive Summary of the Thesis

Validation and Application of the Curle's Aeroacoustic Analogy

Laurea Magistrale in Mechanical Engineering - Ingegneria Meccanica

Author: Dario Colombo

Advisor: Prof. Paolo Schito

Co-advisors: Alberto Artoni, Francesco Fabio Semeraro

Academic year: 2020-2021

1. Introduction

Nowadays, the number of hybrid and full electric vehicles on the road is increasing, reducing the noise emitted by the drive train. In particular, for vehicles driving on highways at high speeds greater than 120 km/h, the aerodynamic noise dominates the other sources.
In the field of Computational Aero Acoustics (CAA), the sound emission and propagation can be predicted by using a DNS or an hybrid method. The latter allows a lower computational effort because the flow field is resolved with the most suitable methods and then an aeroacoustic analogy is applied to obtain the noise propagation to the far field. Therefore, the proposed work highlights a way to predict the acoustic pressure fluctuations by using an integral hybrid approach already implemented in OpenFOAM: the Curle's aeroacoustics analogy, described in section 2. The target of this study is to numerically validate the above mentioned analogy for relevant test cases.
The first test case is about the laminar flow across a square cylinder at $Re = 150$. This choice is driven by the simplicity of the geometry and by the large amount of references available in literature, see for instance [1], [5]. We then consider a turbulent flow across a rectangular cylinder with chord-to-depth ratio of 5 [4] at $Re = 4 \cdot 10^4$. Finally, an automotive application at $Re = 5.2 \cdot 10^5$ focusing on the side view mirror is proposed [2]. The numerical setup of the three test cases above mentioned is included in section 3.
The acoustic analysis of the cases is performed using the Curle's analogy that allows to extract the directivities, the frequencies and the intensity of the noise emitted from the source. The main results shown in section 4 have been compared with the ones found in literature.
The section 5 sums up all the results obtained pointing out main advantages and drawbacks of the aeroacoustic analogy.

2. Theory

The Curle's acoustic analogy that permits to predict the time dependent acoustic pressure fluctuations studied in this work is represented by the following equation:

$$p' = \frac{1}{4\pi}\frac{\boldsymbol{r}}{r^2} \cdot \left(\frac{\boldsymbol{F}}{r} + \frac{1}{c_0}\frac{d\boldsymbol{F}}{dt}\right), \tag{1}$$

where $\boldsymbol{r}$ is the distance vector between the source and the observer, r is the module of the vector distance $\boldsymbol{r}$, $\boldsymbol{F}$ is the force vector acting on the surface of the body, c_0 is the speed of sound and

p' is the acoustic pressure fluctuation.
This formulation is directly implemented in an OpenFOAM function and is valid under some hypothesis. These are:

- Isentropic flow in the region of interest.
- No volumetric sources.
- Retarded time is neglected.

The fact that the retarded time is not considered leads to an instantaneous propagation of the noise in the far field.
Although the presence of these limits, the analogy is able to give an initial guess of the acoustic results in terms of noise emission and propagation in the far field for each of the three different cases. With equation (1) we are able to extract the directivity patterns of the noise in order to classify the sound source as a dipole, monopole or quadrupole. Furthermore, the intensity of the noise is indicated in Sound Pressure Level (SPL) and calculated as follows starting from the acoustic pressure in time:

$$SPL = 20 \log_{10}(\frac{p'_{rms}}{p_{ref}}). \quad (2)$$

Qualitatively speaking, in section 4 the results are accurate and acceptable.

3. Numerical setup

The computational setup of the cases is described in this section distinguishing between the square cylinder test case 3.1, the rectangular cylinder test case 3.2 and the automotive application 3.3.
The physics of the simulations rely on the incompressible Navier-Stokes equations resolved by the finite volume discretization approach on which OpenFOAM is based. The computational time defined for each test case is long enough to reach the steady state condition while the time step permits to maintain the CFL < 1.

3.1. Square cylinder test case

The rigid square cylinder of side length $D = 3.2798 \cdot 10^{-5}\ m$ is immersed in a 2D laminar flow of free stream velocity $U = 68.6\ m/s$ with a Reynolds number of $Re_D = UD/\nu = 150$. The kinematic viscosity and the density are respectively set equal to $\nu = 1.5 \cdot 10^{-5}\ m^2/s$, $\rho = 1.205\ kg/m^3$ and the Mach number is $Ma = 0.2$. The computational domain is shown in figure 1 pointing out the adopted boundary conditions. On the cylinder the wall functions are used.

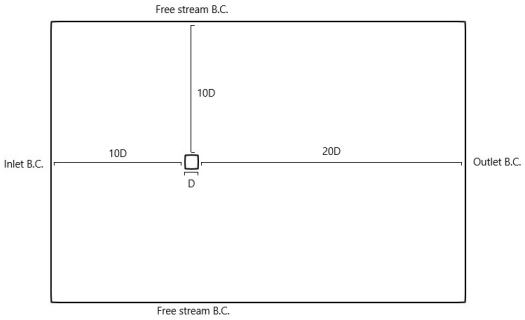

Figure 1: Flow domain for the square cylinder laminar case.

We considered two different grid resolutions in order to study the spatial convergence of the results. The coarser one is constituted by 644×368 cells while the finer one has double the cells both in x and y direction (1288×736). As we will see in the subsection 4.1 we adopted the coarser grid to perform the simulation.

3.2. Rectangular cylinder test case

The air flows across a rectangular cylinder with a chord-to-depth ratio $B/D = 5$ characterised by sharp edges and a smooth surface generating a 3D, turbulent and unsteady flow with an incidence $\alpha = 0$ and a turbulence intensity $Ti = 0.1\%$. The Reynolds number is equal to $Re = 4 \cdot 10^4$ obtained with a free stream velocity $U = 1\ m/s$, a kinematic viscosity $\nu = 1.5 \cdot 10^{-5}\ m^2/s$ and a density $\rho = 1.205\ kg/m^3$. The characteristic length is the one in the cross stream direction $D = 0.6\ m$ while in the spanwise the length L of the cylinder is equal to the chord B of the body itself as it's possible to see in figures 2 and 3.

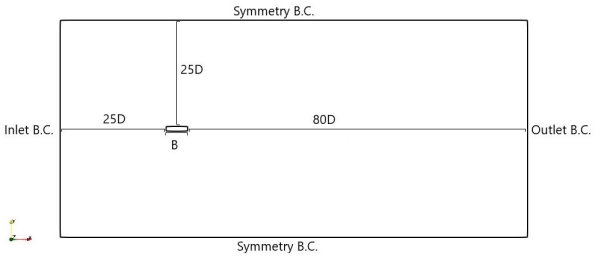

Figure 2: Computational domain in the x-y plane.

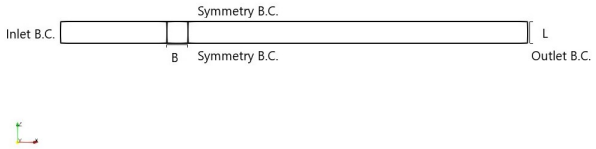

Figure 3: Computational domain in the x-z plane.

In this case the turbulence modeling plays a crucial role in the numerical setup being the flow highly turbulent. The strategy chosen is represented by a Detached Eddy Simulation (DES) with the kOmegaSSTDDES turbulence model.
A structured hexahedral grid is adopted to discretise the spatial computational domain. The 2D mesh in the x-y plane is constituted of 372×144 cells that are projected along the span-wise direction, where 24 cells are employed to uniformly obtain a 3D grid for a total of $1.216512 \cdot 10^6$. This choice permits to obtain the following y^+ values in the cross stream direction:

- $y^+_{max} = 41.43$;
- $\overline{y^+} = 18.28$.

3.3. Side view mirror test case

The flow travelling across the geometry is fully 3D, turbulent and unsteady with a velocity of $U = 39\ m/s$ ($Ma = 0.11$) that corresponds to a value at which the aerodynamic noise becomes dominant. The kinematic viscosity is set to be $\nu = 1.5 \cdot 10^{-5}\ m^2/s$ and, together with the characteristic length of the side view mirror $D = 0.2\ m$, we obtain a Reynolds number of $Re_D = 5.2 \cdot 10^5$ with a density of $\rho = 1.225\ kg/m^3$. The turbulence is modeled with a DES simulation and a kOmegaSSTDDES technique.

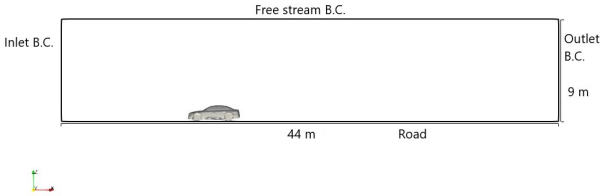

Figure 4: Computational domain for the automotive case in the x-z plane.

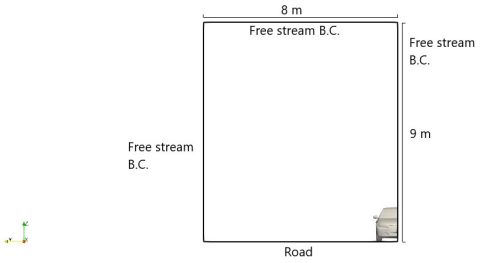

Figure 5: Computational domain for the automotive case in the x-y plane.

Although the geometry is half of a vehicle (see figures 4 and 5), we concentrate on the side view mirror shown in figure 6.

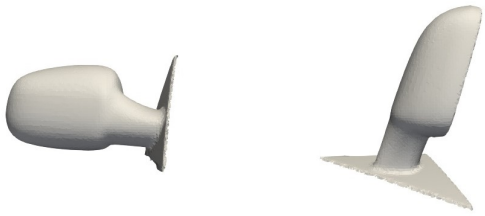

(a) Front view (b) Side view

Figure 6: Side view mirror geometry.

The grid for this case is constructed using the tool *snappyHexMesh* available in OpenFOAM. A coarse, background mesh is firstly generated getting finer and finer towards the geometry of the car with different levels of refinement for different components of the vehicle allowing to have a total number of cells equal to $2.200678 \cdot 10^6$. We set a coarser grid in the underbody while for the side view mirror the resolution level is the highest. This choice has been made considering that the flow passing under the vehicle is not affecting the one crossing the upper part of the car.
Concerning the y^+ for the side view mirror we have a maximum and a mean value respectively equal to $y^+_{max} = 122.18$ and $\overline{y^+} = 32.38$.

4. Results and discussion

In this section the main CFD and acoustics results obtained with the Curle's aeroacoustic analogy are shown with a particular focus on the directivity of the sound propagation and its intensity.

4.1. Square cylinder test case

The unsteady laminar flow crossing the square cylinder is characterized by separation starting from the corners of the geometry. For the considered flow, this phenomenon generates vortexes in the wake of the body obtaining the so called Von Karman street that can be seen in figure 7.

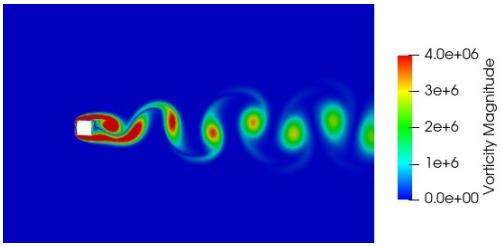

Figure 7: Instantaneous vorticity contours ($\boldsymbol{\omega} = \nabla \times U$) obtained at $TU/D = 250$.

Case	St	Cl_{rms}	Cd_{mean}
Ali et. al [1]	0.16	0.285	1.47
Coarser grid	0.161	0.278	1.458
Finer grid	0.16	0.278	1.459

Table 1: Grid convergence study.

Table 1 highlights that the aerodynamic quantities obtained with the two different strategies are the same, thus, in order to save computational time, the coarser grid is chosen for the acoustic analysis.
The sound propagation in the far field obtained exploiting the Curle's aeroacoustic analogy implemented in OpenFOAM is shown in the following figures:

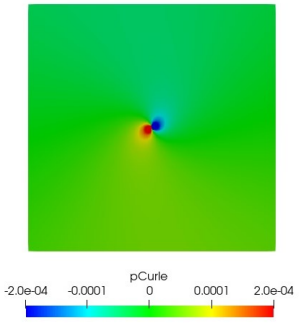

Figure 8: Contours of instantaneous acoustic pressure ($\widetilde{P} = p'/(\rho U^2)$) at $TU/D = 250$.

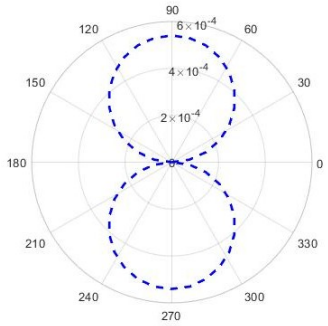

Figure 9: Directivities of root mean square sound pressure ($\widetilde{P}_{rms} = p'_{rms}/(\rho U^2)$) at the Strouhal frequency for the square cylinder test case.

Figure 9 shows that the noise propagation is instantaneous and the sound reaches the observers as soon as it is emitted from the source because the retarded time is neglected in the model. This could be one of the main reasons, among others, for which the reference Ali et. al [1] is not matched. The dipole shown in figure 9 is obtained by placing 45 probes along a circumference of radius $75D$ centered in the acoustic source, i.e. the square cylinder.

4.2. Rectangular cylinder test case

Being the flow turbulent, the phenomenon is characterized by the non periodic and chaotic shedding of the vortices not pointing out the Von Karman street as it's possible to see in figure 10.

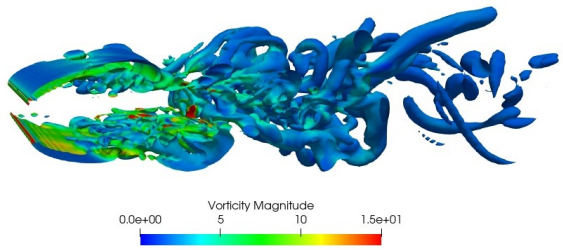

Figure 10: 3D velocity field plotted over vorticity contours at $TU/D = 800$.

Study	St	Cl_{rms}	Cd_{mean}
Bruno et. al [4]	0.112	0.73	1.03
Present work	0.1136	0.96	1.10

Table 2: Rectangular test case flow quantities.

In the table 2 we compare the flow results with the reference from the literature. Although the computed drag coefficient matches the reference, the lift coefficient is instead strongly sensitive to set-up and modelling of the simulation, leading to a significant underestimation of the numerical predictions [3].
The strategy adopted to measure the sound directivity shown in figure 11 pointing out the dipole is the same used also for the square cylinder test case.

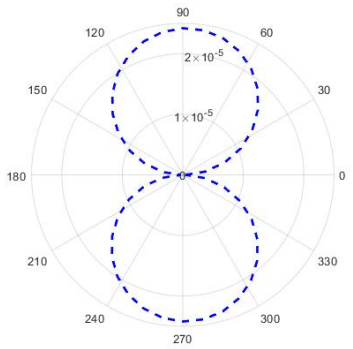

Figure 11: Directivities of root mean square sound pressure ($\widetilde{P}_{rms} = p'_{rms}/(\rho U^2)$) at the Strouhal frequency for the rectangular cylinder test case.

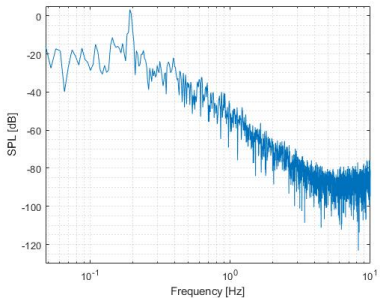

Figure 12: SPL measured by the probe placed at $75D$ from the acoustic source in the cross stream direction ($90deg$).

By looking at figure 12 we can notice the dominant frequency of the sound that is totally correlated to the frequency of the lift. The SPL shown in the figure are affected by the non completeness of the model, being the volume source neglected.

4.3. Side view mirror test case

The main sources of vortexes, as shown in figure 13 are represented by the tires and the side view mirror which are also the main sound sources. As already mentioned, we'll concentrate on the noise emitted from the side mirror component.

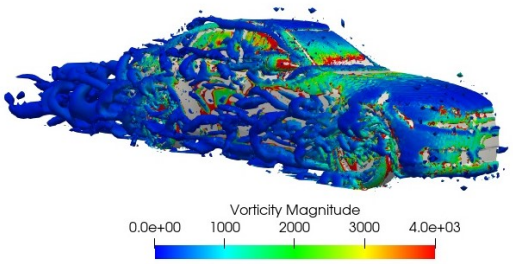

Figure 13: Vorticity magnitude of the automotive test case plotted over vorticity contours at $TU/D = 497.25$.

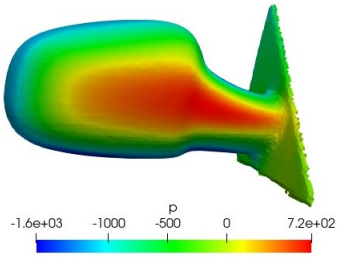

Figure 14: Pressure acting on the side view mirror in the DES configuration at $TU/D = 497.25$.

Concerning the distribution of the pressure on the side view mirror shown in figure 14 we can appreciate the high pressure zone on the part directly exposed to the flow and the low pressure area in the wake where the majority of the vortexes arise. The main flow quantities related to the side view mirror are shown in the following table:

Study	St	Cl_{rms}	Cd_{mean}
Reference [2]	≈ 0.2	–	0.428
Present work	≈ 0.123	0.284	0.299

Table 3: Comparison of the results with the paper of J. Ask and L. Davidson [2].

The misalignment between the values mentioned in the table 3 is probably due to the presence of half of the vehicle and due to the different side view mirror geometry with respect to the reference.
In this particular case, the dipole is not perfectly aligned with the cross stream direction because the flow is not perpendicular to the surface of the body but, in any case, the Curle's model is still able to predict the correct pattern propagation, refer to figure 15.

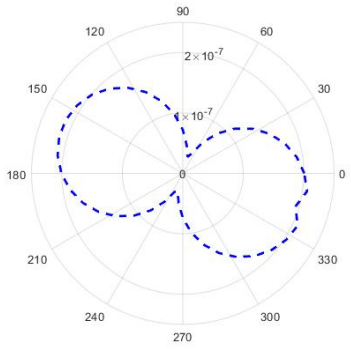

Figure 15: Directivities of root mean square sound pressure ($\widetilde{P}_{rms} = p'_{rms}/(\rho U^2)$) at the Strouhal frequency for the side view mirror test case.

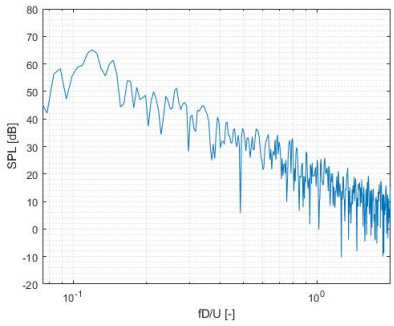

Figure 16: SPL measured in the wake of the side view mirror.

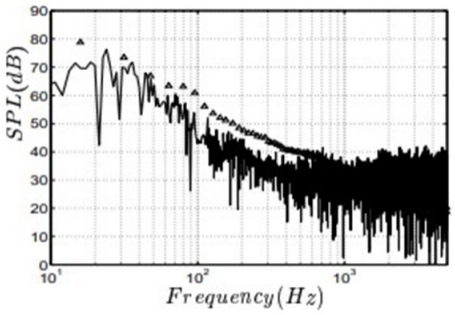

Figure 17: Sound Pressure Level measured at the probe M10 in the reference of J.Ask and L.Davidson [2].

Comparing figure 16 with the results proposed by J.Ask and L.Davidson in figure 17 we can notice that they are in agreement because the acoustic model implemented is the same except for the viscous forces that we are neglecting.

5. Conclusions

We have applied the Curle's aeroacoustic analogy implemented in OpenFOAM to different cases in order to validate the model and predict the sound emission and propagation in the far field. This model is easy to be used since it is directly incorporated into an OpenFOAM's function and also gives results that are qualitatively correct in terms of directivity, decay of the sound and emitted frequencies.
On the other hand, the results are not in total agreement with the literature pointing out some important limits in the model. The first limit is that the model doesn't consider the retarded time in the noise prediction, leading to an instantaneous propagation of the sound. The model also neglects the volume source of the sound constituting the second big limit of the Curle's aeroacoustic analogy implemented in OpenFOAM. Both these drawbacks lead to a non conformity with the data available in literature, especially in the turbulent cases where the volumetric sources cannot be neglected.
In conclusion, we can say that that the Curle's aeroacoustic analogy taken into consideration in this study is a good methodology, especially in terms of emitted frequencies, to give an initial guess of the noise emission and propagation but needs further improvements to be completely accurate and reliable. Therefore, one of the future works can be based on the modification of the

already existing Curle's analogy in OpenFOAM with the aim to make it much more accurate by adding the contributions of the retarded time and the volume source. We also plan to inquire different side view mirror geometries to quantify if it is possible to reduce the noise induced by the side view mirror itself. Other important steps, not included in the thesis, could be experimental validations of the proposed results.

6. Acknowledgements

First of all I would like to thank professor Paolo Schito that gave me the opportunity to do this thesis work in the field of aeroacoustics. Furthermore, I would like to thank PhD. candidates Alberto Artoni and Francesco Fabio Semeraro for their huge help and availability in giving prompt feedbacks with their knowledge in every kind of problem that I had to face.
Finally, I would like to thank my family and my girlfriend Cristina for their continuous support during my entire education even in the darkest periods, my university colleagues and my friends.

References

[1] Mohamed Sukri Mat Ali, J. Doolan, and Vincent Wheatley. The sound generated by a square cylinder with a splitter plate at low reynolds number. 04 2011.

[2] J. Ask and L. Davidson. The near field acoustics of a generic side mirror based on an incompressible approach. *Fluid Dynamic Center - VOLVO CAR CORPORATION, Göteborg, Sweden*, 2005.

[3] L. Bruno, M.V. Salvetti, and F. Ricciardelli. Benchmark on the aerodynamics of a rectangular 5:1 cylinder: an overview after the first four years of activity. 2014.

[4] Luca Bruno, Davide Fransos, Nicolas Coste, and Arianna Bosco. 3d flow around a rectangular cylinder: A computational study. *Journal of Wind Engineering and Industrial Aerodynamics*, 98, 11 2009.

[5] O. Inoue, W. Iwakami, and N. Hatakeyama. Aeolian tones radiated from flow past two square cylinders in a side-by-side arrangement. 04 2006.

POLITECNICO
MILANO 1863

SCUOLA DI INGEGNERIA INDUSTRIALE
E DELL'INFORMAZIONE

Validation and Application of the Curle's Aeroacoustic Analogy

Tesi di Laurea Magistrale in
Mechanical Engineering - Ingegneria Meccanica

Author: **Dario Colombo**

Student ID: 946090
Advisor: Prof. Paolo Schito
Co-advisors: Alberto Artoni, Francesco Fabio Semeraro
Academic Year: 2020-21

Abstract

The noise emitted by a motor vehicle is mainly due to the internal combustion engine, aerodynamics and tire-road contact. Nowadays the number of hybrid and full electric vehicles on the road is increasing, thus the noise emitted by the drive train is no longer a significant contribution. For vehicles driving on highways at high speeds, the aerodynamic noise dominates the other sources. Many research activities rely on Computational Aero Acoustics (CAA) for aeroacoustics predictions, leading to the minimisation of the noise induced by fluids for better comfort and designs. The target of this work is to numerically validate the Curle's analogy implemented in OpenFOAM for relevant test cases. The first test case is about the laminar flow across a square cylinder at $Re = 150$. It is then considered a turbulent flow across a rectangular cylinder at $Re = 4 \cdot 10^4$ with chord-to-depth ratio of 5. The analysis of the test cases is based on extracting directivities, frequencies and intensity of the sound emitted by the source flow field. The results have been compared to studies found in the literature. Based on the former comparison, an automotive application $Re = 5.2 \cdot 10^5$ is then proposed. The Curle's analogy is used to measure and study the noise emitted by the interaction of the vehicle with the wind. In order to solve the acoustic sources, the flow field is computed with incompressible and unsteady CFD simulations, using a DDES turbulence model.

Keywords: Vehicle aerodynamics, Aeroacoustic, CAA, CFD, Curle's aeroacoustic analogy

Abstract in lingua italiana

Il rumore emesso da un veicolo è principalmente dovuto al motore a combustione interna, all'aerodinamica e al contatto degli pneumatici sulla strada. Oggigiorno un numero sempre maggiore di veicoli ibridi o completamente elettrici è presente sulle strade e di conseguenza il contributo del motore endotermico sul rumore complessivo emesso dal veicolo non sarà più quello principale. Per i veicoli che viaggiano sulle autostrade ad alta velocità il rumore generato dall'aerodinamica del veicolo stesso domina sulle altre fonti. Molte attività di ricerca si basano sull'aeroacustica computazionale (CAA) per predire il rumore generato e minimizzarlo allo scopo di migliorare il comfort dei passeggeri. L'obiettivo di questa tesi è di validare numericamente l'analogia di Curle implementata in OpenFOAM per dei validi casi test. Il primo caso riguarda un cilindro a base quadrata investito da un flusso laminare a $Re = 150$. Successivamente abbiamo considerato un cilindro a base rettangolare con rapporto chord-to-depth uguale a 5 attraversato da un flusso turbolento a $Re = 4 \cdot 10^4$. Lo studio di questi casi test si concentra sull'estrazione delle direttività, delle frequenze e dell'intensità del suono emesso dalla sorgente acustica. I risultati sono stati confrontati con quanto presente in letteratura. Il passo successivo è stato quello di applicare quanto riscontrato in questi due test su un caso automotive a $Re = 5.2 \cdot 10^5$. L'analogia di Curle è utilizzata per misurare e studiare il rumore emesso dall'interazione del vento con il veicolo. Con l'obiettivo di predire il suono emesso dalle sorgenti, il campo fluidodinamico è ricavato da simulazioni incomprimibili e instazionarie utilizzando il modello di turbolenza kOmegaSSTDDES.

Parole chiave: Aerodinamica del veicolo, Aeroacustica, CAA, CFD, Analogia aeroacustica di Curle

Contents

Introduction

In the recent years, more understanding and concern has been given to noise pollution. The European Union has issued in several reports the problem focusing on the source of noise and on the effects on people and animals. Furthermore, most of the Europeans living in major urban areas are exposed to high noise levels [14].
In urban areas, most of the noise comes from transportation. In particular the noise from vehicles is generated mainly by the engine noise, the wind noise and the rolling noise, depending at which speed the vehicle travels. The engine noise is the noise generated by the engine and it is important both at low speeds and at high speeds. However, in recent years the trend is to replace internal combustion engines with electrical ones, leading to high reduction in the emitted engine noise. The rolling noise is the one associated to tyres rolling on the road. Finally, the most important noise at high speed is the one induced by the wind and is mainly generated by the A-pillar, the tyres and the side view mirror. By looking at figures 1 and 2 it is possible to notice that the main source of sound at low speed is the rolling noise while at high speed the aerodynamic noise becomes dominant.
The significance of the aeroacoustic noise for the exterior noise of motor vehicles has been known for a long time.

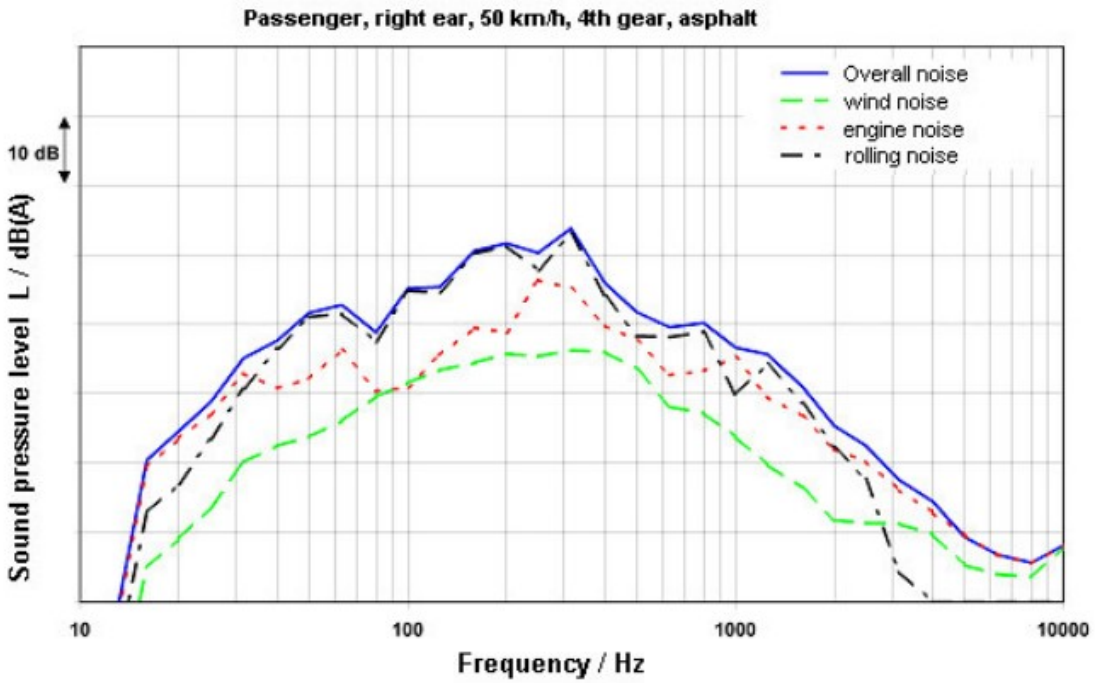

Figure 1: Overall noise and noise components of an upper middle-class passenger vehicle at $U = 50\ km/h$ [9].

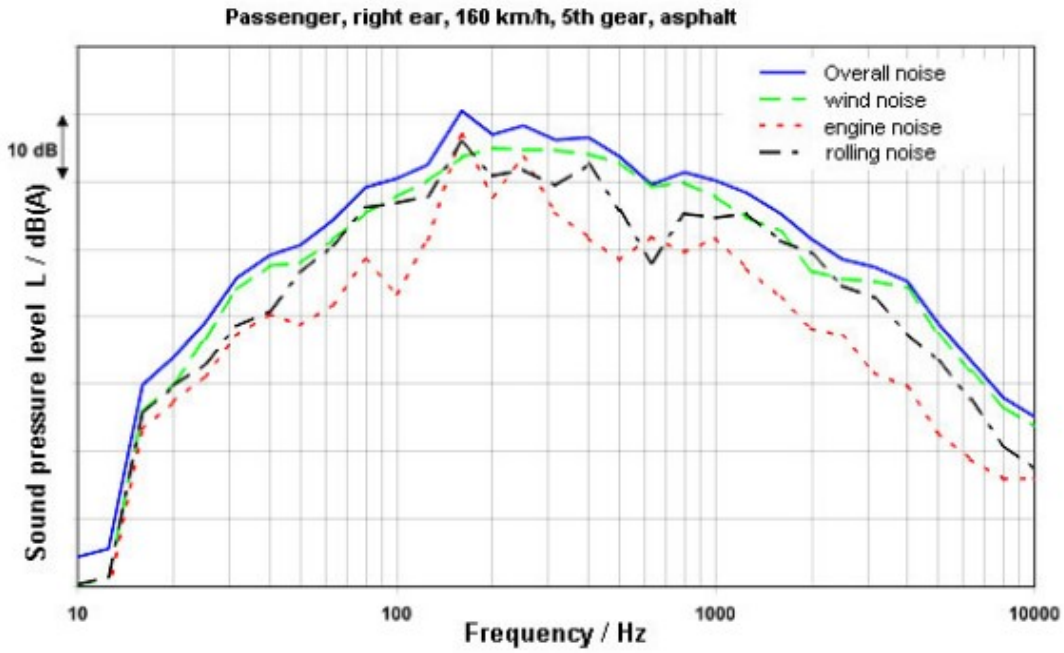

Figure 2: Overall noise and noise components of an upper middle-class passenger vehicle at $U = 160\ km/h$ [9].

A pioneering engineering work is the pass-by tests performed in [6] with the aim to address specifically the phenomenon. Aerodynamic noise researchers originally attempted acoustic measurements in conventional wind tunnels. However, external tests suffer often from other source of noise or require large space: a more controlled environment was required. Indeed, due to the strong interference between the wind tunnels' inherent noise and the noise induced on the body, the measurements are hard. The necessity of facilities led to the development of anechoic wind tunnels, able to address experimentally the aeroacoustic problem. Anechoic wind tunnels combine the presence of panels to minimize the reflections and particular strategies to reduce the noise source from the fan.

Figure 3: Royal NLR Anechoic wind tunnel which shows a particular use sound absorbing materials [22].

However, leading experimental campaigns is often very expensive and there aren't many anechoic facilities. Moreover, conventional transition from wind tunnel to anechoic wind tunnels are not straight forward and there are not many facilities.
The first work of Lighthill in 1954 gave rise to the development of continuous models to understand aeroacoustics. Lighthill derived an inhomogeneous exact wave equation from the equations describing the fluid flow. Furthermore, he highlighted how the aeroacoustic noise is mainly composed by monopoles, dipoles and quadrupoles acoustic sources, see figure 4. The monopole sound field is generated by the mass flux through a surface. Dipoles are obtained from the reaction of the surface to the force exerted from the fluid flow to the surface itself while, quadrupoles mechanism is due to fluctuating stresses in the fluid.

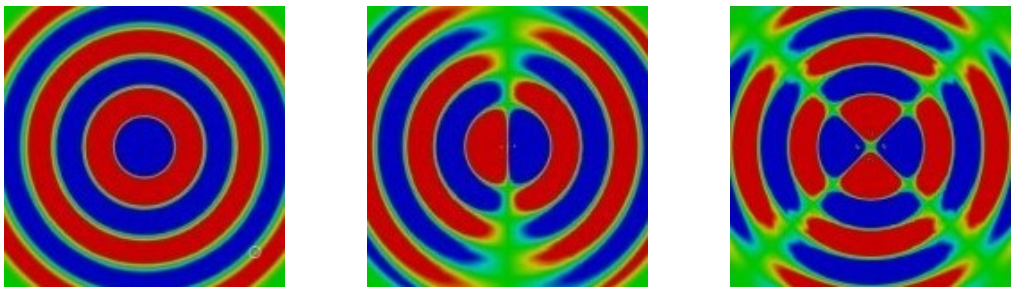

(a) Monopole. (b) Dipole. (c) Quadrupole.

Figure 4: Acoustic sources and their propagation patterns. Images obtained with SPEED [23].

A better intuition of the problem has also been given by Möhring, that analytically relates the quadrupole term to vorticity for low Mach flows. This is physically related to the stretching and compression of the eddies. Where there are vortexes, there is sound. For more details, see [12], [29], [24].
The Computational Aero Acoustics (CAA) aims to provide numerical tools to best address the noise emission problem. Noise is generated via (usually small) pressure fluctuations. The hardest challenge in CAA is to be able to correctly predict the pressure fluctuations, that might have the same order of magnitudes of the local truncation error or round off errors. For more details see the review of [20].
The pressure fluctuations generating noise can be assessed with a direct (DNS) or hybrid approaches. Both of them provide a methodology to predict the sound emission and propagation in the far field. DNS methods solve all the scales in the entire domain: this approach leads to high mesh requirements and inevitably to high computational costs.
Hybrid-approaches allow to compute the main sound sources by solving the flow field with the most suitable Computational Fluid Dynamics (CFD) methods. Then, by applying convenient strategies the acoustic field is propagated. One of the possible strategies to propagate the sound sources is through the application of aeroacoustic analogies. Lighthill proposed the first acoustic analogy transforming the compressible Navier–Stokes equation into an inhomogeneous wave equation. One of the approaches is to solve then the Lighthill's acoustic wave equation employing for instance finite element methods, see [17]. This approach is computationally expensive because the solution is computed on the whole acoustic domain, which in general is large, but it provides an accurate solution and it is still less expensive then perfoming DNS. Another approach consists in computing the analytical solution of the Lighthill's equation under certain assumptions employing suitable Green's functions. This leads to the integral formulation of the Lighthill's analogy. The integral is then computed via proper quadrature methods and provides the solution

on few points. Usually it is employed in experiments and the observation points coincide with the probe microphones employed for the measurements. One of the most important limits of the Lighthill's integral analogy, is that no solid boundaries are taken into account. Curle extended the Lighthill's theory including the effects of solid surfaces at rest that are equivalent to a surface dipole distribution. Then, Ffowcs Williams and Hawkings further developed the integral solution towards accounting for arbitrary moving bodies in the source domain [33]. The workflow of hybrid aeroacoustics methods involves three steps:

- perform unsteady flow simulations on a computational domain;
- compute the acoustic sources;
- simulate the acoustic field.

The main focus of this study will be on flow at low Mach number. This avoids a lot of issues, like for instance shockwaves occurring in the transonic regime, which would require more detailed studies. It also best fits the context of the employed numerical tools, which is the Curle's analogy. Indeed, low Mach number applications have huge disparity of scales between flow structures and acoustic wavelengths. This thesis aims to validate the Curle's aeroacoustic analogy implemented in OpenFOAM in order to provide an initial understanding of the model by applying it to different test cases.

Aerodynamic noise on bluff bodies at low Mach. Flow-induced sound is one of the engineering problems associated with bluff bodies. Therefore, it is very important to have a good understanding of the physics of the noise induced by the flow around bluff bodies so its reduction can be made using practical methods [1].
The sound sources result from the generation of fluid oscillations that may occur as a result of a turbulent flow, and/or a flow discontinuity that evolves into a periodically shed unstable free shear layer. in the latter case, a distinct tone is radiated. The extension done by Curle on the Lighthill's work showed that the surface pressure fluctuations induced by the shear layer shedding increases sound intensity by a factor of Ma^{-2}, where Ma is the Mach number, when compared with the sound generated from the turbulent flow. Thus, the unsteady aerodynamic forces acting on a solid body generate a significant sound at low Mach numbers [1].

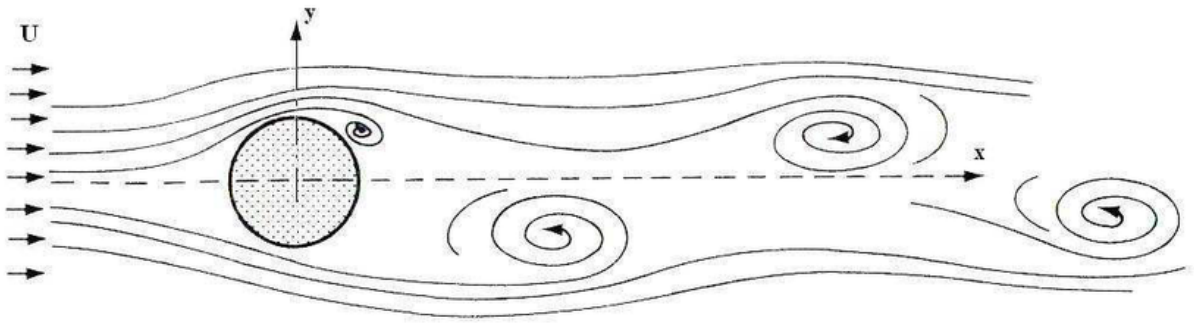

Figure 5: Vortex shedding across a cylindrical bluff body [16].

The bluff bodies suffer of high levels of unsteady aerodynamic force when the shear layers become unstable beyond the critical Reynolds number ($Re_c = 49$ for a circular cylinder [43] and $Re_c = 47$ for a square cylinder [38]). Furthermore, for a fixed flow condition, the aerodynamic forces and the frequency of the vortexes are mainly influenced by the geometry of the bluff bodies [1]. The study of bluff bodies with sharp edges is of interest as the flow separation point is fixed, while for a circular cylinder the flow separation point changes periodically around the base of the cylinder.
At low Reynolds the main force generating the noise is the lift force. Reducing lift fluctuations will reduce the noise emitted by the bluff body. One of the possible strategies to reduce the lift fluctuations is to add a splitter on the wake of the cylinder. This has also the effect to delay the vortex formation and thus reducing the induced noise, see for instance [1].

A-pillar noise. Pillars are vertical supports on a vehicle. They are located around all the glass on an automobile and they are important for holding glass in place and adding structural integrity to a vehicle, primarily the roof, see figure 6.

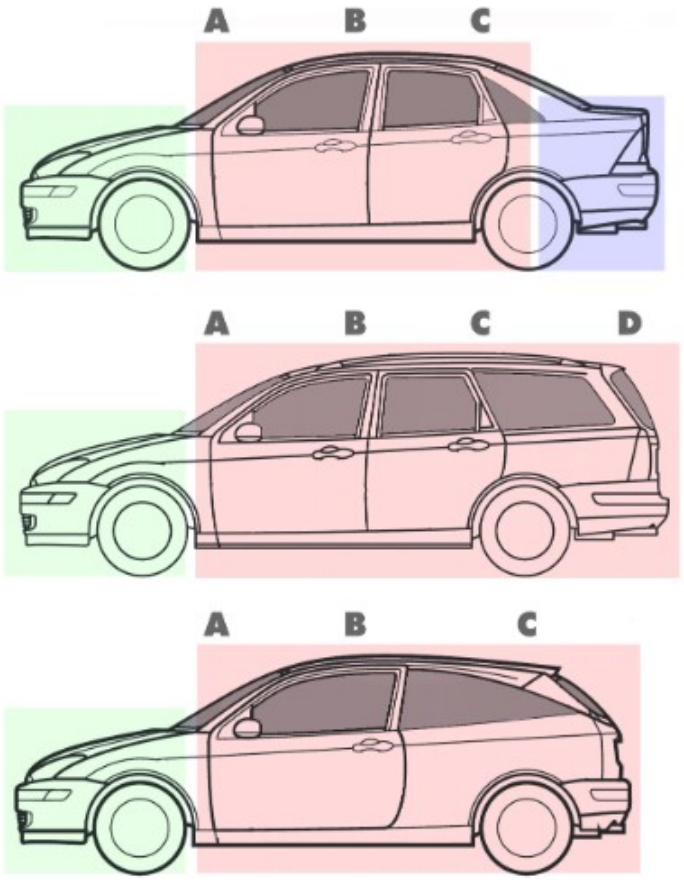

Figure 6: Pillars for different types of vehicle [15].

The "A" pillar holds the windshield in place, see figure 8.

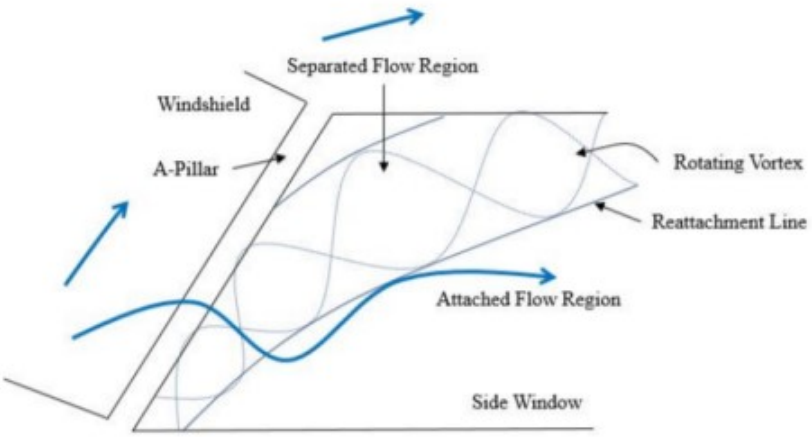

Figure 7: Demonstration of typical vortex structure around the A-pillar [13].

The design of the A-pillar has a marked effect on the generation of aerodynamic noise. Close to the A-pillar, at high speeds, high level of turbulence and pressure fluctuations can be observed. This structural component determines the volume and shape of the separation vortex on the side window, which can also influence noise emission from the exterior mirror. Sharp-edged A-pillars are acoustically more unfavorable under yaw conditions than rounded ones, see [9]. Furthermore, from the aerodynamic point of view, sharp edges increase the drag coefficient and the costs over the life cycle of the car. This has also been confirmed by the industry, where in the last decades a shift to rounded edge A-pillar has happened.

Tyre noise aeroacoustic mechanism. Another important source of aeroacoustic noise are the tyres. The noise generation mechanism involves both vibroacoustics and aeroacoustics. The main effects in tyre noise generation are:

- Air pumping.
- Horn effect.
- Turbulence noise generation

The air pumping effect generates noise due to the squeezing of the grooves. The air is imprisoned inside the grooves, then the treads are compressed on the road, and finally the air is suddenly released.

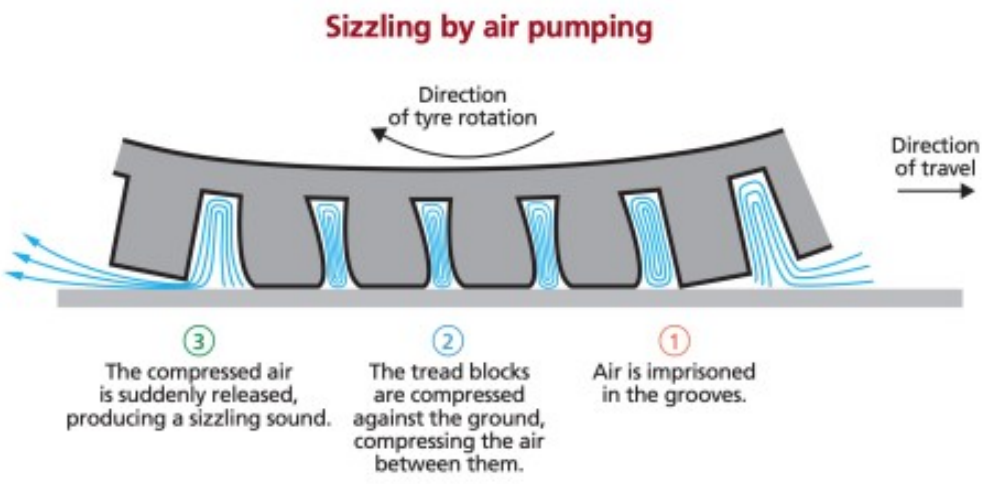

Figure 8: Air pumping mechanism steps [22].

This generates a hiss that then is amplified by the horn effect. The horn effect is due to the geometry of the tyre and the road that create a ”horn” that amplifies the generated noise, see figure 9.

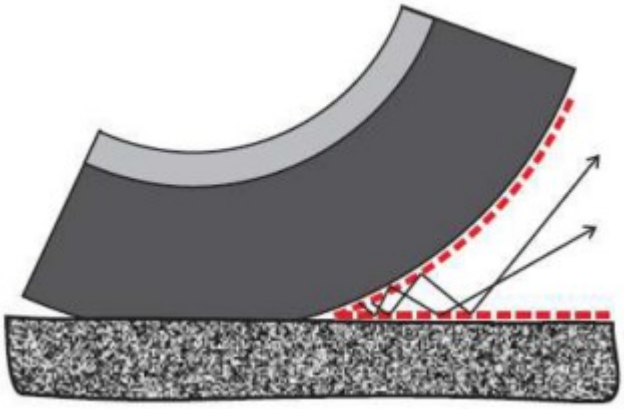

Figure 9: Horn amplification [22].

Finally, the presence of turbulence, and the inherently noise related to vortexes also affects the noise induced by the tyre. The wake generated by the separation of the boundary layer from the wheel introduces high energy in the shear layer. Two shoulder vortexes are formed while, the contact patch on the ground detaches two other vortexes. However, if an isolated tyre is rotating, an horseshoe vortex cannot form, as the boundary layer near the ground does not separate in front of the wheel.

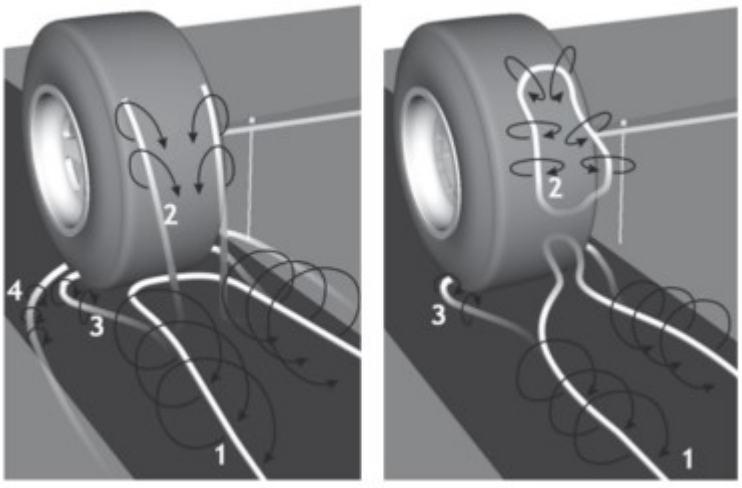

Figure 10: Difference between a rotating wheel and a fixed one [22].

The vortexes are one of the primary sources contributing to tyre noise so that the wake and the turbulence will significantly contribute to tyre aeroacoustics at high speeds.

Aerodynamic noise induced by side view mirror. The automotive industry is really interested in the sound generation phenomena induced by the wind and one of the most important contributor to the flow-induced noise is the flow around the side view mirror due to its bluff-body character [8]. The main purpose of the side view mirror is to provide visibility of the back of the car to the driver. This functionality has to be preserved in the aeroacoustic design of new solutions.
The usual shape of the side view mirror can be seen as a wall mounted bluff body. The noise is mainly generated by the vortexes that have a tonal character (whistling). Some vortex generators are often placed in front of the noise source with the aim to interfere with the periodicity of the vortexes [9], see figure 11.

Figure 11: Vortex generator to avoid tonal noise in the area of two exterior mirrors of production vehicles [9].

Furthermore, noise excitation can also be reduced by positioning the mirror in zones of lower flow speeds since the general trend of the tonal frequencies with increasing free stream velocity scales as $U^{3/2}$.
The noise induced by the side view mirrors is an important noise source. One solution to remove the noise could be to completely remove the side view mirror and introduce cameras to help the driver. However, regulations are very strict and it does not seem to be a solution that finds enough discussions, both in literature or on the media.

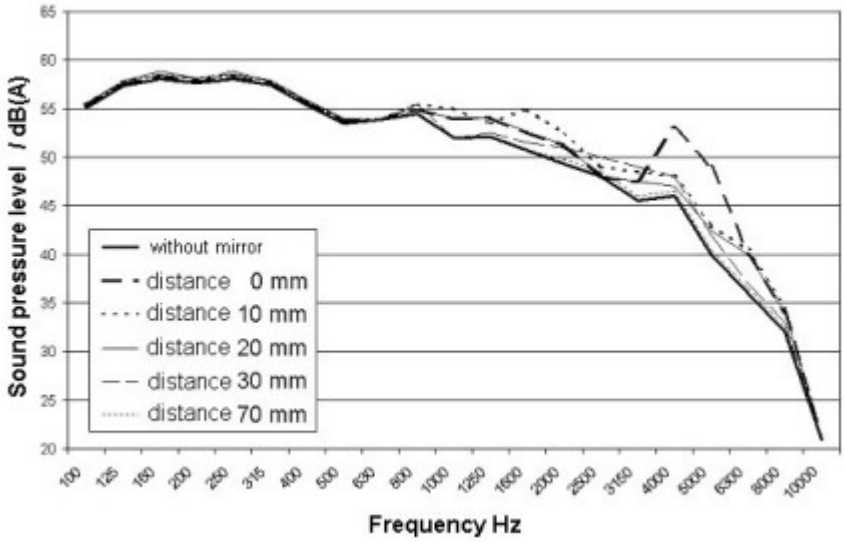

Figure 12: Influence of the distance of the left exterior mirror from the vehicle surface to the sound pressure level at the driver's left ear [9].

Most of the analysis performed on side view mirrors are focused on only the side view mirror itself, avoiding the effect of the whole car. Although this approach is cheap, it might lack of precision. In this work, the noise induced by the forces on a side view mirror generated by the CFD of the entire car are inquired.
This thesis is structured as follows. In chapter 1 will be introduced the basic theory regarding the CFD numerics and the state of the art related to hybrid modeling of aeroacoustic sound used to predict the emitted noise from a source. The first application case is introduced in chapter 2 and it is about a laminar flow crossing a square cylinder. The choice of this test is driven by the simplicity of the geometry and by the big amount of references available in literature with which compare the results [1], [18]. Chapter 3 analyzes the turbulent flow test case in which the air is passing across a rectangular cylinder [3]. Many researches regarding this application available in literature are gathered together in an extended platform focused on the Benchmarck on Aerodynamics of a Rectangular Cylinder. Chapter 4 is about an automotive application with a particular focus on the side view mirror. This geometry has been the subject of several studies present in literature. Hold [11] and Siegert [35] conducted both experimental and numerical investigations based on URANS simulations to predict sound generation and propagation at the Reynolds number of $Re = 7.066 \cdot 10^5$. They analyzed three different grids and used an aeroacoustic analogy based on the surface pressure and its temporal derivative to evaluate the radiated sound from the side view mirror. Another study was conducted by Rung et

al. [32] at $Re = 5.2 \cdot 10^5$ who focused on the differences in noise generation obtained with a URANS and a DES modeling technique [2].
In each of the above mentioned cases, the CFD simulation is performed validating the results with the literature and then, the Curle's analogy is applied to predict the noise propagation in the far field. Therefore, in each chapter are shown both the fluid dynamic results and the acoustic ones.
Chapter 5 sums up all the results obtained in the different test cases simulations pointing out advantages and drawbacks of the Curle's model implemented in OpenFOAM. In the same chapters are described also the future works and developments that can be carried out starting from this thesis work.

1 | Theory

In this chapter, a brief review of the involved fluid dynamics theory is done, with a focus on the aeroacoustics.

1.1. Fluid dynamics

We consider the continuity and momentum conservation equations for fluids, also known as Navier-Stokes equations:

$$\frac{\partial \rho}{\partial t} + \frac{\partial (\rho u_i)}{\partial x_i} = 0, \tag{1.1}$$

$$\frac{\partial (\rho u_i)}{\partial t} + \frac{\partial (\rho u_i u_j)}{\partial x_j} = -\frac{\partial p}{\partial x_i} + \frac{\partial \tau_{ij}}{\partial x_j}, \tag{1.2}$$

where ρ is the fluid density, u_i are the fluid velocity components, p is the pressure and τ_{ij} is the viscous stress tensor [10]. Starting from these equations some simplifications can be made according to the flow characteristics. One of these simplification is incompressible flow. As a criterion to establish when it is valid, it is possible to take the ratio between the velocity of the fluid and the speed of sound and check that is less than 0.3. This ratio is known as the Mach number (Ma). Another important non-dimensional parameter is the Reynolds number (Re) which describes the ratio between inertia and viscosity. It can be written as:

$$Re = \frac{\rho U D}{\mu}, \tag{1.3}$$

where μ is the dynamic viscosity, U is a fluid flow characteristic velocity and D is a geometrical characteristic length of the specific problem. The Reynolds number is a number that indicates the flow regime: low Re refers to laminar flow, while high Re refers to turbulent one [31]. Turbulent flows are very common regimes in everyday life and it is hard to correctly predict their behaviour. The main challanges from the physical point of view are related to the intrinsic three dimensional, dissipative and diffusive behaviour

of the turbulent flows. The energy is transferred from larger to smaller eddies and then turned into thermal energy. This process is called energy cascade.

1.2. Computational Fluid Dynamics

If the flow is very complicated, the analytical equations (1.1), (1.2) are too difficult to be solved without a numerical or experimental approach. For this reason the study of the Computational Fluid Dynamics (CFD) and its usage is of huge importance for the researchers. However, due to its nature, flow field involves numerous lengths scales. In order to resolve all the fluid length scale and have a direct numerical solution of equations (1.1) and (1.2) might be too computational expensive. Indeed, the minimum grid space required in order to fully resolve a turbulent flow field scale is very cogent, leading to unpracticable computational grids for moderate Reynolds numbers. This is why many turbulence models have been proposed in order to reduce the overall computational effort. Experiments are performed to calibrate and validate those models, and nowadays a large variety of models is available. There are different types of turbulence models and in the following paragraphs are described the most important ones.

1.2.1. Reynolds Averaged Navier-Stokes Equations

The Reynolds Averaged Navier-Stokes (RANS) equations are obtained starting from the instantaneous equations and averaging them in time. To do so, the velocity vector and the pressure are divided in two components: a mean and a fluctuating part. The Reynolds decomposition is now introduced:

$$u_i = U_i + u_i', \qquad p = P + p', \tag{1.4}$$

where P and U_i are the mean parts and p' and u_i' are the fluctuating ones.
Starting from (1.1) and (1.2) and writing them for an incompressible flow they become:

$$\frac{\partial u_i}{\partial x_i} = 0, \tag{1.5}$$

$$\frac{\partial u_i}{\partial t} + u_j \frac{\partial u_i}{\partial x_j} = -\frac{1}{\rho}\frac{\partial p}{\partial x_i} + \frac{1}{\rho}\frac{\partial \tau_{ij}}{\partial x_j}. \tag{1.6}$$

Then, by using the Reynolds decomposition (1.4) we finally write the RANS formulation:

$$\frac{\partial U_i}{\partial x_i} = 0, \tag{1.7}$$

$$\frac{\partial U_i}{\partial t} + U_j \frac{\partial U_i}{\partial x_j} = -\frac{1}{\rho}\frac{\partial p}{\partial x_i} + \frac{1}{\rho}\frac{\partial \tau_{ij}}{\partial x_j} - \overline{u_i' u_j'}. \tag{1.8}$$

From this latter equation is possible to notice that a new term, $\overline{u_i' u_j'}$, arises in the right hand side RHS of the equation describing the relationship between fluctuating velocities. This term is called "Reynolds stress tensor" and introduces a closure problem in the RANS approach where six additional unknowns appear in the stress tensor. To solve the closure problem a modelling strategy is usually employed. The many turbulence models can be divided in two families:

- One-equation model that solves a transport equation for one turbulent variable such as the turbulent kinetic energy k or the turbulent viscosity ν_t;
- two-equations model in which two transport equations are solved. A very common example is the kOmegaSST turbulence model that is also used in this thesis [36].

As previously said, RANS equations are not time dependent equations. Therefore, they cannot be employed for acoustic analysis. A different strategy could suggest to employ the Unsteady Reynolds Averaged Navier-Stokes (URANS) equations that keep the transient term and permit to describe a phenomenon variable in time such as the propagation of sound.

1.2.2. Large Eddy Simulation

The main strategy in Large Eddy Simulation (LES) is to filter the Navier-Stokes equations obtaining variables that depend on both space and time [36]. In this way, the turbulence scales are split in two: the bigger vortices are resolved as happens in the DNS, while the smaller ones are modelled. This method allows to reduce the time needed to solve the flow field with respect to a pure DNS and, at the same time, permits to efficiently describe only the scales of interest.
To obtain the filtered Navier-Stokes equations it is necessary to decompose the variables and to apply a filter as follows:

$$\begin{cases} \phi_i = \widetilde{\phi}_i - \phi_i^{SGS}, \\ \widetilde{\phi}_i(x_i) = \int\int\int_V \phi_i(x_i) G(x_i - x_i') dx_i. \end{cases} \tag{1.9}$$

In this system of equations $\widetilde{\phi}_i$ represents the filtered component, ϕ_i^{SGS} is the subgrid scale (SGS) component and G is the low pass filter. In other words ϕ_i^{SGS} contains all the spatial frequencies higher than the cut-off frequency. With this approach, the smallest vortex size resolved is not in the order of magnitude of the Kolmogorov scale but it is determined by the filter [28].
Although the LES are very accurate, they require a very fine grid especially near the walls increasing excessively the computational time. The need of developing an accurate turbulence model more affordable for industrial applications than the LES brought to the derivation of the DES turbulence model.

1.2.3. Detached Eddy Simulation

The Detached Eddy Simulation [39] was developed to face the challenge of high-Reynolds number flow in application fields such as aerospace, ground transportation and atmospheric studies. It is based on the combination of LES and RANS.
The main drawback of the RANS is that, as stated before, it is stationary and cannot evaluate the transient behaviour of some properties such as the sound and its propagation. On the other hand, the use of a LES is computationally expensive in terms of time and grid requirements.
The working principle is that the boundary layer is resolved by RANS and the outer regions are treated with LES; the space between these areas, known as the gray area, could give some problems unless the separation is abrupt or fixed by the geometry [39]. This model was originally formulated from the substitution of the distance function d in the one equation Spalart-Allmaras model, derived from the distance to the nearest wall, with a modified distance function:

$$\overline{d} = min(d, C_{des}\Delta), \tag{1.10}$$

where Δ is the cell length and C_{des} is a constant.
This means that in the near solid boundary regions where the turbulent length scale d is lower than the grid dimension ($d < C_{des}\Delta$), the DES model switches to RANS mode. Otherwise, in the other regions where the turbulent length scale overcome the grid dimension, the DES works as a LES [36]. Therefore, this filter permits to cut down the level of resolution needed to solve the simulation.

Despite the DES is studied starting from the Spalart-Allmaras model, it can be implemented with other RANS models by accurately modifying the turbulent length scale. A very good candidate is the kOmegaSST model, that being a two equation model, uses k and ω to define the turbulent length scale:

$$\overline{d} = min(C_{des}\Delta, \frac{\sqrt{k}}{\beta^*\omega}), \tag{1.11}$$

where β^* is a constant, k is the turbulent kinetic energy and ω is the specific dissipation rate [40].
The working principle of the filter is the same as the one explained for the Spalart-Allmaras model generating an hybrid model able to switch from LES to RANS in the regions where the turbulence length scale is lower than the grid length scale.

1.2.4. Delayed Detached Eddy simulation and Improved Detached Delayed Eddy simulation

Other variants of the DES present in literature and in the most common CFD codes are the Delayed Detached Eddy simulation (DDES) and Improved Detached Delayed Eddy simulation (IDDES).
DDES detects boundary layers and, even if the model should switch to LES because of the limiter, it prolongs the full RANS mode. In this way the detection depends on the eddy viscosity and for this reason it is a very good alternative to the standard DES.
IDDES is based on a new definition of Δ that combines the wall distance with the local characteristics of the grid. Δ tends to be depressed near the wall and give it a steep variation stimulating instabilities and boosting the resolved Reynolds stress [39].
In some of the test cases proposed in this thesis the DDES version of the kOmegaSST turbulence model is used.

1.3. Computational AeroAcoustics

The acoustics theory defines the sound as pressure fluctuations that propagate in form of waves through some transmission mediums, such as solids and fluids. A particular branch of acoustics that studies sound generation via either turbulent fluid motion or aerodynamic forces interacting with surfaces is called aeroacoustics.
Since the beginning of CAA a lot of difficulties have to be taken into account when addressing flow noise simulations. The main ones are the followings:

- Energy disparity and acoustic inefficiency: the energy in the flow and the radiated acoustic energy are very different from each other. We can say that the total radiated power of a turbulent jet scales with $\mathcal{O}(U^8/c^5)$, while a dipole source generated by the presence of an obstacle inside the flow scales with $\mathcal{O}(U^6/c^3)$. Therefore, an aeroacoustic process at low Mach number is a weak source of sound.

- Length scale disparity: the difference between the sizes of the eddies occurring in the turbulent flow and the wavelength of the generated acoustic sound might be big, leading to very different computational grid requirements. Consider for instance an eddie with length scale l_v and a characteristic frequency f. The emitted sound wave has the same frequency, but the wavelength λ is [33]:

$$\lambda \propto c_0 \cdot \frac{l_v}{U} = \frac{l_v}{Ma}. \tag{1.12}$$

  This means that $\frac{l_v}{\lambda} = Ma$. The difference between the length scales highly depends on the Mach number.

The fundamental work defining the models of sound generation was firstly proposed by James Lighthill. He developed a method to reduce the sound generated by a jet engine starting from the fundamental wave equation and then applying it in other important fields such as the submarine propellers, the rocket lift off and the automotive sector [36]. The equation proposed by Lighthill is the following wave equation.

$$\frac{1}{c_0}\frac{\partial^2 p'}{\partial t^2} - \nabla^2 p' = q, \tag{1.13}$$

This equation represents the propagation of the pressure perturbations p' where q is the source term and c_0 is the speed of sound. When the latter is not present, $q = 0$, the sound field is generated by the initial perturbations or boundary conditions. The method used to quantify the emitted noise is the Sound Pressure Level (SPL) measured in decibel (dB)

and calculated as:

$$SPL = 20\log_{10}(\frac{p'_{rms}}{p_{ref}}), \tag{1.14}$$

where p'_{rms} is the rms value of the fluctuating pressure p' and $p_{ref} = 2 \cdot 10^{-5} Pa$ for sound propagating in gases and $p_{ref} = 10^{-6} Pa$ for propagation in other media. The threshold of pain is around SPL = 140 dB [10]. Furthermore, the Lighthill's work brought to the development of the Computational Aero Acoustics (CAA) that implements numerical methods to solve the equations involved in the phenomenon. Two main numerical approaches can be distinguished:

- Direct methods: they use CFD codes to calculate directly both the fluid dynamic and acoustic solutions. This methods require a very fine grid to compute the solution, therefore the computational demand is very high.
- Hybrid methods: the solution of the flow field is completely separated from the acoustic propagation. Therefore, one can choose the best method to solve the CFD with the most suitable computational grid, and rely on other methods to solve the acoustic problem. the computational cost is much lower than the one required for a direct method [36].

In this thesis we will focus on hybrid integral methods with particular attention to the Curle's aeroacoustics analogy.

1.4. Hybrid Methods

As written before, hybrid schemes in CAA separate the acoustic computation from the flow field using aeroacoustic's analogies. This is possible due to the fact that we will consider mainly problems that have a one way coupling between the flow and the acoustics. This means that no energy is fed back into the flow from the acoustic wave propagation [36]. Some of the hybrid approaches rely on integral methods in order to compute the acoustic far field. The most common analogies are: the Lighthill's aeroacoustic analogy, Curle's aeroacoustic analogy and the Ffowcs Williams and Hawkings' aeroacoustic analogy (FW-H).
In the following paragraphs are described the main aeroacoustic analogies including the one used in this thesis'work.

1.4.1. Lighthill's acoustic analogy

The main idea is to associate the sound source to the actual flow problem and obtain a propagation problem in a fluid at rest.
The Lighthill's analogy can be obtained from the compressible Navier-Stokes equations by deriving in time the (1.1), deriving in space the (1.2) and subtracting them from each other [31].

$$\frac{\partial^2 \rho}{\partial t^2} - \frac{\partial^2}{\partial x_i \partial x_j}(\rho u_i u_j) = \frac{\partial^2}{\partial x_i \partial x_j}(p\delta_{ij} - \tau_{ij}). \tag{1.15}$$

It is then exploited the following mathematical identity:

$$c_0^2 \frac{\partial^2 \rho}{\partial x_i^2} = \frac{\partial^2}{\partial x_i \partial x_j}(c_0^2 \rho \delta_{ij}). \tag{1.16}$$

The equation (1.16) can be added to the equation (1.15) in order to get the inhomogeneous wave equation of Lighthill showing the source terms on the right hand side.

$$\frac{\partial^2 \rho}{\partial t^2} - c_0^2 \frac{\partial^2 \rho}{\partial x_i^2} = \frac{\partial^2}{\partial x_i \partial x_j}(\rho u_i u_j) + \frac{\partial^2}{\partial x_i \partial x_j}(p - c_0^2 \rho)\delta_{ij} - \frac{\partial^2}{\partial x_i \partial x_j}\tau_{ij}. \tag{1.17}$$

Furthermore, a decomposition of the properties of the flow into a mean value and an acoustic fluctuation is performed. Considering that the fluctuating components are responsible for the transfer of sound, the mean ones are neglected. Finally, we obtain the Lighthill wave equation:

$$\frac{\partial^2 \rho'}{\partial t^2} - c_0^2 \frac{\partial^2 \rho'}{\partial x_i^2} = \frac{\partial^2 T_{ij}}{\partial x_i \partial x_j}, \tag{1.18}$$

$$T_{ij} = \rho u_i u_j + (p' - c_0^2 \rho')\delta_{ij} - \tau_{ij}, \tag{1.19}$$

where ρ' is the fluctuating density, c_0 is the speed of the wave and the term T_{ij} is called Lighthill stress tensor. It contains the fluctuating components, the viscous stresses and a generalization of the entropy production term [28]. For low Mach and isentropic flow problems, Lighthill noticed that the term that contributes the most to the production of sound is $\rho u_i u_j$ [36]. Therefore, the Lighthill's tensor is semplified as follows:

$$T_{ij} \approx \rho u_i u_j. \tag{1.20}$$

It is known that the problem (1.18) can be solved analytically by employing a convolution between the source and a suitable Green function. The Green's function of the free field

radiation is used only for three dimensional problems and reads:

$$G(\boldsymbol{x},t)=\frac{\delta(\tau-t+\frac{r}{c_0})}{4\pi r}=\frac{\delta(g)}{4\pi r}, \tag{1.21}$$

where δ is the Dirac delta, g is equal to $g=(\tau-t+\frac{r}{c_0})$, τ is the retarded time and r is the distance between the observer and the sound source. They are defined respectively in equation (1.23) and (1.24). Finally, by using equation (1.21) and its symmetrical properties is possible to write the equation (1.20) in integral form:

$$\rho(\boldsymbol{x},t)-\rho_0=\rho'=\frac{1}{4\pi c_0^2}\frac{\partial^2}{\partial x_i\partial x_j}\int_V\frac{T_{ij}(\boldsymbol{y},\tau)}{|\boldsymbol{x}-\boldsymbol{y}|}dV(\boldsymbol{y}), \tag{1.22}$$

where V is the control volume and τ is the retarded time defined as the instant in which the acoustic radiation is emitted from the position $\boldsymbol{y}$ that is where the sound source is placed. t is instead defined as the time in which the fluctuations arrive to the observer's position $\boldsymbol{x}$.

$$\tau=t-\frac{|\boldsymbol{x}-\boldsymbol{y}|}{c_0}, \tag{1.23}$$

$$r=|\boldsymbol{x}-\boldsymbol{y}|. \tag{1.24}$$

1.4.2. Curle's acoustic analogy

The Lighthill's theory does not consider the presence of solid boundaries inside the flow. For this reason, Curle implemented his analogy to incorporate the contribution of the stationary surfaces on the sound emission.
Given the following generalized integral solution (1.18) for wave equation problems it is possible to derive the Curle Analogy [5]:

$$p'(\boldsymbol{x},t)=\int_{-\infty}^{+\infty}\left\{\int_{V_s}Q_pGdV+\int_{\partial v_B}(p'\frac{\partial G}{\partial\boldsymbol{n}}-G\frac{\partial p'}{\partial\boldsymbol{n}})dS\right\}d\tau, \tag{1.25}$$

where n is the normal to the surface S, Q_p is the given source and G is a given Green function. By knowing the expression of G we can actually solve the time integral in the equation (1.25). To do so we can re-formulate the first part of the surface integral in equation (1.25) as follows:

$$p'\frac{\partial G}{\partial\boldsymbol{n}}=p'\frac{\partial G}{\partial r}\frac{\partial r}{\partial\boldsymbol{n}}=\frac{p'}{4\pi}(\frac{d\delta}{dg}\frac{\partial g}{\partial r}\frac{1}{r}-\frac{\delta}{r^2})\frac{\partial r}{\partial\boldsymbol{n}}=\frac{p'}{4\pi}(\frac{d\delta}{d\tau}\frac{1}{c_0r}-\frac{\delta}{r^2})\frac{\partial r}{\partial\boldsymbol{n}}. \tag{1.26}$$

thus, after some manipulations, we can write:

$$p'(\boldsymbol{x},t) = \int_{v_s} \frac{Q_p}{4\pi r} dV + \int_{\partial v_B} \frac{1}{4\pi r}[(\frac{1}{c_0}\frac{\partial p'}{\partial \tau} + \frac{p'}{r})\boldsymbol{n}\cdot\boldsymbol{e}_r - \frac{\partial p'}{\partial \boldsymbol{n}}]_\tau dS, \tag{1.27}$$

where $\boldsymbol{e}_r$ is the radial versor. The equations are expressed using the pressure p as acoustic variable but, considering the state equation is possible to switch to the density ρ as variable [10].

1.4.3. Acoustic sources

The equation (1.22) contains only the Lighthill stress tensor T_{ij} as source term and describes a quadrupole which propagation is represented by four lobes as shown in figure 4a. The quadrupole mechanism is due to fluctuating stresses in the fluid. In order to identify the other acoustic sources is necessary to look at the equation (1.27) in which the first surface integral refers to a dipole while the volume integral refers to a monopole.
The monopole sound field is generated by the mass flux through the surface S and propagates uniformly in all directions. The dipole sound field is obtained from the reaction of the surface to the force $F_j = -\int_S n_j(p_{ij}\delta_{ij} - \tau_{ij})$ exerted from the flow to the surface itself. Its propagation is represented by two lobes in a principal direction [10].

1.4.4. Ffowcs Williams and Hawkings's acoustic analogy

The analogy of Ffowcs Williams and Hawking further extended the work that Curle had done by taking into account the sound generated from the motion of a body, which velocity is indicated with v, immersed in a turbulent flow. In this thesis this formulation is not directly studied and applied to the test cases but it has to be intended as the evolution of the Curle's acoustic analogy applied to moving bodies. The formulation is derived from the manipulation of the Navier-Stokes equations and, after some further manipulations, the equations reads [36]:

$$\begin{aligned}\rho(\boldsymbol{x},t) - \rho_0 = &\frac{1}{4\pi c_0^2}\frac{\partial^2}{\partial x_i \partial x_j}\int_V \frac{T_{ij}^*}{r(1-\frac{l_j v_j}{c_0})} dV(\boldsymbol{y}^*) \\ &- \frac{1}{4\pi c_0^2}\frac{\partial}{\partial x_i}\int_S \frac{F_i^*}{r(1-\frac{l_j v_j}{c_0})} dS(\boldsymbol{y}^*) \\ &+ \frac{1}{4\pi c_0^2}\frac{\partial}{\partial t}\int_S \frac{Q^*}{r(1-\frac{l_j v_j}{c_0})} dS(\boldsymbol{y}^*),\end{aligned} \tag{1.28}$$

where

$$T_{ij}^* = \rho(u_i^* + v_i)(u_j^* + v_j) - \tau_{ij}^* + (p - c_0^2(\rho - \rho_0))\delta_{ij}, \tag{1.29}$$

$$F_i^* = (\rho(u_i^* + v_i)u_j^* + p\delta_{ij} - \tau_{ij}^*)n_j, \tag{1.30}$$

$$Q^* = (\rho_0 v_i + \rho u_i^*)n_i, \tag{1.31}$$

$$l_j = \frac{(x_j - y_j)}{r}. \tag{1.32}$$

The three source terms (1.29), (1.30) and (1.31) indicate respectively a quadrupole, dipole and monopole source mechanism.

1.5. Curle's implementation in OpenFoam

To perform the acoustic study in the applications faced in this thesis, a function implemented directly in OpenFOAM containing the aeroacoustic analogy of Curle is used. To derive it, it is necessary to start from the equation (1.27) and apply the following semplifications [19]:

- No volumetric sources.
- Retarded time is neglected.
- $\frac{\partial p'}{\partial n} = 0$. This condition is valid only if the chosen surfaces coincides with the surface of a rigid body. Furthermore, it is equivalent in requiring the body to be rigid and fully reflective [5].

Therefore, the equation reads:

$$p'(\boldsymbol{x}, t) = \int_{\partial v_B} \frac{1}{4\pi r} \left[\left(\frac{1}{c_0} \frac{\partial p'}{\partial t} + \frac{p'}{r} \right) \boldsymbol{n} \frac{\boldsymbol{r}}{r} \right] dS. \tag{1.33}$$

Furthermore, by solving the integral we get the final formulation implemented in OpenFOAM:

$$p' = \frac{1}{4\pi} \frac{\boldsymbol{r}}{r^2} \cdot \left(\frac{\boldsymbol{F}}{r} + \frac{1}{c_0} \frac{d\boldsymbol{F}}{dt} \right), \tag{1.34}$$

where $\boldsymbol{r}$ is the distance vector between the source and the observer, r is the module of the vector distance $\boldsymbol{r}$ and $\boldsymbol{F}$ is the force vector acting on the surface of the body.
The results obtained with this model will be discussed in the next chapters.

2 | Square cylinder test case

The aim of this thesis is to provide an accurate understanding of the Curle's aeroacoustic analogy implemented in OpenFOAM applied to different test cases where the sound emission and propagation is studied.
Phillips [27] compared sound intensity levels of a circular cylinder from semiempirical model based on Curle's equation with experimental results and pointed out a very strong relationship between the sound generation and unsteady forces of bluff bodies. This suggested that the noise emitted from the body is mainly due to the aerodynamic force fluctuations and can be well estimated using the Curle's equation [1].

2.1. Flow specifications

The problem under investigation is represented by a rigid square cylinder of side length $D = 3.2798 \cdot 10^{-5}\ m$ immersed in a laminar flow of velocity $U = 68.6\ m/s$ with a Reynolds number of $Re_D = UD/\nu = 150$. The physics of the phenomenon is governed by the incompressible Navier-Stokes equations (1.7) and (1.8) resolved by the finite volume discretization approach on which OpenFOAM is based. The kinematic viscosity and the density are respectively set equal to $\nu = 1.5 \cdot 10^{-5}\ m^2/s$ and the Mach number is $Ma = 0.2$. The results of the CFD simulation are compared with the ones of Ali [1] to get a proper validation.

2.2. Numerical setup

Based on the experimental results is possible to say that the case is two dimensional because of the very low Reynolds number. The three dimensional flow structure characteristics occur when the $Re > 160$, therefore for $Re = 150$ the flow around a single square cylinder is 2D and laminar [1]. In order to achieve a stationary flow, the non dimensional computational time is set to $TU/D \approx 250$ and the non dimensional time step is $\Delta tU/D \approx 0.006$ to keep the CFL under 0.8. The simulation is carried on using the

solver pimpleFOAM and with the following numerical schemes:

- 2^{nd} order backward scheme for temporal discretization;
- the convection term is discretized using the LUST scheme. It is a blended 75% linear and 25% linearUpwind scheme;
- 2^{nd} order linear scheme for the viscous term.

2.2.1. Computational domain

The computational domain is generated taking the origin of the reference system in the center of the square cylinder that is placed at 10D from the inlet and 20D to the outlet boundary along the stream-wise direction x. Along the cross-stream direction y the domain extends above and below the square cylinder for 10D, see figure 2.1.

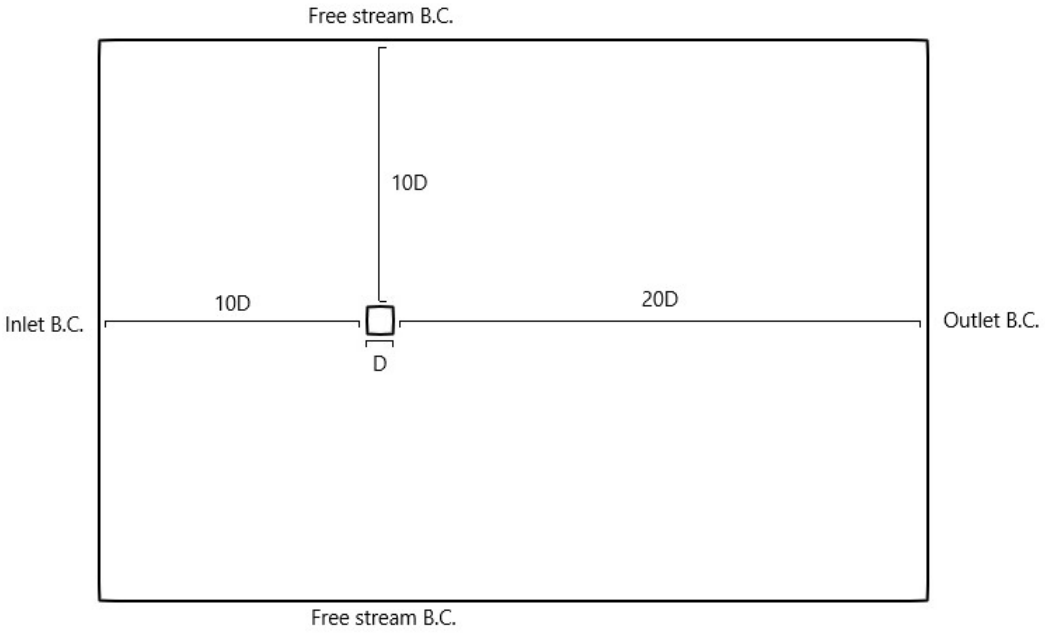

Figure 2.1: Flow domain for the square cylinder laminar case.

By looking at the figure the air flows from left to right crossing the square cylinder.

2.2.2. Boundary conditions

To numerically solve the incompressible Navier-Stokes equations used to model this problem is necessary to define the boundary conditions for the pressure and the velocity. They are listed in the following table:

	p	U
Inlet	zeroGradient	fixedValue (u specified)
Outlet	fixedValue	inletOutlet
Top	zeroGradient	slip
Bottom	zeroGradient	slip
Cylinder	zeroGradient	noSlip ($u_x = u_y = u_z = 0$)

Table 2.1: Boundary conditions for the laminar square cylinder.

2.2.3. Mesh

The mesh of the computational domain in this study is constructed following two grid refinements in order to achieve a good accuracy of the results. The first grid is constituted by 644×368 cells, while the second one has double the number of cells both in x and y direction for a total of 1288×736 cells generating in both cases a completely structured grid of hexahedra. The mesh is stretched in the cross stream direction y, in order to have a cell expansion ratio of 5 between the first cell on the body and the last, at the edge of the domain both above and below the cylinder. Cells are stretched also along the streamwise direction, in particular in the wake region the cell expansion ratio is 4 while between the inlet and the body is equal to 8.
In figure 2.2 and 2.3 is possible to have a closer look to the refinement obtained close to the square cylinder.

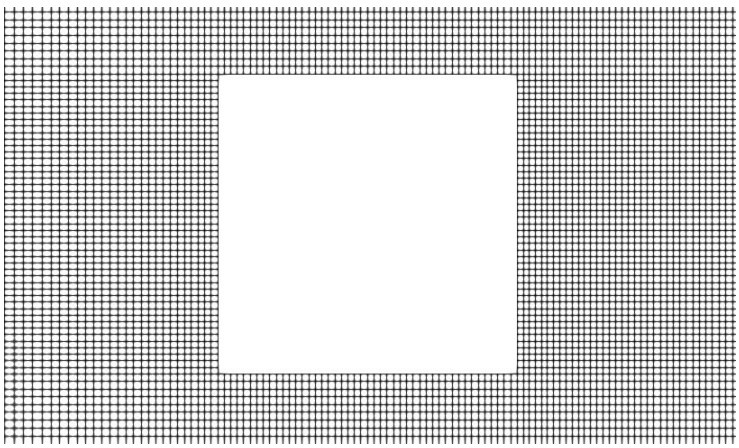

Figure 2.2: 644×368 cells grid.

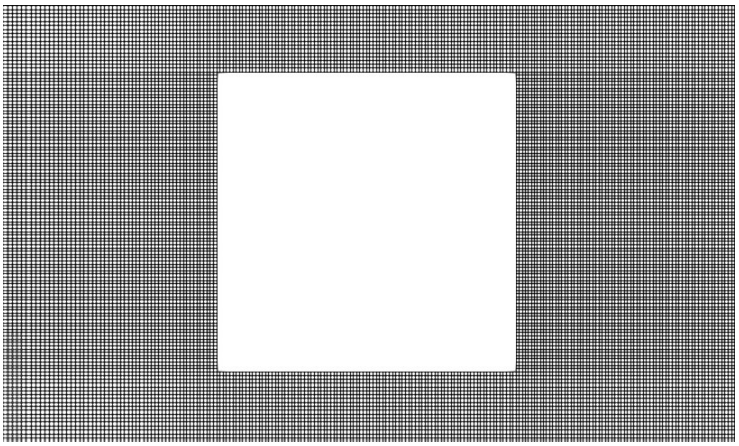

Figure 2.3: 1288×736 cells grid.

2.3. Results and discussion

In this section we will discuss both the results related to the flow characteristics and the results related to the acoustics obtained from the above described setups.

2.3.1. Flow characteristics

The unsteady laminar flow crossing the square cylinder is characterized by separation starting from the upper corners of the geometry. This phenomenon, together with the $Re = 150$, generates vortexes in the wake of the cylinder obtaining the so called Von Karman street that can be seen in figure 2.4a.

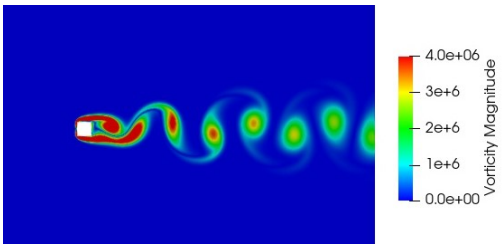

(a) Instantaneous vorticity contours ($\boldsymbol{\omega} = \nabla \times U$) obtained at $TU/D = 250$.

(b) Instantaneous pressure field obtained at $TU/D = 250$.

Figure 2.4: Instantaneous pressure and vorticity for the case with the coarser grid.

For the laminar case, the shedding of the vortexes is periodic and defined by the velocity of the undisturbed flow and the dimension of the geometry. By using these parameters it

is possible to define the Strouhal number as follows:

$$St = f_{st} \cdot \frac{D}{U}, \tag{2.1}$$

where f_{st} is the Strouhal frequency of the vortexes defined as the inverse of the shedding period T_{st}.

A grid convergence study is performed to compare the flow results obtained with the coarser grid with the ones obtained with the finer grid. The analysis is summarized in the following table:

Case	$N_x \times N_y$	TU/D	St	Cl_{rms}	Cd_{mean}
A	644×368	≈ 250	0.161	0.278	1.458
B	1288×736	≈ 250	0.16	0.278	1.459

Table 2.2: Grid convergence Study for the square cylinder test case.

Previous Studies	St	Cl_{rms}	Cd_{mean}
Ali et. al [1]	0.16	0.285	1.47
Sohankar et. al [37]	0.165	0.230	1.44
Doolan [7]	0.156	0.296	1.44

Table 2.3: Comparison of the case A with the previous study.

From the table 2.2 is possible to notice that the fluid dynamic quantities are very similar to each other, in particular the lift coefficient. Therefore, the coarser refinement is chosen to perform the acoustic analysis because it shows a very good agreement with the paper of Ali et. al [1] from which The values mentioned in the 2.3 are taken.
Figure 2.5a shows the time history of the aerodynamic coefficients obtained from the instantaneous aerodynamic force that is derived from the instantaneous pressure acting on the surface. An example of pressure field at a fixed time step is shown in figure 2.4b. The generic non-dimensional force coefficient c_x is calculated with the following equation:

$$c_x = \frac{F_x}{\frac{1}{2}\rho U^2 A_{ref}}. \tag{2.2}$$

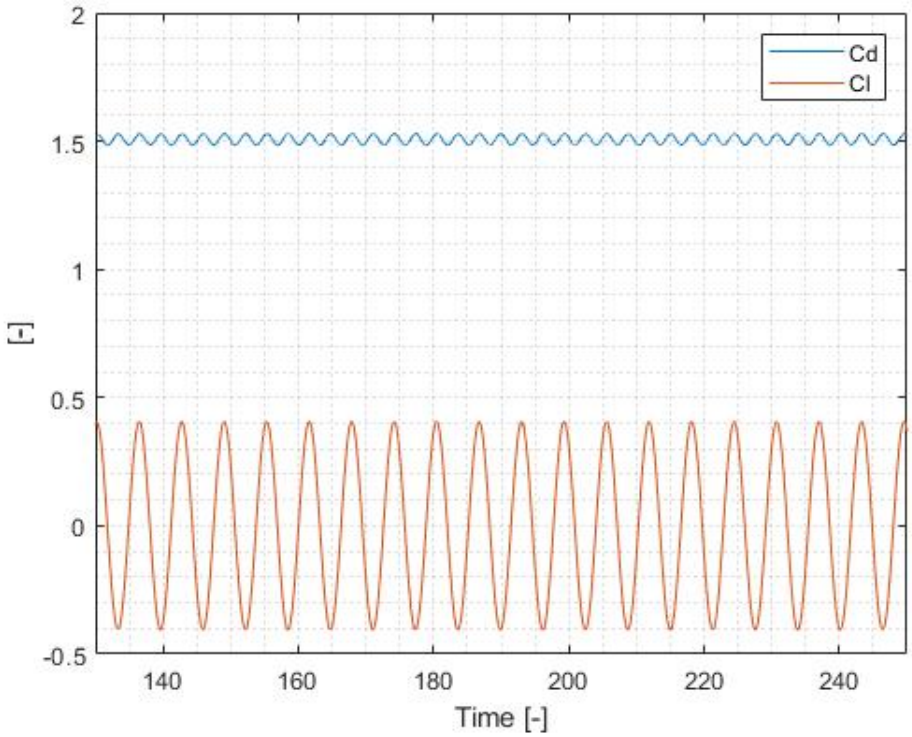

(a) Time histories of drag and lift coefficient for the case A.

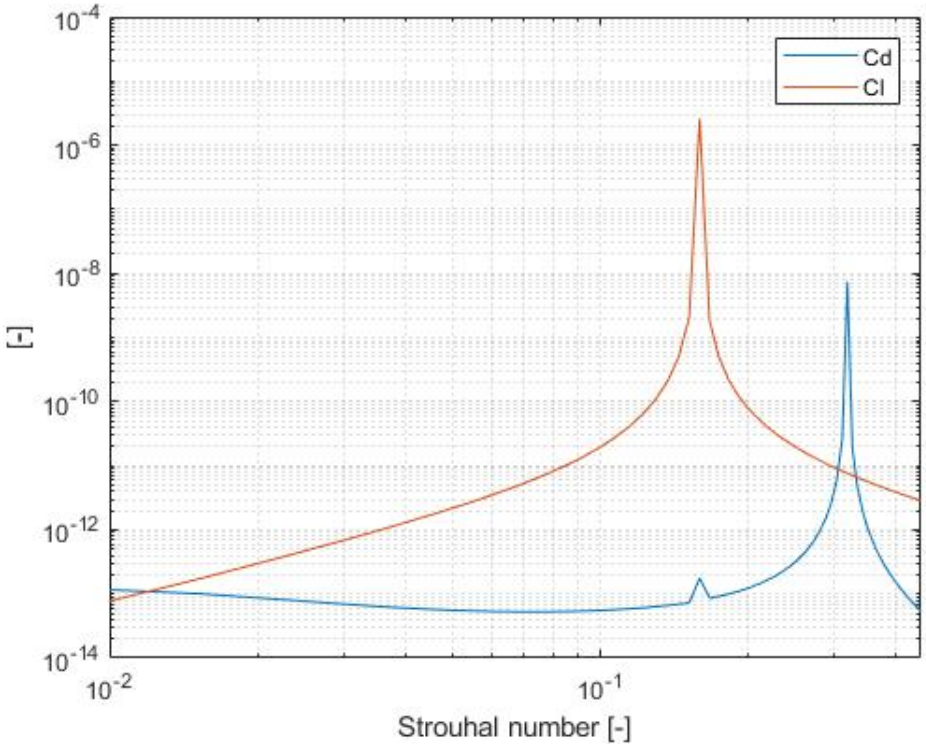

(b) Power Spectral Density of the drag and lift coefficient for the case A.

Figure 2.5: Time histories and PSD of the aerodynamic coefficients for the square cylinder test case.

The sampling of the data starts from a non-dimensional time $TU/D = 130$ and ends at $TU/D = 150$ allowing us to have enough vortex shedding periods after the stationary condition to obtain very accurate results. Figure 2.5b shows that the frequency of the drag coefficient is double the one of the lift (Strohual frequency fs). This is due to the fact that the drag coefficient along the stream wise direction is affected by both the vortexes shedded from the top and from the bottom of the square cylinder. The lift coefficient is instead given by the alternatively shedding of the vorteces from the two sides of the geometry.
On the basis of these considerations the acoustic analysys is carried on in the next paragraph.

2.3.2. Acoustics

Positively concluded the fluid-dynamic validation, the results can be used to study the acoustics of the related geometry. The Curle's aeroacoustic analogy implemented in OpenFOAM is the one described in the equation (1.34) and allows to obtain the pressure oscillations generated from the interaction of the wind with the square cylinder. Given this information is then possible to study the directivity of the noise propagation and emission and its intensity using the equation of the Sound Pressure Level (SPL) (1.14). The main acoustic source is a dipole related to the forces and their time derivatives acting on the body's surface.
Qualitatively, figure 2.6 shows the sound propagation in the far field obtained exploiting the function $CurleSurface$ in OpenFOAM. The surface over which the values are plotted in the figure below extends for $5000D$ downstream and upstream of the sound source both in the x and y direction.

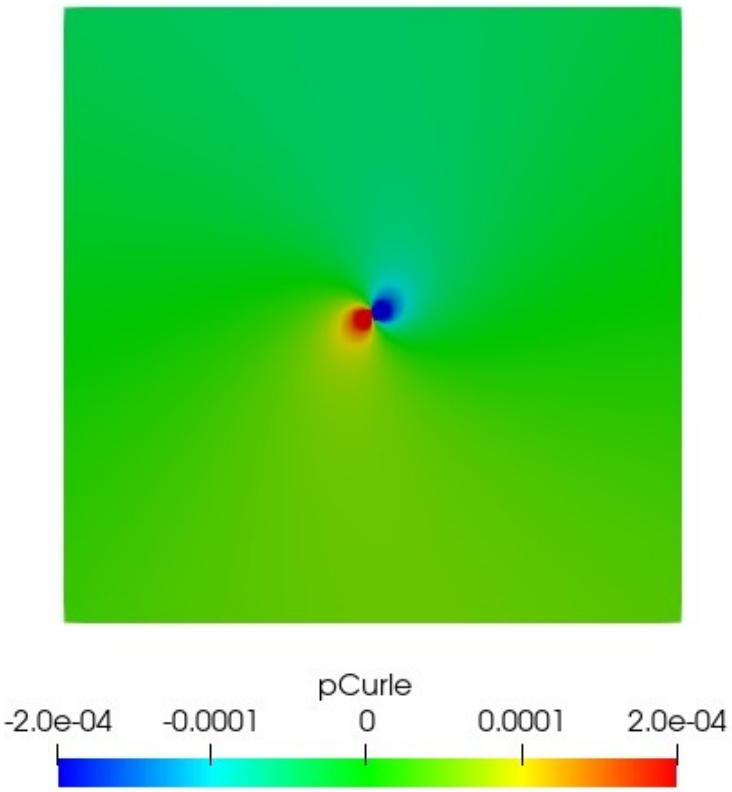

Figure 2.6: Contours of instantaneous acoustic pressure ($\widetilde{P} = p'/(\rho U^2)$) at the non dimensional time instant $TU/D = 250$.

It is possible to clearly distinguish the dipole created by the time dependent acoustic pressure oscillations arised from the presence of an obstacle in the flow, i.e. the square cylinder. The dipole it is not perfectly symmetrical with respect to the x direction because it represents only the acoustic pressures taken at the last time instant of the simulation. By doing a time averaging over the sampling window is possible to get the symmetrical propagation pattern.
If we compare figure 2.6 with the dipole in figure 4b there is one big difference: the fluctuation in space is not detected. In other words, the positive and negative peaks of the acoustic pressure oscillations in space do not compare because the model implemented in the software, differently from what is done in Ali et. al [1], does not consider the contribution of the retarded time expressed in the equation 1.23. In this way, the noise propagation is instantaneous and the sound reaches the observers as soon as it is emitted from the source.
Figure 2.7 is instead showing the oscillations of the acoustic pressure in time splitting the contribution of the force and its derivative taken from the equation (1.34) as done in the

following:

$$A1 = \frac{1}{4\pi}\frac{\boldsymbol{r}}{r^3} \cdot \boldsymbol{F}, \tag{2.3}$$

$$A2 = \frac{1}{4\pi}\frac{\boldsymbol{r}}{r^2}\frac{1}{c_0} \cdot \frac{d\boldsymbol{F}}{dt}. \tag{2.4}$$

The term $A1$ and $A2$ are obtained by modifying the source code of the Curle's function *curlePoint* implemented in the CFD software.

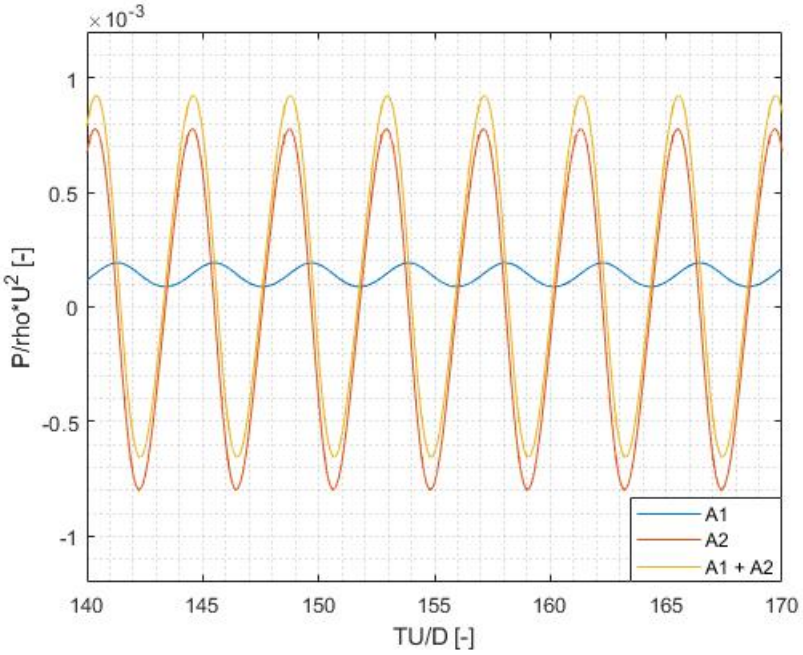

Figure 2.7: Instantaneous time dependent acoustic pressure ($\widetilde{P} = p'/(\rho U^2)$) obtained at the non dimensional time range between $TU/D = 140$ and $TU/D = 170$ at a distance of $R = 75D$ from the acoustic source in the cross stream direction.

By plotting the two contributions on the overall acoustic pressure we can appreciate that the term that dominates the sound generation in the equation 1.34 is the derivative of the force $A2$.
The fluctuations of figure 2.7 are derived from the placement of several probes in the far field done to measure the acoustic pressures variable in time. 45 observers are placed around a circumference of radius $R = 75D$ and centered in the sound source as shown in the figure below.

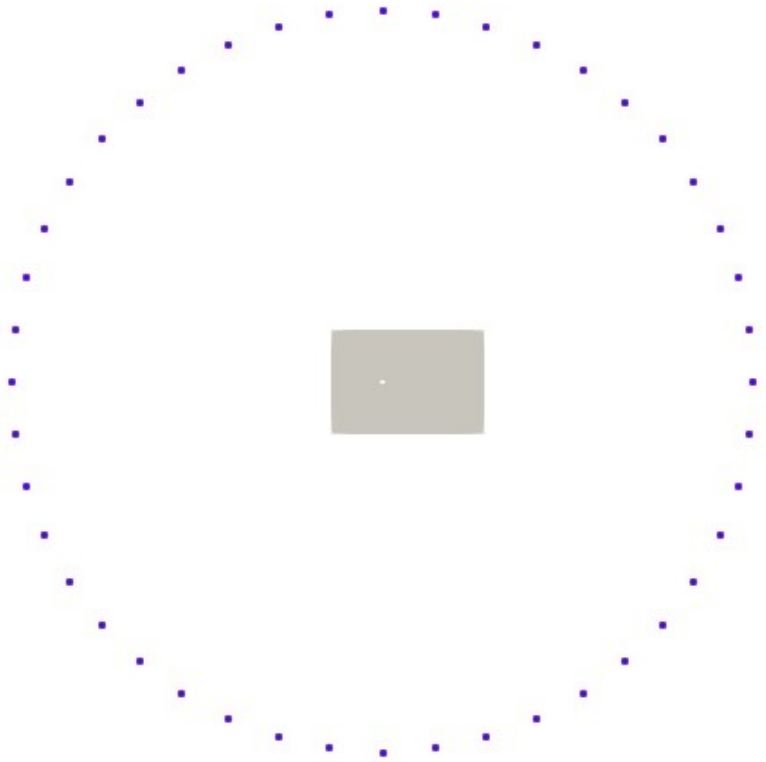

Figure 2.8: Position of the 45 observers placed along a circumference of $R = 75D$ and centered in the center of the square cylinder.

With this strategy is possible to study the directivity of the sound by performing a spectral analysis of the acoustic pressure time histories as post-processing. The SPL at the Strouhal frequency is taken for each of the 45 probes in order to derive the p'_{rms} from the inverse of the equation 1.14.

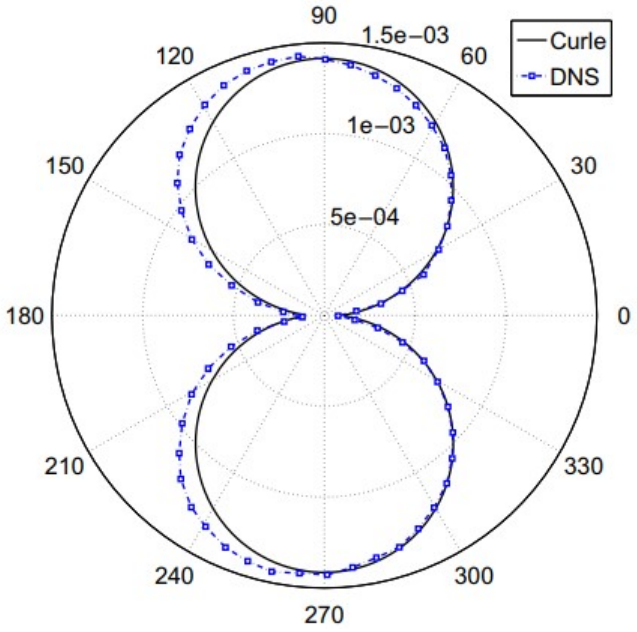

Figure 2.9: Directivities of root mean square sound pressure ($\widetilde{P}_{rms} = p'_{rms}/(\rho U^2)$) at the Strouhal frequency, R = 75D, Re = 150, Ma = 0.2 shwon in the paper of Ali et. [1] obtained using the Curle's analogy.

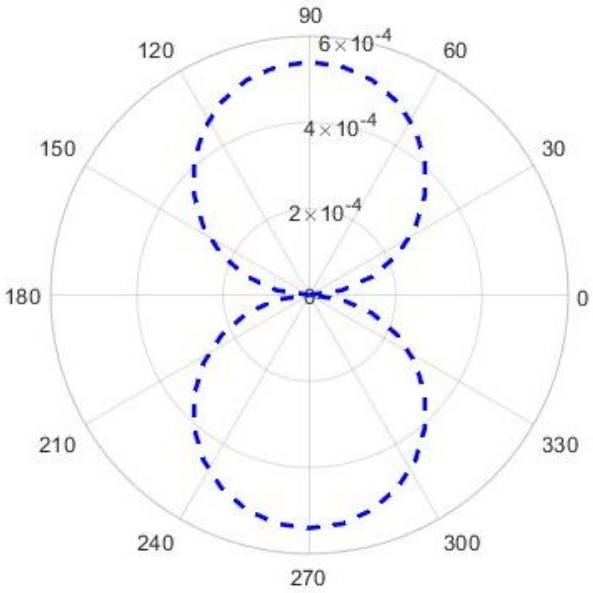

Figure 2.10: Directivities of root mean square sound pressure ($\widetilde{P}_{rms} = p'_{rms}/(\rho U^2)$) at the Strouhal frequency obtained using the Curle's analogy implemented in OpenFOAM for the square cylinder test case.

Figure 2.9 and 2.10 show a comparison between the results obtained in this work and the ones of Ali [1]. The same directivity pattern (Dipole) can be seen in both figure suggesting a very good qualitative agreement with the literature and the theory while, the big difference is related to the sound intensity being underestimated by the model studied in this thesis. As already said, this is due to the fact that the retarded time is not taken into consideration leading to a very strong error in the predictions.
150 probes are also placed along the cross stream direction y starting from a distance of $1D$ from the center of the geometry and reaching the distance of $150D$. The strategy is the same as before: we take the SPL at the Strohual frequency f_{st} of each observer and derive the p'_{rms}. The final aim now is to analyze if and how much the Curle's aeroacoustic analogy implemented in OpenFOAM is able to detect the decay of the sound by getting further from the acoustic source.

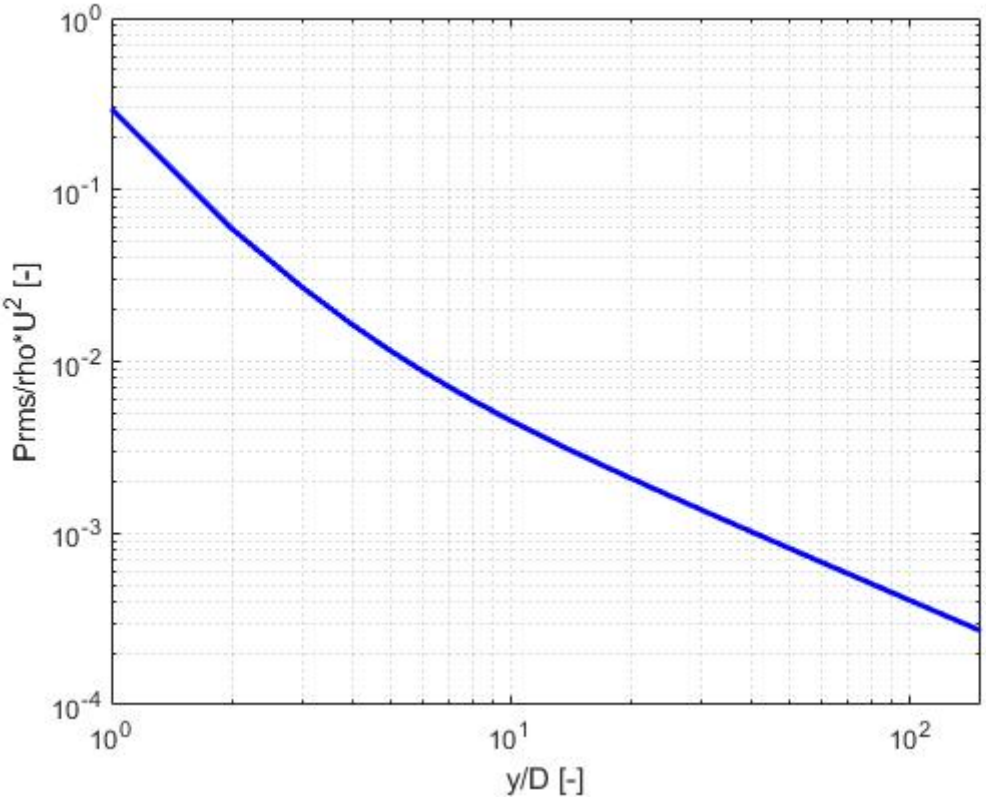

Figure 2.11: Decay of root mean square sound pressure ($\widetilde{P}_{rms} = p'_{rms}/(\rho U^2)$) at the Strouhal frequency obtained using the Curle's analogy implemented in OpenFOAM for the square cylinder test case.

By having a look to this figure we can clearly distinguish the decay of the noise but from a quantitative point of view, we still have to face the same limits analyzed before. In this

test case the aeroacoustic model of Curle implemented in OpenFOAM is useful to obtain an initial and qualitative guess of the sound emitted from an acoustic source.
The sound generated by the bluff body is strongly related to the aerodynamic forces acting on the body itself, therefore it is possible to reduce the noise by reducing the aerodynamic load, in particular the rms value of the lift coefficient [1].

3 | Rectangular cylinder test case

The aerodynamic behaviour of rectangular cylinders has attracted the attention of the scientific community since the first experimental reference works of Okajima [26] and Norberg [25], [3]. For this reason, a benchmark study on the aerodynamics of a stationary rectangular cylinder with chord-to-depth ratio equal to 5 was launched in July 2008 with the aim to propose a new case benchmark. The Benchmark on Aerodynamics of a Rectangular Cylinder (BARC) [4].

A big amount of configurations of the BARC flow obtained in both wind tunnel experiments and numerical simulations are gathered together with the aim to establish a platform where the results can be compared. This permits to give a wider view of the problem in terms of bulk parameters, flow and aerodynamic load statistics, pressure and forces. From a physical point of view, although the geometry is really simple, the flow over an elongated rectangular cylinder at high Reynolds numbers is very complex, being three dimensional, turbulent and characterized by unsteady flow separation and reattachments [4].

This case allows to further investigate the qualitative accuracy of the Curle's aeroacoustic analogy already applied to the square cylinder. Concerning the acoustics of this application, there are not many data available in literature. Therefore, the study presented in this chapter aims to give a first and qualitative guess of the sound emitted taken the rectangular cylinder as the noise source with the aim to be employed in a second moment for experimental validations.

The main reference in this chapter is represented by the paper of Bruno [3] that is used to validate the flow results obtained from the CFD simulation. The detailed flow and acoustics characteristics used for the simulation setup are carefully described in the following paragraphs.

3.1. Flow specifications

The physics of the examined case is governed by the time-dependent incompressible Navier-Stokes equations (1.1) and (1.2) with a Reynolds number equal to $Re = 4 \cdot 10^4$. This value is obtained with a free stream velocity $U = 1\ m/s$, a kinematic viscosity $\nu = 1.5 \cdot 10^{-5}\ m^2/s$ and a density $\rho = 1.205\ kg/m^3$.
The air flows across a rectangular cylinder with a chord-to-depth ratio $B/D = 5$ characterised by sharp edges and a smooth surface generating a 3D, turbulent and unsteady flow with an incidence $\alpha = 0$ and a turbulence intensity $Ti = 0.1\%$. The above mentioned Reynolds number is calculated considering the length of the body in the cross stream direction $D = 0.6\ m$ while on the span-wise direction the length L of the cylinder is equal to the chord B of the body itself.

3.2. Numerical setup

Differently from what happens in the laminar case, given the high Reynolds number, the first issue that has to be faced is clearly turbulence modeling. Although the most used approaches are the LES and DES, there are studies published on the BARC platform that rely on Unsteady Reynolds Average (URANS) models such as the one of Mannini et al. [21] and Ribeiro [30]. More precisely LES simulations represent 51% of the numerical contributions, the DES ones 30% and, finally, URANS computations 29% [4].
In this work a 3D RANS simulation with a kOmegaSST turbulence model is firstly run with the aim to reach a steady-state solution able to initialize all the field variables (U, p, k, $omega$ and ν_t) for a 3D Detached Eddy simulation (LES) that is used to obtain the results for the fluid-dynamic and acoustic post process shown in the following paragraphs. In this way is possible to reduce the non-dimensional simulation time of the DES that, in order to enhance a good convergence and maintain the CFL below 1, is set to be equal to $TU/D = 800$ with a time resolution of $\Delta tU/D = 0.01$. The turbulence model used for the Detached Eddy Simulation is the kOmegaSSTDDES that permits, as already described in chapter 1.2.3, to reduce the computational effort with respect to a pure LES.
The solver pimpleFOAM and the following numerical schemes have been employed:

- 2^{nd} order backward scheme for temporal discretization;
- 2^{nd} order Gauss linearUpwind scheme for the convection term including k and $omega$;
- 2^{nd} order linear scheme for the viscous term.

3.2.1. Computational domain

The computational domain is shown in figures 3.1 and 3.2 where the origin of the reference system is placed in the center of the rectangular cylinder. In this case the domain is three-dimensional and the span-wise length $L = 3m$ is defined equal to the chord $B = 5D = 3m$.

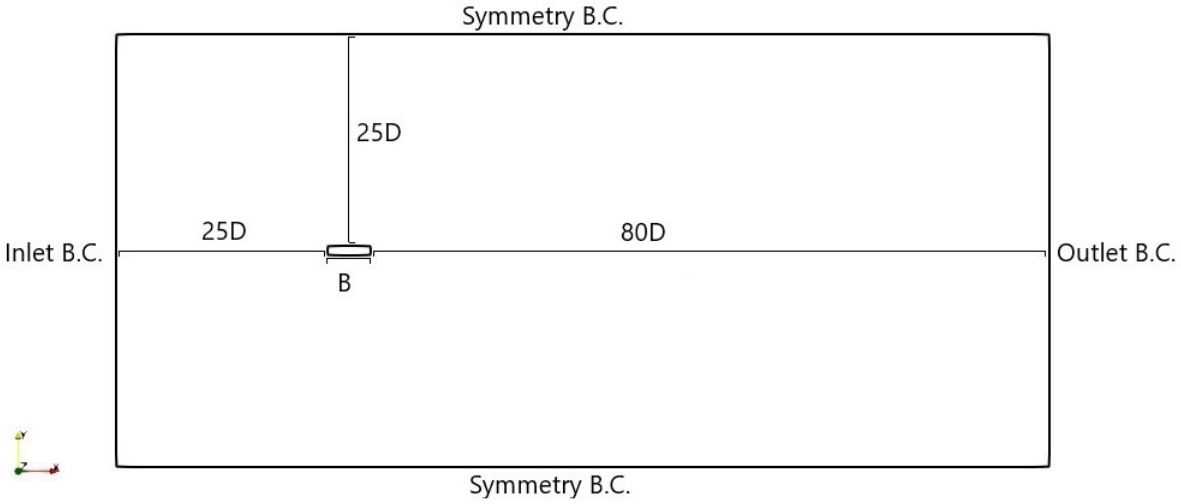

Figure 3.1: Lateral view.

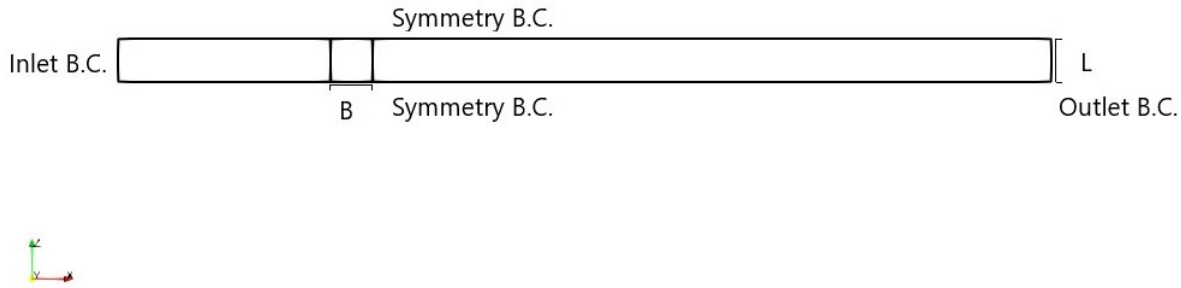

Figure 3.2: Top view.

Also in this case the fluid flows from left to right across the rectangular cylinder.

3.2.2. Boundary conditions

The boundary conditions chosen for the RANS and LES simulations are shown in the table 3.1. The initial value of the turbulence intensity k, the specific turbulent dissipation rate *omega* and the turbulent viscosity ν_t is guessed starting from the free stream velocity U and the turbulent intensity Ti.

	p	U	k	ω	ν_t
Inlet	zeroGradient	fixedValue	fixedValue	fixedValue	calculated
Outlet	fixedValue	zeroGradient	zeroGradient	zeroGradient	calculated
Top	symmetry	symmetry	symmetry	symmetry	symmetry
Bottom	symmetry	symmetry	symmetry	symmetry	symmetry
Front	symmetry	symmetry	symmetry	symmetry	symmetry
Back	symmetry	symmetry	symmetry	symmetry	symmetry
Wall	zeroGradient	noSlip	WallFunction	WallFunction	WallFunction

Table 3.1: Boundary conditions for the laminar square cylinder.

The Reynolds Average simulation is stopped once it reaches the steady-state and the obtained scalar and vector values of the field parameters are used as initial conditions for the Detached Eddy Simulation.

3.2.3. Mesh

A structured hexahedral grid is adopted to discretise the spatial computational domain. The 2D mesh in the x-y plane is constituted of 372×144 cells that are projected along the span-wise direction, where 24 cells are employed to uniformly obtain a 3D grid. Hence, the spatial resolution in the z direction is $\Delta z/B = 0.042$, i.e., lower than the minimum requirement for the spanwise discretisation $\Delta z/B \leq 0.1$ proposed by Tamura et al. [41] and equal to the one proposed by Bruno [3]. This grid generation strategy allows to achieve a good resolution with an overall number of cells equal to $1.216512 \cdot 10^6$. The mesh is stretched in the cross stream and in the stream wise direction, both towards the inlet and the outlet, with a cell expansion ratio of 50.

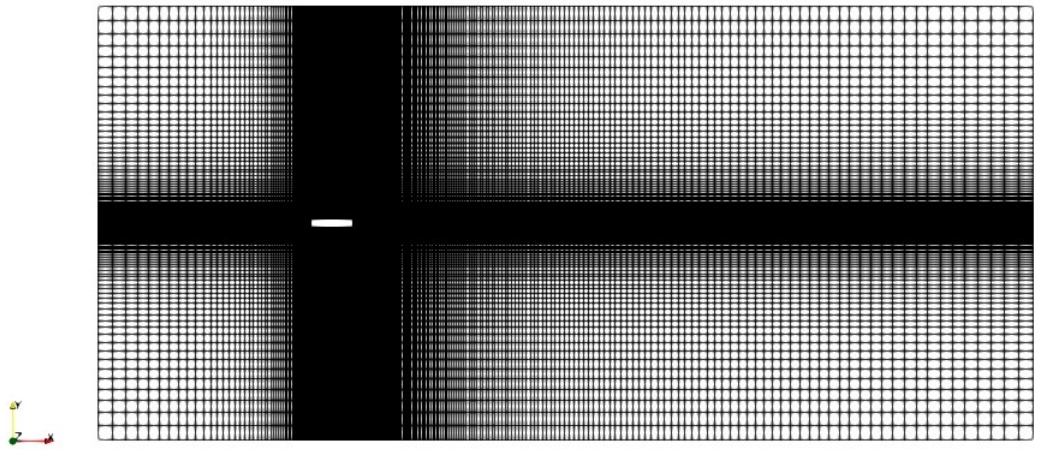

Figure 3.3: Grid resolution of the computational domain in x-y plane.

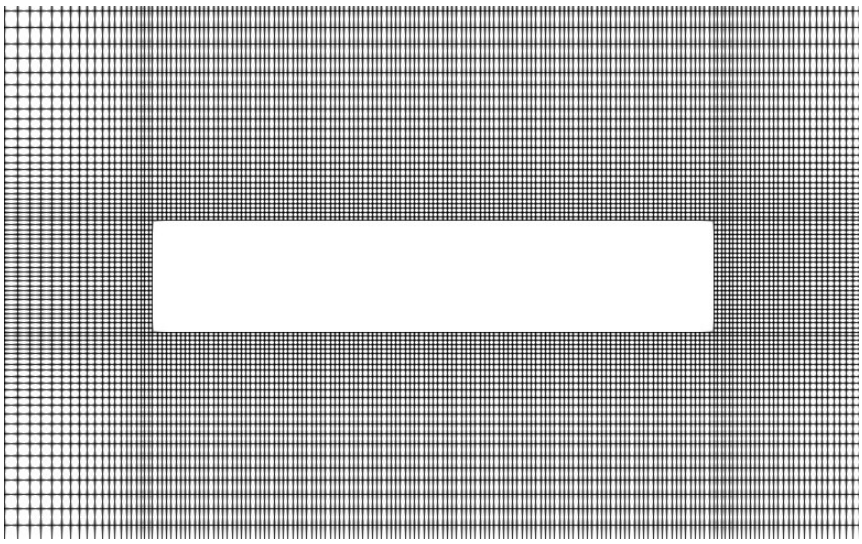

Figure 3.4: Focus on the spatial resolution of the rectangular cylinder.

Being the flow turbulent and unsteady is really important to correctly model the turbulence quantities in the near wall region. As it is possible to see in table 3.1, the strategy adopted is to use wall functions to speed up the simulations and reduce the computational time. With this choice is possible to obtain value of y^+ in the cross stream direction up to $y^+_{max} = 41.43$ with a mean value equal to $\overline{y^+} = 18.28$. This is not a critical value since it is not necessary to predict the correct point where the separation happens because it is completely driven by the sharp edges of the rectangular cylinder.

3.3. Results and discussion

As done for the laminar square cylinder test case, in the following paragraphs are described and explained the results obtained from the point of view of the fluid-dynamics and the acoustics.

3.3.1. RANS Flow characteristics

As said in 3.2, the strategy adopted for this test case is to perform a RANS simulation and use it to initialize the flow fields for a more accurate 3D DES approach. Figure 3.5 highlights the velocity field obtained as output of the RANS simulation in which is possible to recognize that a very good convergence and stability of the solution are reached. Furthermore, another proof of convergence is given by figure 3.6 that plots the aerodynamic coefficients derived from the forces acting on the surface of the rectangular cylinder.

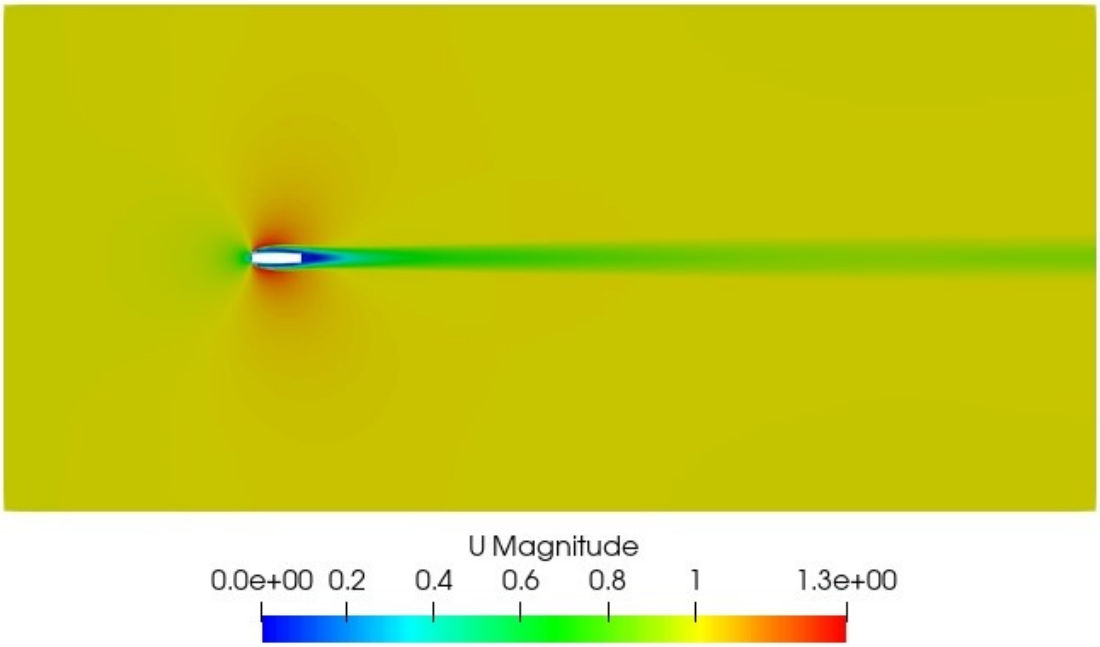

Figure 3.5: Velocity field of the RANS rectangular cylinder test case in the x-y plane at the last iteration.

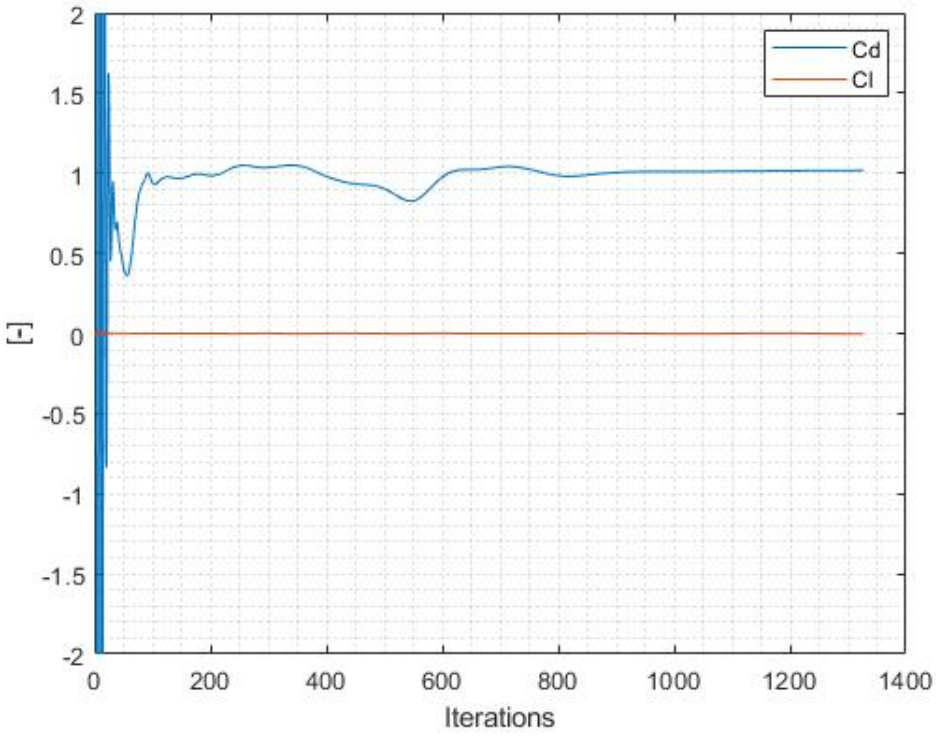

Figure 3.6: Aerodynamic coefficients of the RANS rectangular cylinder test case.

From this point on the results are used as initial conditions for the Detached eddy Simulation.

3.3.2. LES Flow characteristics

The flow in this test case is turbulent and for this reason the phenomenon is characterized by the non periodic and chaotic shedding of the vortices as it is possible to see in figure 3.7b. Differently from the laminar setup, there are multiple frequencies associated to the region behind the wake of the cylinder. In order to estimate the Strouhal number, it is considered the dominant frequency as the shedding frequency.

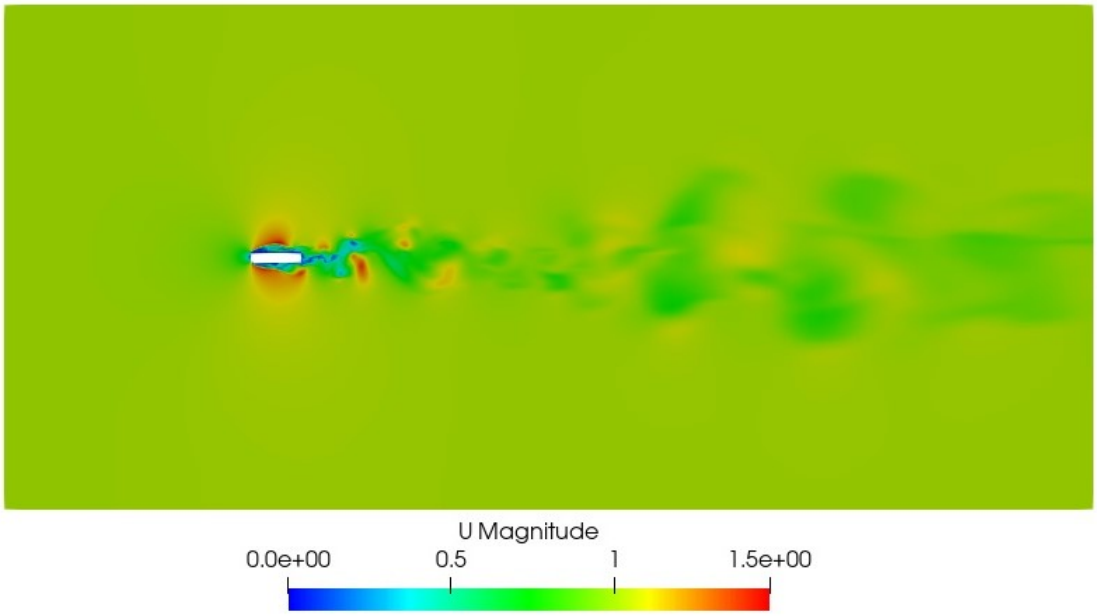

(a) Velocity field of the DES rectangular cylinder test case in the x-y plane at $TU/D = 800$.

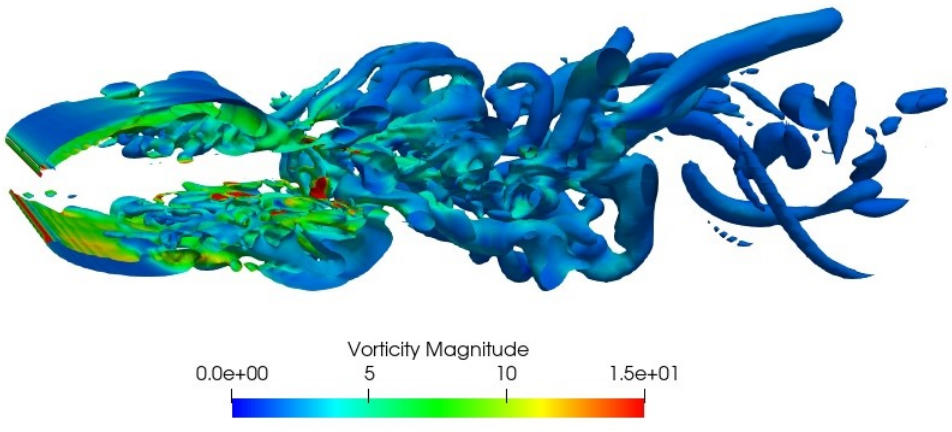

(b) 3D velocity field plotted over vorticity contours at $TU/D = 800$.

Figure 3.7: 2D and 3D instantaneous velocity field for the rectangular cylinder test case at $TU/D = 800$.

In figure 3.7b can be appreciated also the three dimensionality of the phenomenon being the Reynolds number very high, while the velocity field is plotted in order to point out the differences with the same field obtained in the RANS simulation 3.5 in which the eddies are not present since the quantities are averaged in time.
To validate the simulation performed in this thesis with the literature, the calculation and usage of the aerodynamic coefficients is essential. The time histories of the non-dimensional forces and their frequency components are shown in the figure 3.8 and 3.10.

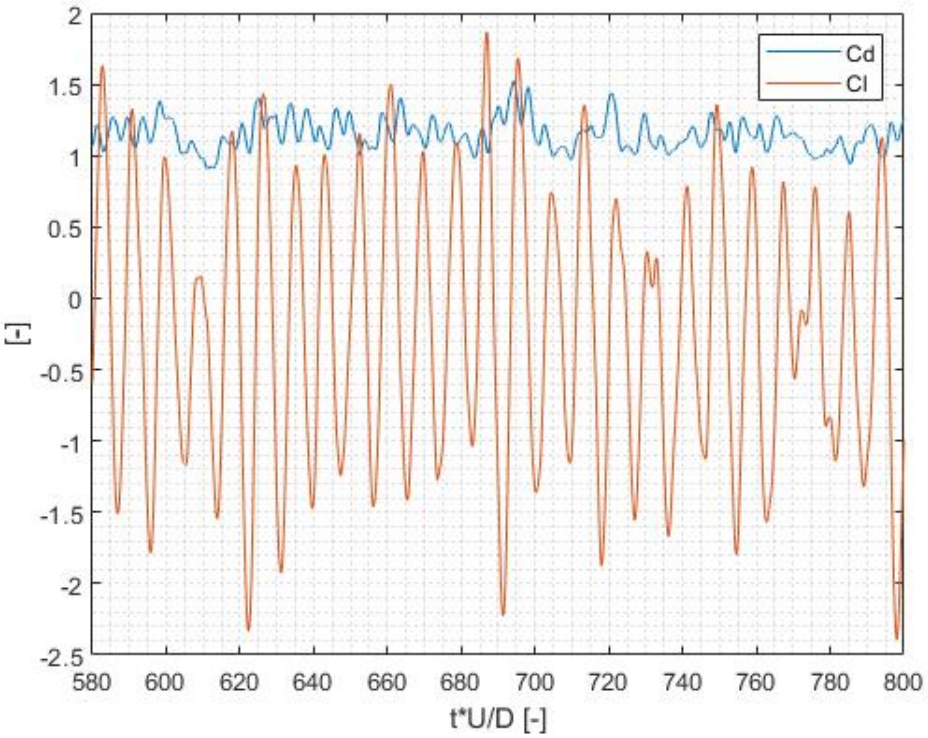

Figure 3.8: Time histories of drag and lift coefficient for the rectangular cylinder test case (BARC).

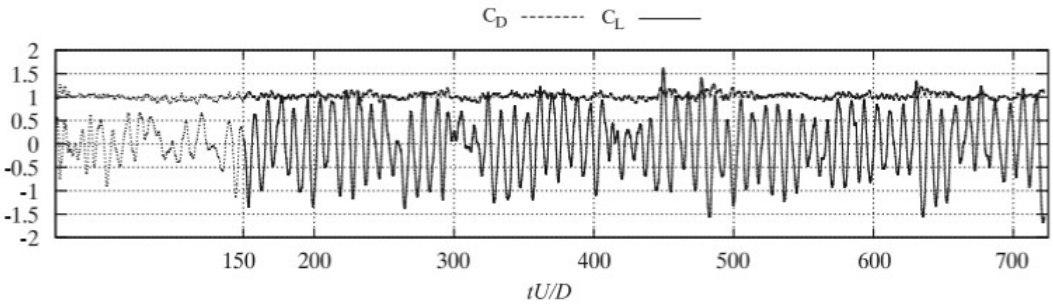

Figure 3.9: Time histories of drag and lift coefficient shown in the paper of Bruno et. al [3].

The sampling of the data starts at $TU/D = 580$ and ends at $TU/D = 800$ permitting to have a range of information related to the shedding of the vortices that is extended enough to capture the physics of the phenomenon. In the figure that shows the Power Spectral Density of the aerodynamic coefficients is possible to notice the dominant frequency and its value, in particular $St \approx 0.1136$. In the same figure 3.10 there's also a peak related to the drag force that is double the one related to the lift. As in the laminar case, this is due to the fact that the drag coefficient is affected by the vortices shedded from the bottom and upper part of the rectangular cylinder.
Figures 3.9 and 3.11 indicate respectively time histories and power spectral densities of the drag and lift coefficients present in the paper of Bruno et. al [3]. This comparison shows a very good agreement between the results having the same qualitative behaviour of the aerodynamic coefficients and the same dominant frequency.

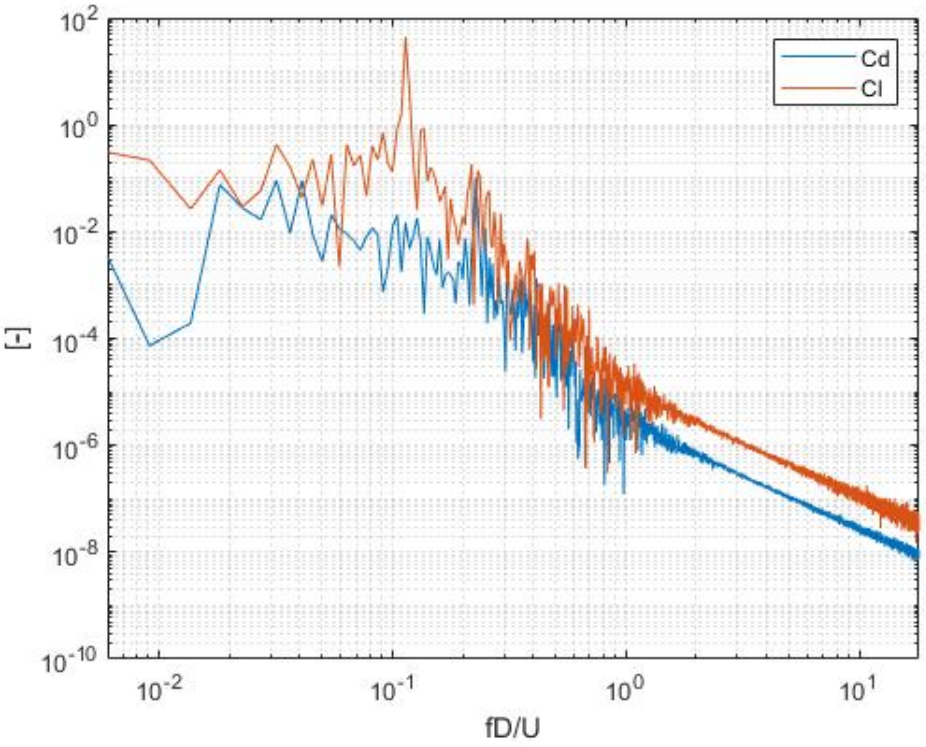

Figure 3.10: Power Spectral Density of the drag and lift coefficient for the rectangular cylinder test case (BARC).

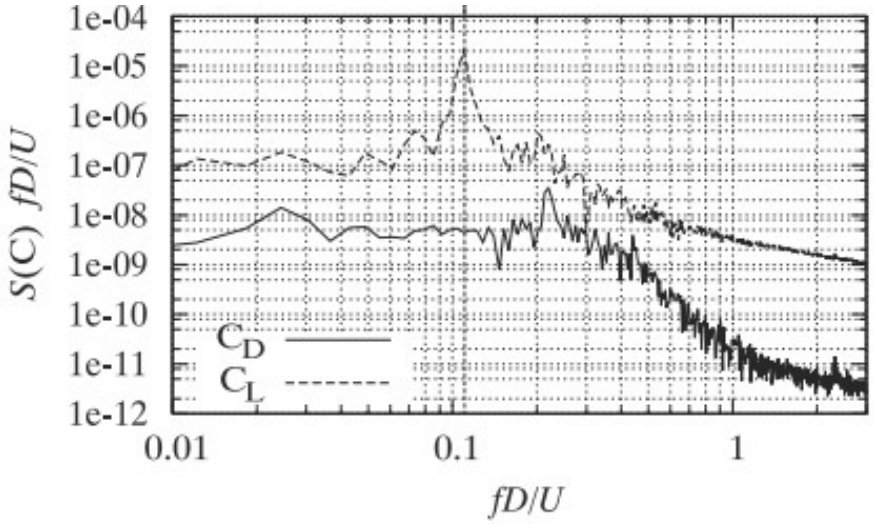

Figure 3.11: Power Spectral Density of the drag and lift coefficient shown in the paper of Bruno et. al [3].

What is interesting to look at are the different frequencies that compose the signal in time of the forces due to the high turbulence of the flow.
Quantitatively the fluid dynamics characteristics of the flow are summarized in the following table:

Previous Studies	St	Cl_{rms}	Cd_{mean}
Bruno et. al [3]	0.112	0.73	1.03
Mannini and Schewe [21]	$0.087 - 0.119$	$0.173 - 0.553$	$0.965 - 1.016$
Wei and Kareem [42]	–	$0.495 - 1.465$	$1.165 - 1.305$
Present work	0.1136	0.96	1.10

Table 3.2: Comparison of the obtained results with the literature of the BARC [4].

The table 3.2 compare the obtained results with the literature pointing out the main similarities and also divergences. It is shown that the near wake flow, the base pressure and, hence, the drag coefficient obtained in the different flow configurations are in very good agreement. The lift coefficient is instead strongly sensitive to set-up and modelling of the simulation, leading to a significant dispersion of the numerical predictions [4]. To further validate the described work with the literature we plot the distribution of the pressure coefficient cp averaged in time along half of the perimeter of the rectangular

cylinder identified by the absissa s (see figure 3.12). The cp is calculated as follows:

$$cp = \frac{p - p0}{\frac{1}{2}\rho U^2}, \tag{3.1}$$

where $p0$ represents the static pressure that in our case is equal to zero.

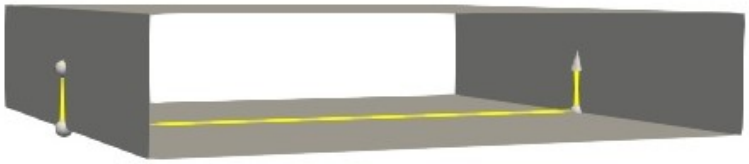

Figure 3.12: Highlights of the absissa s (red line) along which the mean pressure coefficient $\overline{cp}$ is plotted.

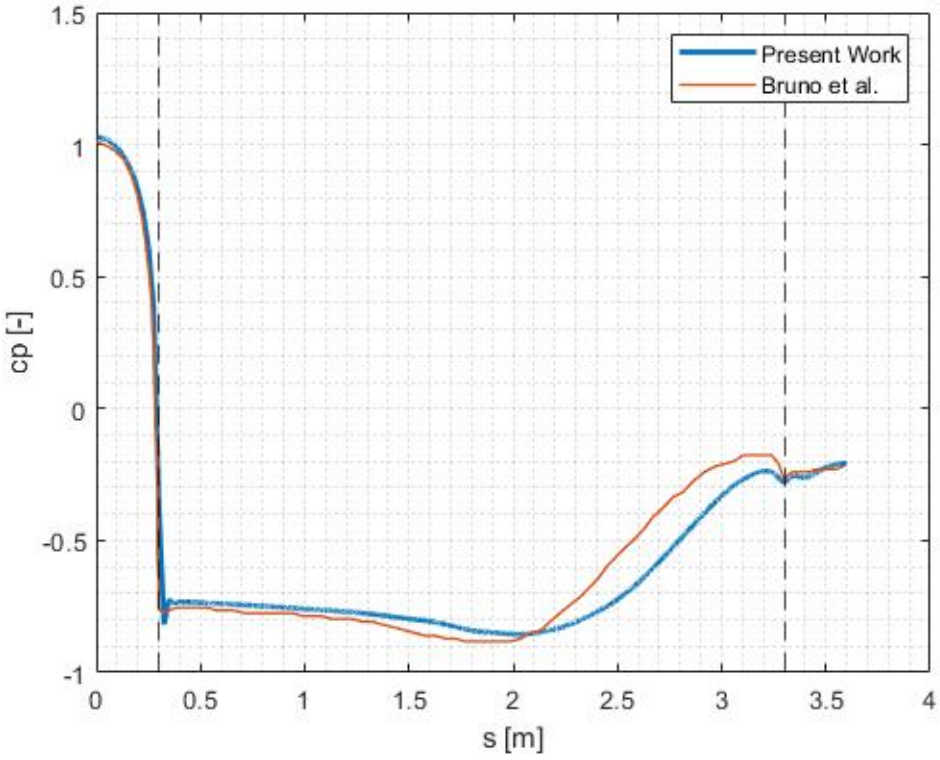

Figure 3.13: Profile of $\overline{cp}$ along half of the rectangular cylinder perimeter.

In figure 3.13 the two black lines represent respectively the point in which there are the two edges of the rectangular cylinder (where the geometry changes orientation).
The trend of the mean pressure coefficient is in very good agreement with the experimental data available in the literature [4].

3.3.3. Acoustics

The acoustic results obtained using the Curle's aeroacoustic analogy are described in this paragraph starting from the time dependent acoustic pressure fluctuations given as an output of the equation 1.34. The oscillations plotted in figure 3.15 refers to the probe placed at a distance of $75D$ from the center of the rectangular cylinder along the y direction.

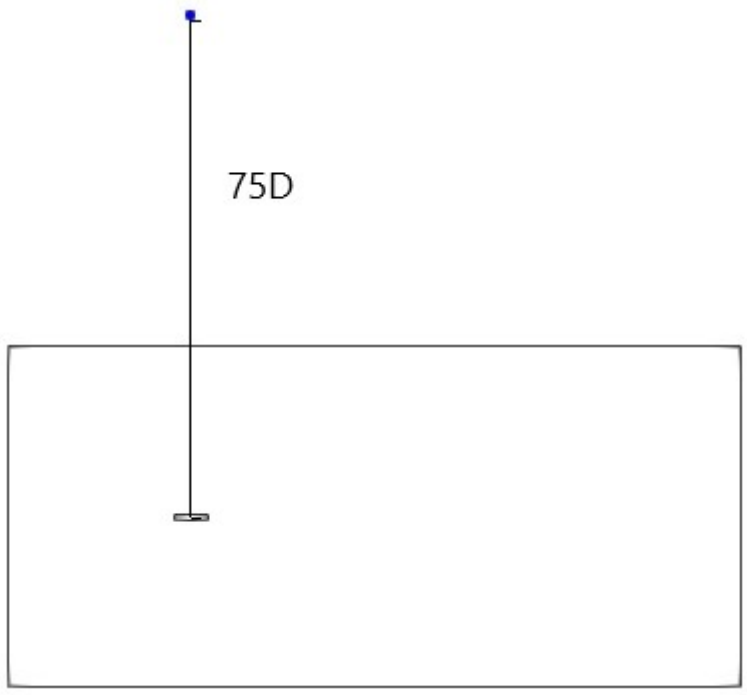

Figure 3.14: Probe position at 75D from the center of the rectangular cylinder in y direction.

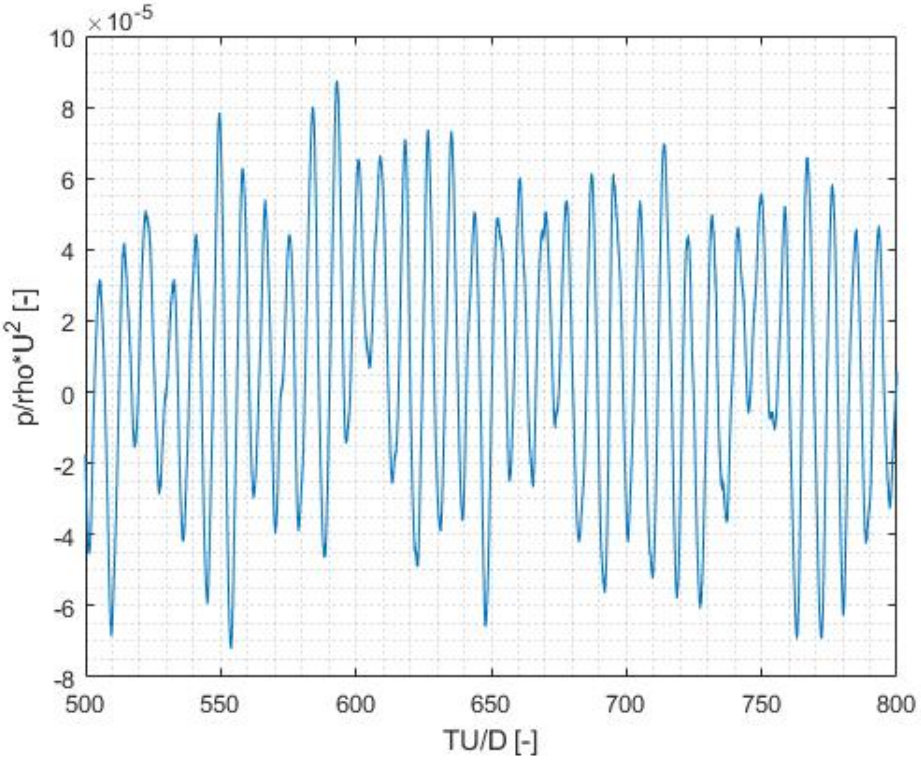

Figure 3.15: Instantaneous time dependent acoustic pressure ($\widetilde{P} = p'/(\rho U^2)$) obtained at the non dimensional time range between $TU/D = 500$ and $TU/D = 800$ at a distance of $R = 75D$ from the acoustic source in the cross stream direction for the rectangular cylinder test case.

This strategy allows to get a wider knowledge of the phenomenon permitting to study the directivity of the sound propagation and its intensity. From this point on is necessary to state that the model used to predict the noise emission is not fully developed because it is not considering the retarded time and the volume acoustic source generated by the turbulence. In figure 3.16 are shown the trends of the noise against the frequency for three different observers pointing out the f_{st} already obtained with the spectrum analysis of the aerodynamic coefficients.

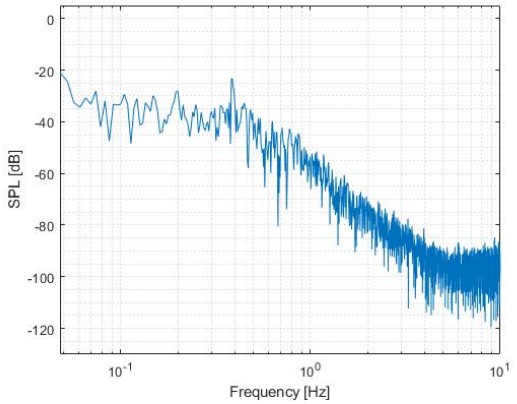

(a) SPL measured by the probe placed at $75D$ from the acoustic source in the stream wise direction ($0deg$).

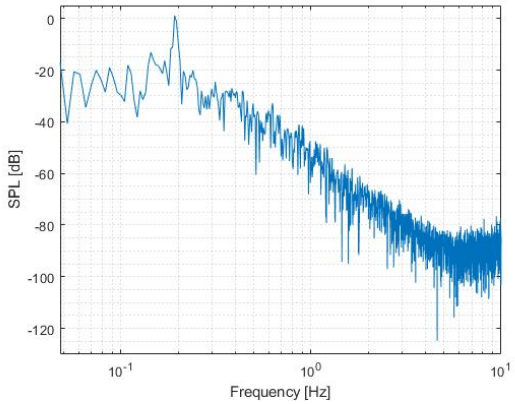

(b) SPL measured by the probe placed at $75D$ from the acoustic source along the direction inclined of $45deg$ with respect to the horizontal.

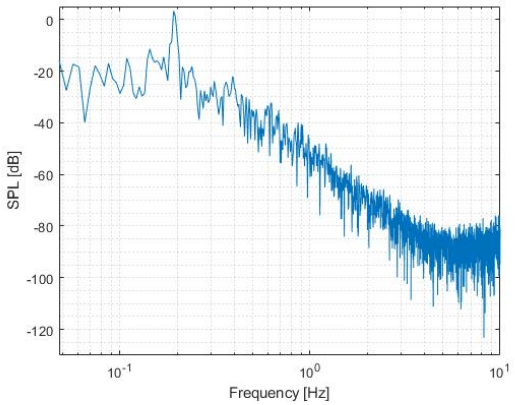

(c) SPL measured by the probe placed at $75D$ from the acoustic source in the cross stream direction ($90deg$).

Figure 3.16: Sound Pressure Level measured at different probes position along the circumference.

By looking at the figures it is possible to notice that the dominant frequency for the probe placed along the stream wise direction (figure 3.16a) is the one of the drag. This is completely aligned with the frequency analysis performed in the previous paragraph related to the flow characteristics of the simulation.
Furthermore, by analyzing the data taken from the 45 probes is possible to derive the directivity of the sound propagation in the far field.

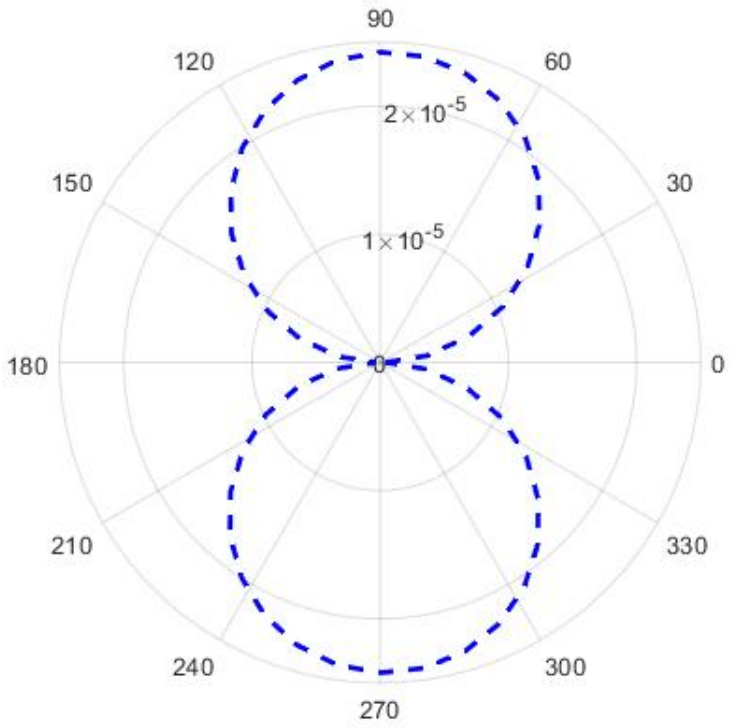

Figure 3.17: Directivities of root mean square sound pressure ($\widetilde{P}_{rms} = p'_{rms}/(\rho U^2)$) at the Strouhal frequency obtained using the Curle's analogy implemented in OpenFOAM for the rectangular cylinder test case.

As for the square cylinder laminar case, the graph in figure 3.17 is obtained taken the SPL at the dominant frequency f_{st} at each probe.
Also in this test case the decay of the noise emitted from the source is studied by placing 75 probes along the cross stream direction y until the distance of $150D$ from the center of the rectangular cylinder is reached. We can appreciate the progressive reduction of the sound as we getting further from the source validating the model from a qualitatively point of view.

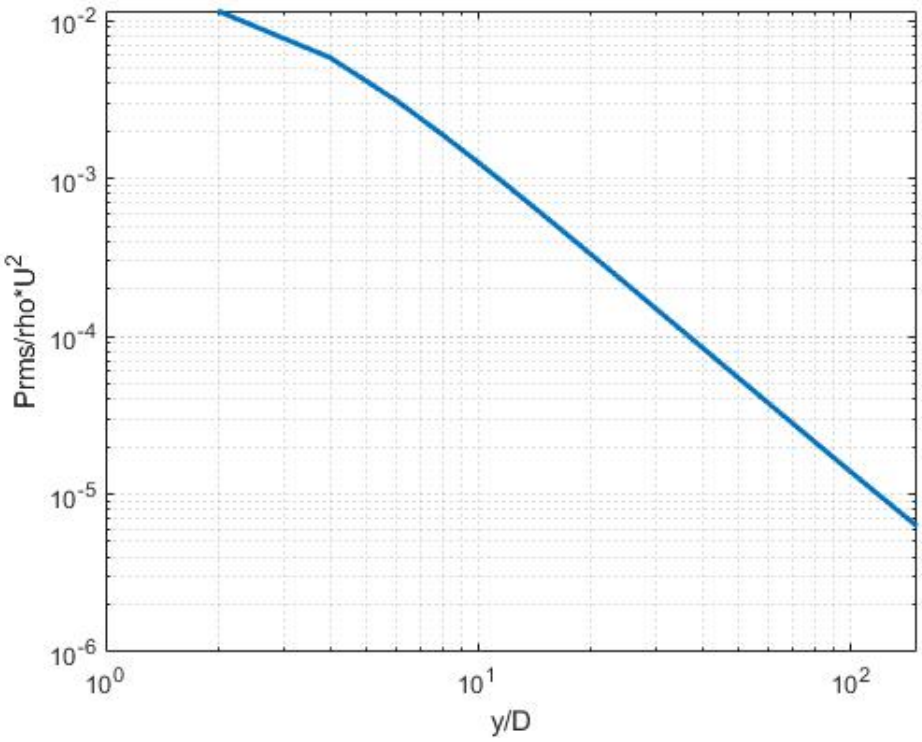

Figure 3.18: Decay of root mean square sound pressure ($\widetilde{P}_{rms} = p'_{rms}/(\rho U^2)$) at the Strouhal frequency obtained using the Curle's analogy implemented in OpenFOAM for the rectangular cylinder test case.

Despite the very low amount of data available in literature we can say that the results are qualitatively correct since the dominant frequency, the decay and the dipole have been obtained. Unfortunately, it is not possible to say the same from the quantitative point of view since some comparisons in the literature are not present. As said before, the errors are due to the lack of the terms related to the retarded time and the volume acoustic source. In order to best evaluate the current implemented Curle model for the considered application, an experiment should be carried out.

4 | Side view mirror test case

The noise reduction induced by the wind experienced by the driver or the passengers of a ground vehicle is an important parameter for the comfort assessment. The emitted sound can be a consequence of different flow phenomena occurring in low Mach number flows. The main components exposed to this problem that are primary sources of noise are the side view mirrors, the A-pillars, the tires and the underfloor details when the vehicle travels above approximately 120 km/h [2].
By the study of the articles mentioned in the introduction, a better estimation of the acoustic field using the DES model can be noticed. For this reason, the present work is a first attempt to investigate the flow and the acoustics of the generic side view mirror mounted on a half of a road vehicle at the Reynolds number of $Re = 5.2 \cdot 10^5$. As already cited, the work taken as reference in this study is the one of J. Ask and L. Davidson [2] which results are used to get a proper comparison with the ones proposed in the following sections.

4.1. Flow specifications

The flow travelling across the geometry is fully 3D turbulent and unsteady following the equations (1.1) and (1.2) and its free stream velocity is $U = 39m/s \approx 140\ km/h$ that corresponds to a value at which the aerodynamic noise becomes dominant. The kinematic viscosity is set to be $\nu = 1.5 \cdot 10^{-5}\ m^2/s$ and, together with the characteristic length of the side view mirror $D = 0.2\ m$ (see figure 4.4) , we obtain a Reynolds number of $Re_D = 5.2 \cdot 10^5$ with a density of $\rho = 1.225\ kg/m^3$.
Although the geometry is half of a vehicle, we concentrate on the side view mirror defining the Reynolds number based on this component while, from the acoustic point of view, we isolate its contribution on the overall sound generation and propagation.

4.2. Numerical setup

Similarly to what described in chapter 3 at section 3.2, the simulation is as follow: a converged RANS with a KOmegaSST turbulence model serves as an initial condition for the Detached Eddy Simulation approach implemented with the KOmegaSSTDDES modeling technique.
The simulation runs for a non-dimensional time $TU/D \approx 500$ with a time discretization of $\Delta TU/D = 2.925 \cdot 10^{-3}$ in order to have enough sampling data to correctly capture the phenomenon and to maintain the CFL constantly under 1. The used solver is the pimpleFOAM employing 3 corrector loops while the numerical schemes are the followings:

- 2^{nd} order backward scheme for temporal discretization;
- 2^{nd} order Gauss linearUpwindV scheme for the convection term while for k and $omega$ Gauss linearUpwind is chosen;
- 2^{nd} order linear scheme for the viscous term.

4.2.1. Computational domain

The geometry is placed inside a computational domain that extends for $44m$ along the stream wise direction and for $9m$ along the cross stream direction. In the span wise extension the far field boundaries are at a distance of $8m$ between each other. In figure 4.2 is possible to notice the interested side view mirror mounted on the vehicle, while in figures 4.3a and 4.3b its geometry is shown isolated from the car.

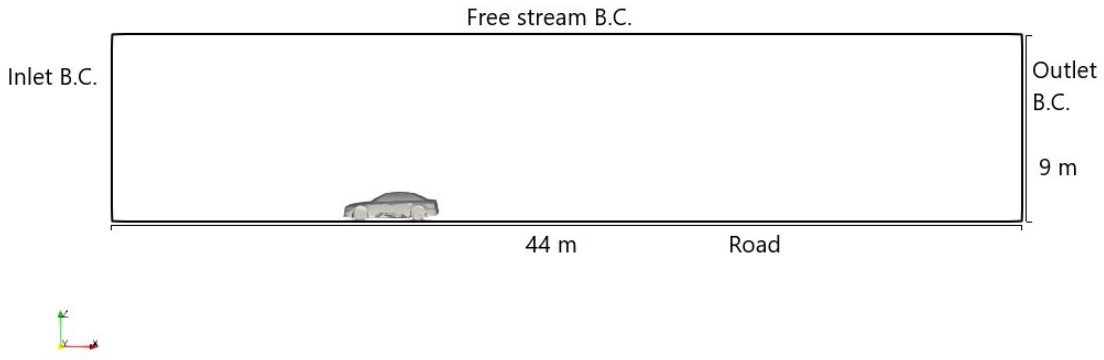

Figure 4.1: Computational domain for the automotive case in the x-z plane.

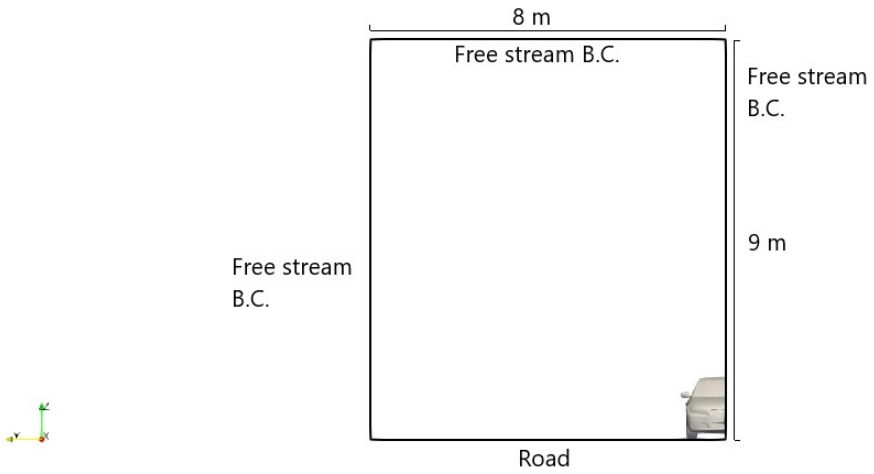

Figure 4.2: Computational domain for the automotive case in the x-y plane.

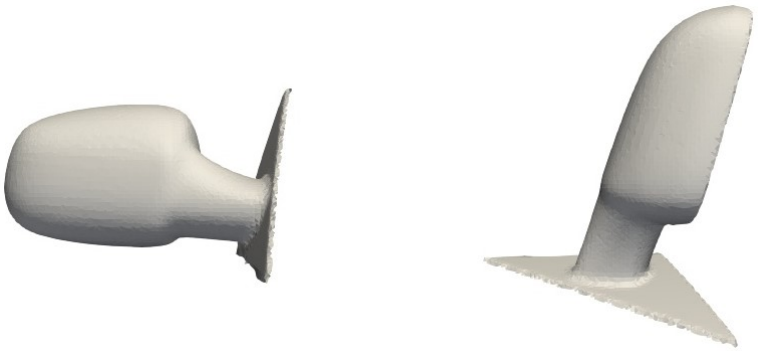

(a) Front view. (b) Top view.

Figure 4.3: Side view mirror geometry.

To choose the above mentioned Reynolds number it has been considered a simplified geometry of the side view mirror as shown in figure 4.4 taken from the paper of J.Ask and L.Davidson [2]. It consists of a half cylinder in top of which a quarter sphere is blunted.

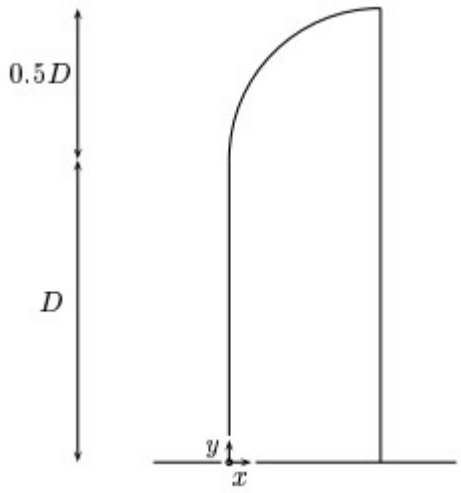

Figure 4.4: Simplified geometry of the generic side view mirror.

As it is possible to see from the figure, the characteristic length D is the height of the half cylinder.

4.2.2. Boundary conditions

As done for the other two cases, the boundary conditions are shown in the table below.

	p	U	k	ω	ν_t
Inlet	zeroGradient	fixedValue	fixedValue	fixedValue	zeroGradient
Outlet	fixedValue	zeroGradient	zeroGradient	zeroGradient	zeroGradient
Top	symmetry	symmetry	symmetry	symmetry	symmetry
Road	zeroGradient	fixedValue	wallFunction	wallFunction	wallFunction
Front	symmetry	symmetry	symmetry	symmetry	symmetry
Back	symmetry	symmetry	symmetry	symmetry	symmetry
Car	zeroGradient	noSlip	wallFunction	wallFunction	wallFunction

Table 4.1: Boundary conditions for the side view mirror test case.

The velocity of the road patch is set (fixedValue from table 4.1) equal to the velocity of the free stream flow in order to simulate the movement of the vehicle.

4.2.3. Mesh

The grid for this case is constructed using the tool *snappyHexMesh* present in OpenFOAM.
With this strategy is possible to adopt several levels of refinement for the different components of the vehicle. In our study we set a coarser grid in the area of the detailed underbody while the highest level of refinement is obtained for the side view mirror (see figure 4.5 and 4.6). This choice has been made considering the quality of the mesh and that the flow passing under the vehicle is not affecting the one crossing the upper part of the car, hence permitting bigger cell dimensions.

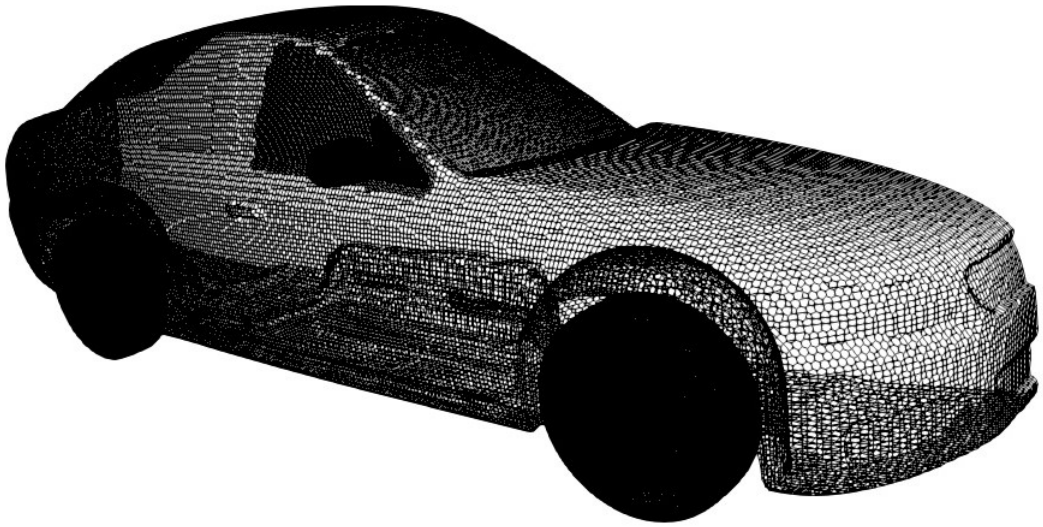

Figure 4.5: Grid resolution for the half vehicle geometry.

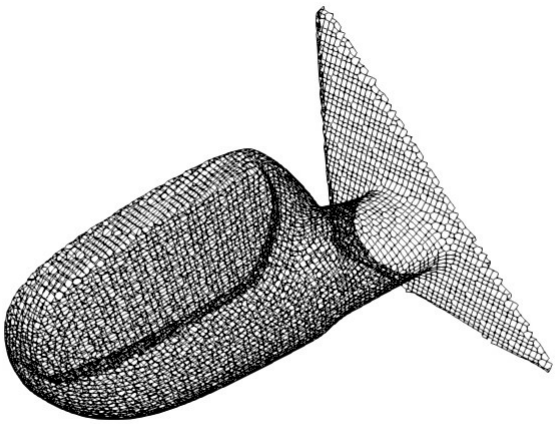

Figure 4.6: Grid resolution for the side view mirror.

Three set of layers are used to reach the desired value of y^+ in order to correctly cope with the wall functions adopted in the near wall regions. The maximum and mean value of non-dimensional distance from the wall for the side view mirror are respectively: $y^+_{max} = 122.18$ and $\overline{y^+} = 32.38$.

4.3. Results and discussion

In the next paragraph the results of the CFD simulation and the acoustic part are described. The model used to predict the noise is still the aeroacoustic Curle's analogy implemented in OpenFOAM.

4.3.1. RANS Flow characteristics

The first results are related to the Reynolds Averaged simulation because the aim is to get the steady state values of the field variables in the whole domain and use them to initialize the 3D DES.

(a) Velocity field in the computational domain.

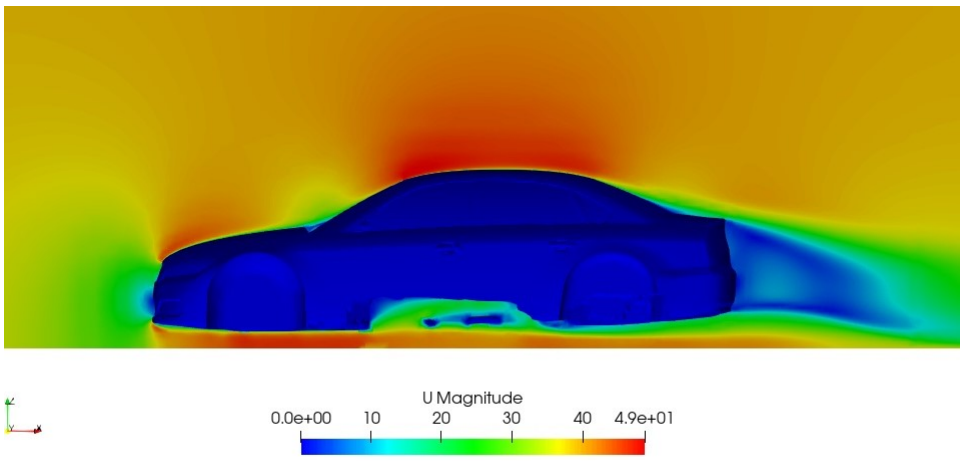

(b) Velocity field around the vehicle.

Figure 4.7: Velocity field of the RANS side view mirror test case in the x-z plane.

The velocity field can be visualized in figure 4.7 while the pressure acting on the geometry is shown in figure 4.8.

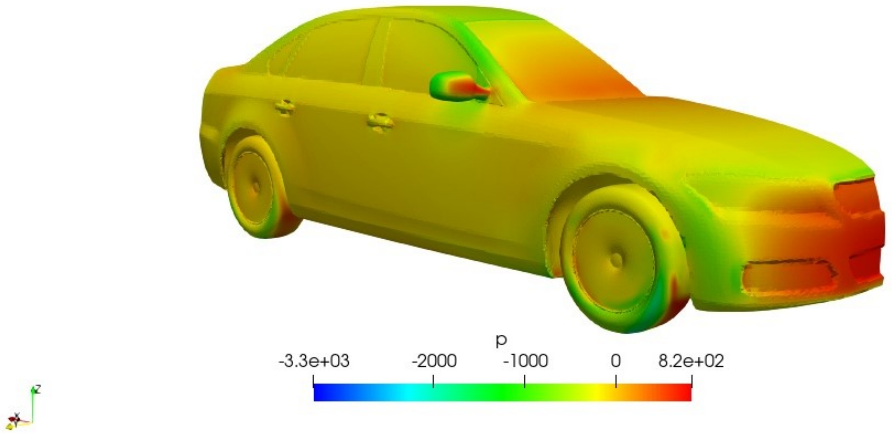

Figure 4.8: Pressure acting on the surface of the vehicle geometry in the RANS configuration.

Since the focus of this test case is on the side view mirror we can look at its aerodynamics coefficients to have the proof that the simulation is converged correctly.

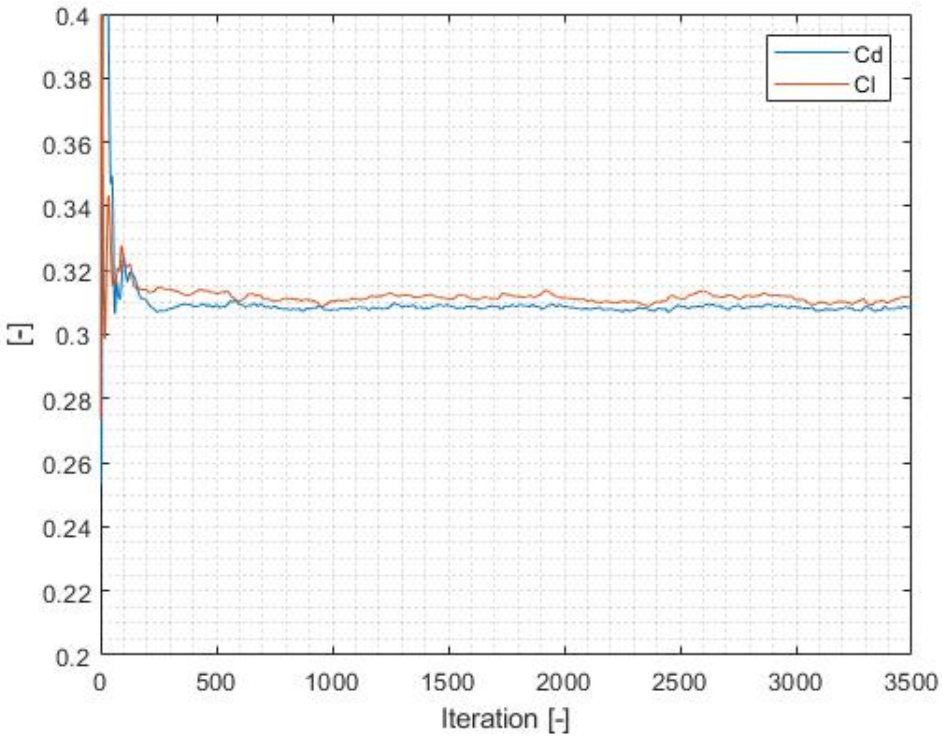

Figure 4.9: Aerodynamic coefficients of the side view mirror in the RANS configuration.

4.3.2. LES Flow characteristics

In this paragraph it is analyzed the CFD results of the Detached Eddy Simulation where the quantities are time dependent permitting to have turbulent eddies that detach from the geometry.

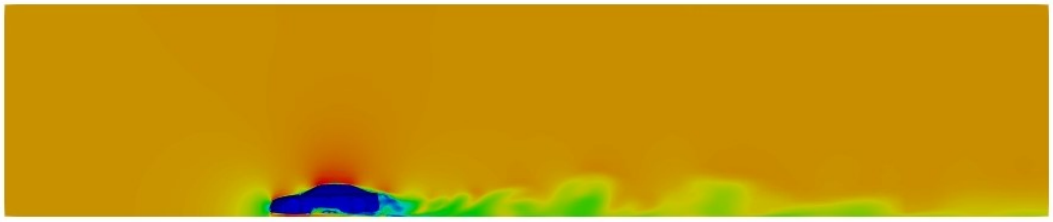

(a) Velocity field in the computational domain.

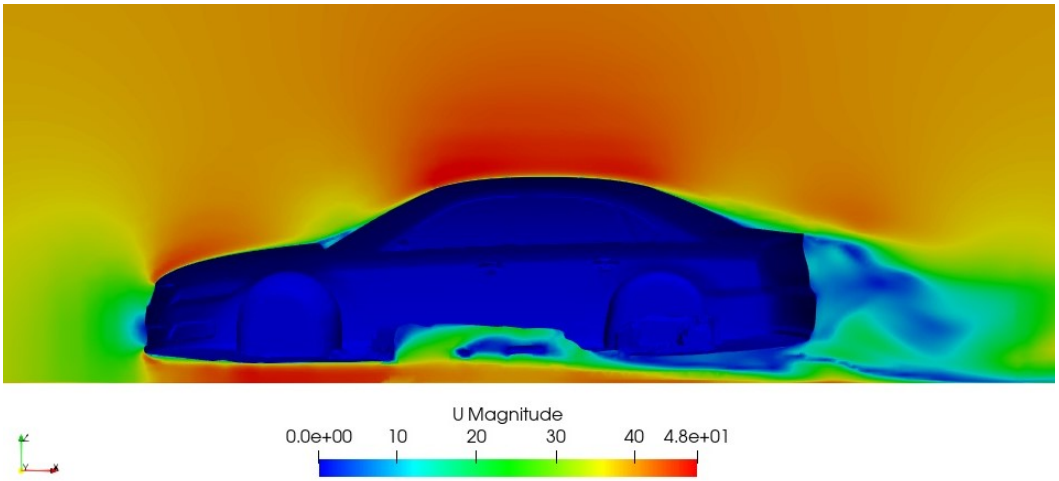

(b) Velocity field around the vehicle.

Figure 4.10: Instantaneous velocity field of the DES automotive case in the x-z plane at $TU/D = 497.25$.

In figure 4.10a is shown the instantaneous velocity field of the entire domain while figure 4.11 shows the vorticity magnitude of the vehicle pointing out the three dimensionality of the flow.

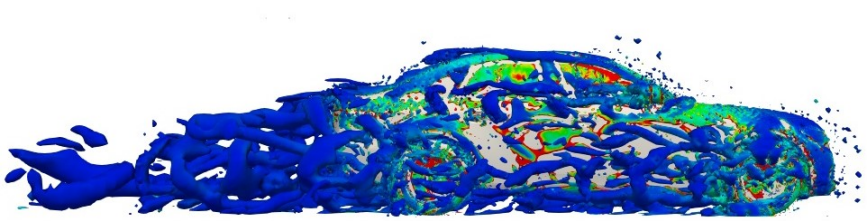

(a) View of the x-z plane.

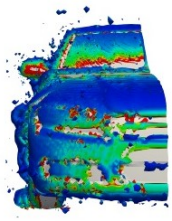

(b) View of the y-z plane.

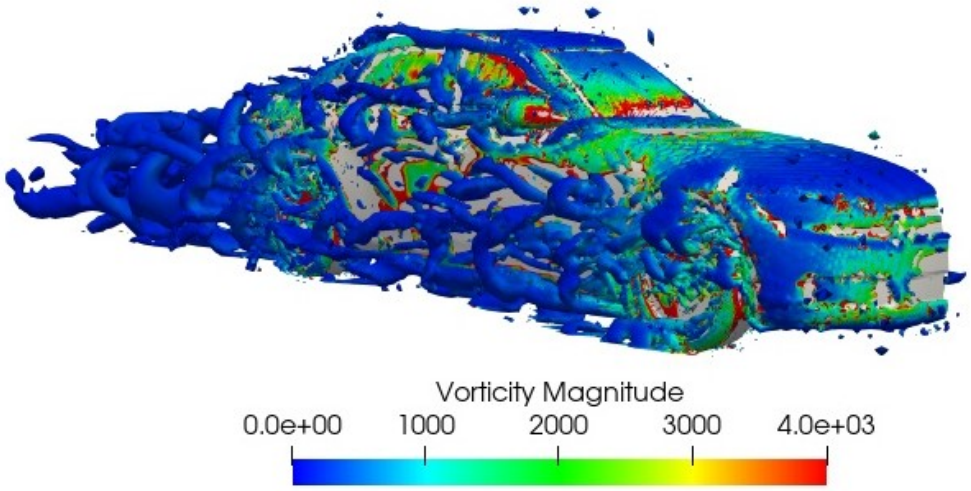

(c) 3D representation of the geometry.

Figure 4.11: Vorticity magnitude of the automotive test case plotted over vorticity contours at $TU/D = 497.25$.

The main sources of vortices are represented by the tires and the side view mirror which are also the main sound sources. As already mentioned, in this thesis the focus is on the noise emitted from the side mirror component.
In figure 4.12 is instead represented the distribution of the pressure around the surface of the vehicle highlighting an high pressure zone in the front part of the vehicle. In particular, by comparing the front bumper on figures 4.10 and 4.12, the Bernoulli equation shows that pressure is inversely related to velocity. In other words, high velocity creates a low pressure area while low velocity generates an high pressure area. This permits to the flow to accelerate on the upper part of the vehicle detaching towards the end and generating the vortices represented in the above figure.

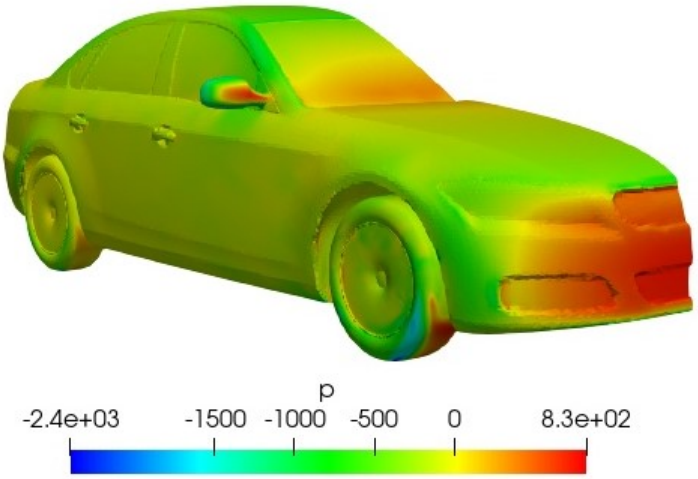

Figure 4.12: Pressure acting on the surface of the vehicle geometry in the DES configuration at $TU/D = 497.25$.

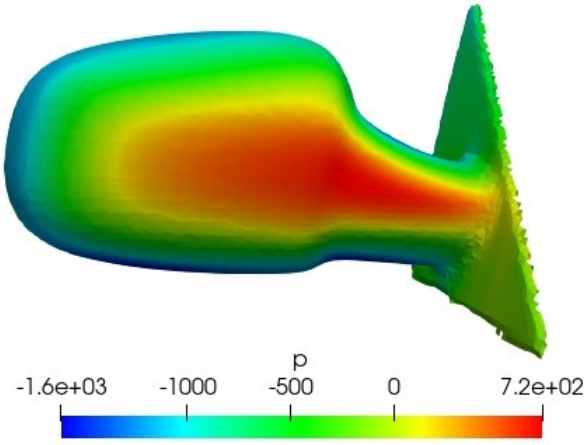

Figure 4.13: Pressure acting on the side view mirror in the DES configuration at $TU/D = 497.25$.

Concerning the distribution of the pressure on the side view mirror shown in figure 4.13 we can appreciate the high pressure zone on the part directly exposed to the flow and the low pressure area in the wake where the majority of the vortices arise. Starting from the pressure distribution shown in the above figures we can derive the aerodynamic coefficients of the side view mirror and the entire vehicle which time histories are shown respectively in figure 4.15 and 4.14.

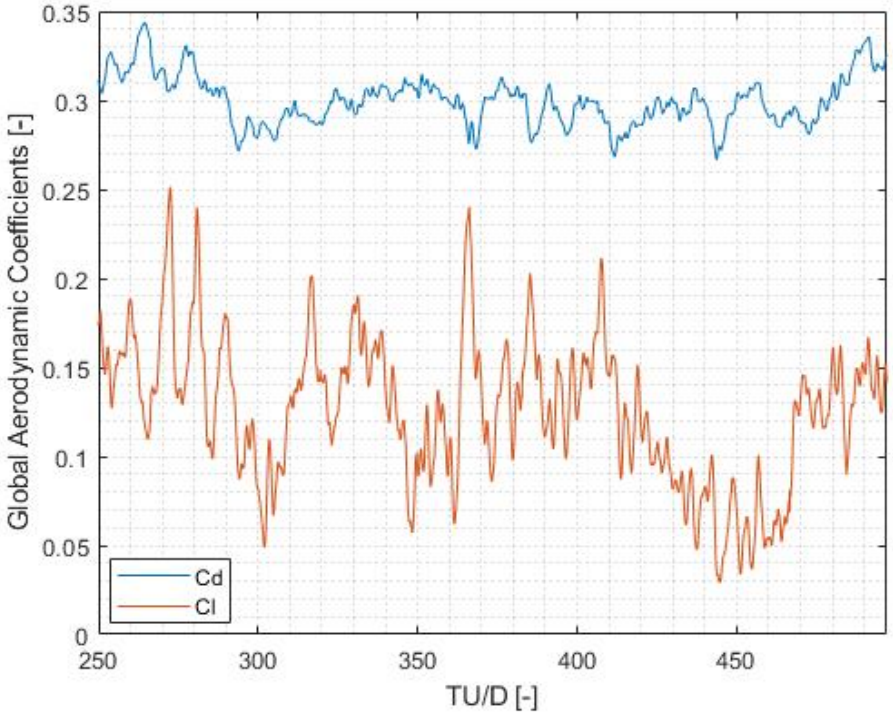

Figure 4.14: Time histories of drag and lift coefficient for the entire vehicle.

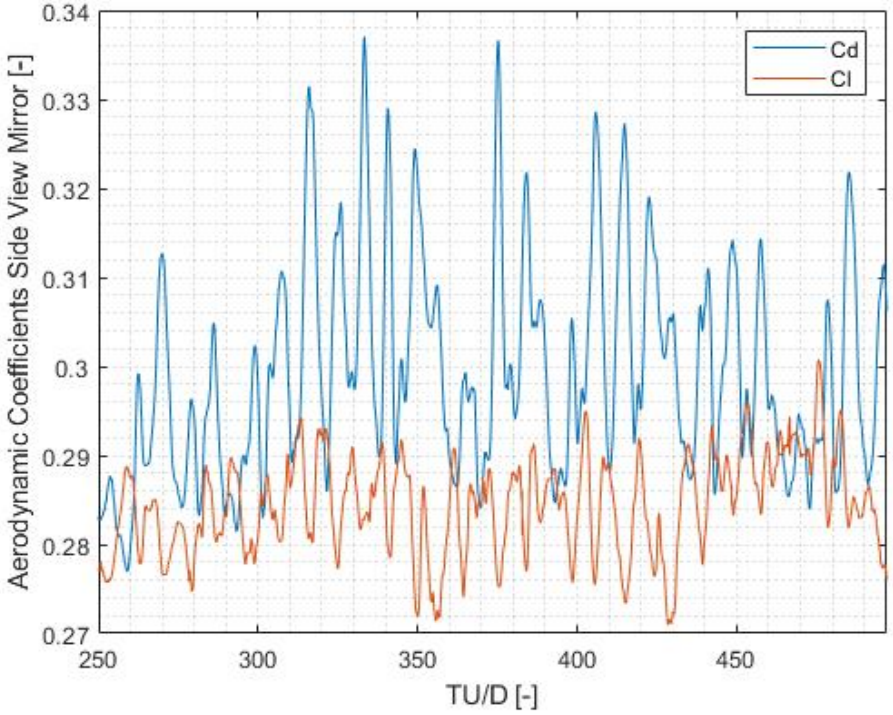

Figure 4.15: Time histories of drag and lift coefficient for the side view mirror.

The time window in which the sampling is performed starts at a non dimensional time of $TU/D = 250$ and ends at $TU/D = 497.25$. This time range is wide enough to get a proper representation of the physics involved in the simulation obtaining a mean drag coefficient, derived from the time history in figure 4.14, equal to $\overline{c_d} = 0.293$. Considering that for the same geometry of the vehicle used in this test case the value of mean drag is $\overline{c_d} = 0.285$ we are in good agreement with the literature [34]. Furthermore, by digging more into the components of the vehicle we can have a comparison in the following table of the fluid dymanic parameters obtained on the side view mirror with the ones proposed by Ask and Davidson [2].

Previous Studies	St	Cl_{rms}	Cd_{mean}
J. Ask and L. Davidson [2]	≈ 0.2	–	0.428
Present work	≈ 0.123	0.284	0.299

Table 4.2: Comparison of the results with the paper of J. Ask and L. Davidson [2].

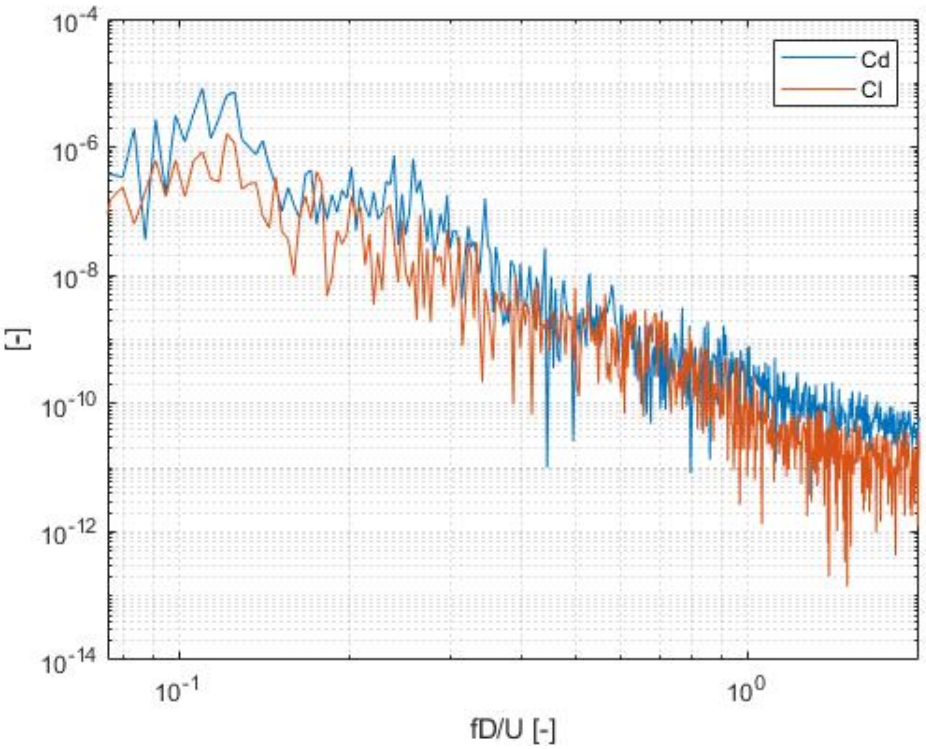

Figure 4.16: Power Spectral Density of the aerodynamic coefficients of the side view mirror.

By looking at the table 4.2 we notice that the mean drag coefficients are quite different one from the other. This is not an unexpected result because the two side view mirror geometries are not completely equal between each other and, furthermore, in our test case is present also half of the body of the vehicle that is not considered in the reference paper of J.Ask and L.Davidson [2] that may cause some differences in the air flow passing over the side mirror. Infact, the dominant frequency is qualitatively detected in figure 4.16 but is not quantitatively the same of the one proposed by J.ASk and L.Davidson [2] because the periodicity of the vortices shedded from the geometry is different. Furthermore, It is no more possible to clearly distinguish the dominant frequency of the drag from the one of the lift as done in the previous test cases because the flux is not perfectly normal to the surface of the side view mirror. All these issues will impact also on the noise generation and propagation as we'll describe in the next paragraph.

4.3.3. Acoustics

The acoustic analysis has been made on the basis of the same Curle's aeroacoustic analogy already used for the previous test cases. The noise emission and propagation study is done focusing on the side view mirror as acoustic source neglecting the rest of the vehicle components.
With the aim of comparing the acoustic results with the ones proposed by J.Ask and L.Davidson [2] we firstly concentrate on the sound generation and propagation in the near field. To do so we placed 4 probes as shown in figure 4.17 predicting for each one the acoustic pressure perturbations by using the Curle's analogy implemented in OpenFOAM.

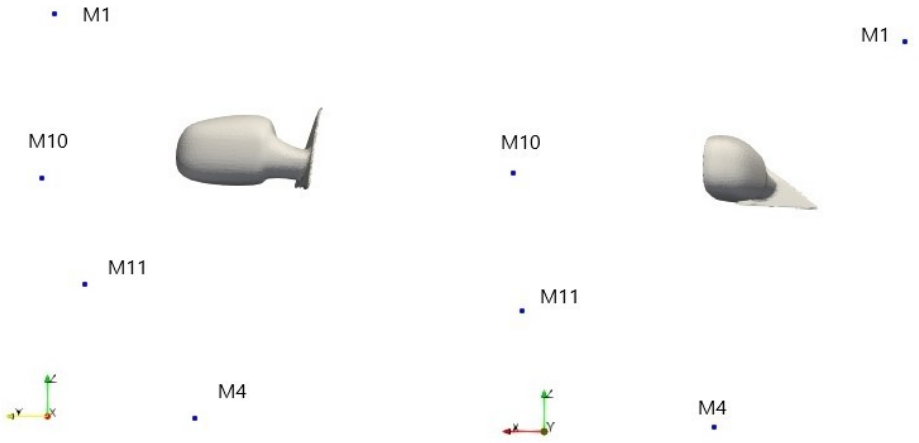

(a) View of the y-z plane. (b) View of the x-z plane.

Figure 4.17: Position of the probes in the near field for the side view mirror test case.

Then, starting from the acoustic oscillations and doing a spectral analysis we obtained the SPL measured in dB against the frequency as shown in figure 4.18. We can appreciate that the dominant frequency is the same already highlighted in figure 4.16.

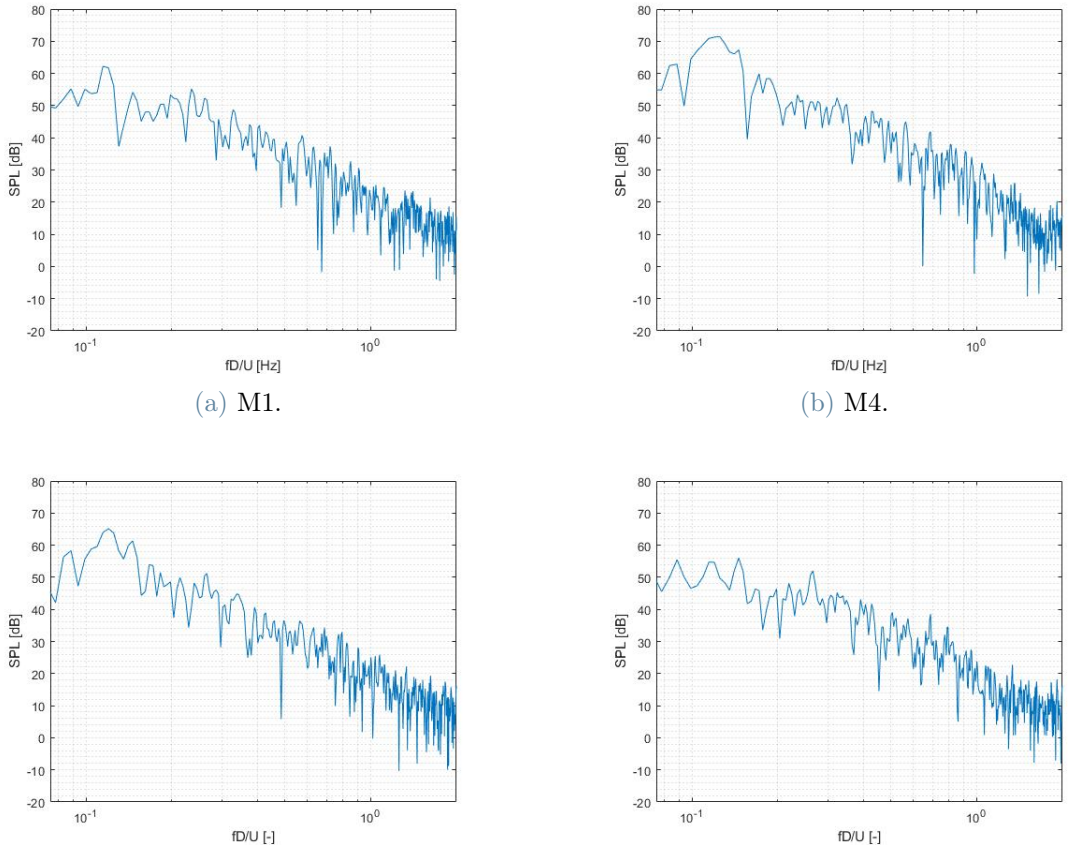

(a) M1. (b) M4.

(c) M10. (d) M11.

Figure 4.18: Sound Pressure Level measured at different probes positions in the far field.

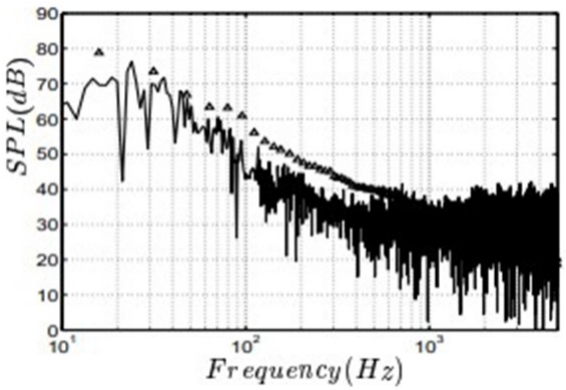

Figure 4.19: Sound Pressure Level measured at the probe M10 in the reference of J.Ask and L.Davidson [2].

Quantitatively speaking the intensity of the sound measured at the above mentioned positions is similar to the one proposed in the paper of J.Ask and L.Davidson [2] in figure 4.19 because the aeroacoustic model implemented is the same except for the viscous forces that we are neglecting in this thesis. Other aspects that differ from the paper and have an impact on the acoustic results are the different geometry of the side view mirror and the presence of half of the vehicle that generate a different structure and periodicity in the vortices. Those two contributions make the predicted sound intensity slightly lower with respect to the one of J.Ask and L.Davidson [2].
The far field acoustics is analyzed by predicting the pattern of the noise propagation emitted from the side view mirror. As done for the previous cases we placed 45 probes along a circumference of radius $75D$ in the x-y plane centered in the acoustic source. Figure 4.20 shows the positions of the probes.

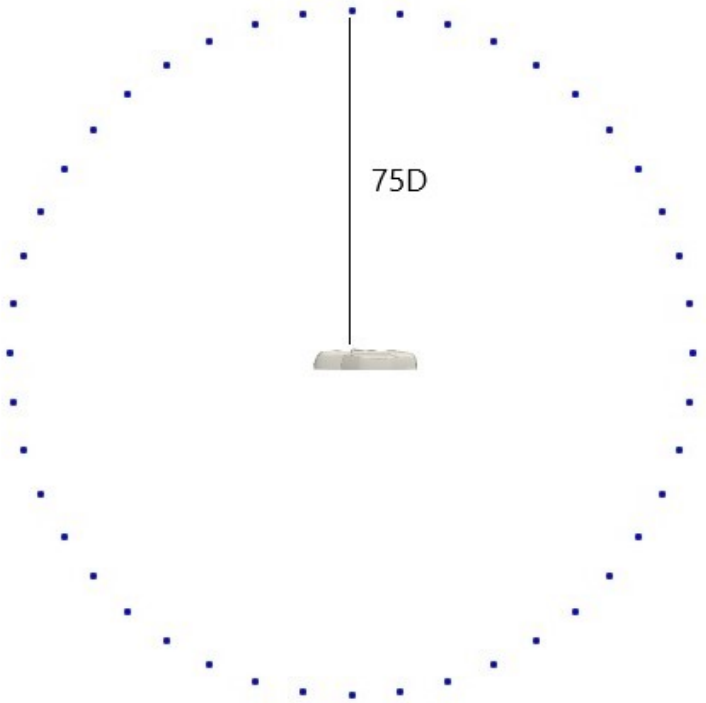

Figure 4.20: Probes position in the far field in the x-y plane.

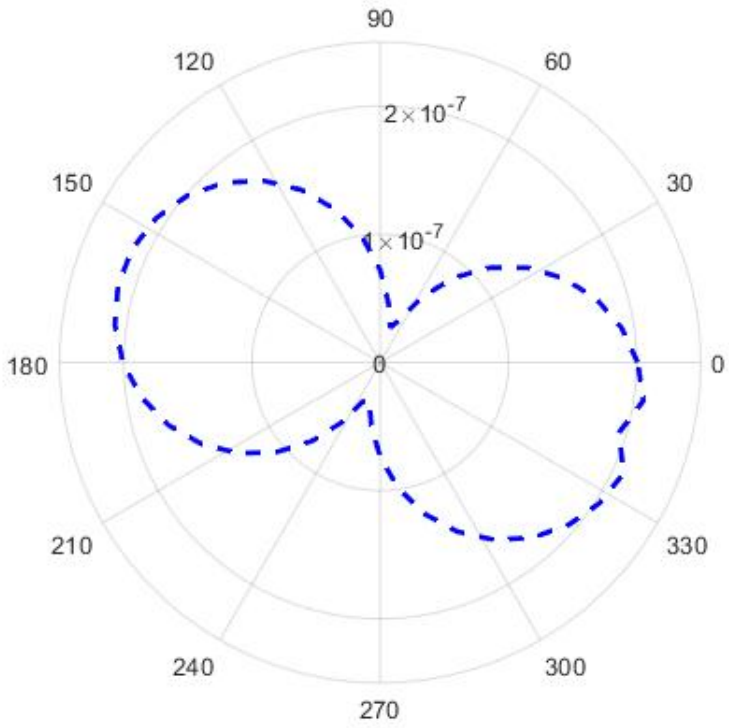

Figure 4.21: Directivities of root mean square sound pressure ($\widetilde{P}_{rms} = p'_{rms}/(\rho U^2)$) at the Strouhal frequency obtained using the Curle's analogy implemented in OpenFOAM for side view mirror test case.

Figure 4.21 shows that the dipole is not perfectly vertical as in the previous cases. This is due to the fact that the flow is no more perfectly normal to the surface of the acoustic source and this generates the rotated shape shown in the figure above. Furthermore, the contribution of the drag at the same frequency is now much more present and in the same order of magnitude of the one of the lift. These two considerations combined together contribute to the rotation of the dipole with respect to the vertical axis.
To complete the acoustics study on this particular case we derived also the decay of the noise emitted by placing 75 probes every $2D$ progressively further from the acoustic source. Also in this case we took the p'_{rms} value at the dominant frequency for each probe.

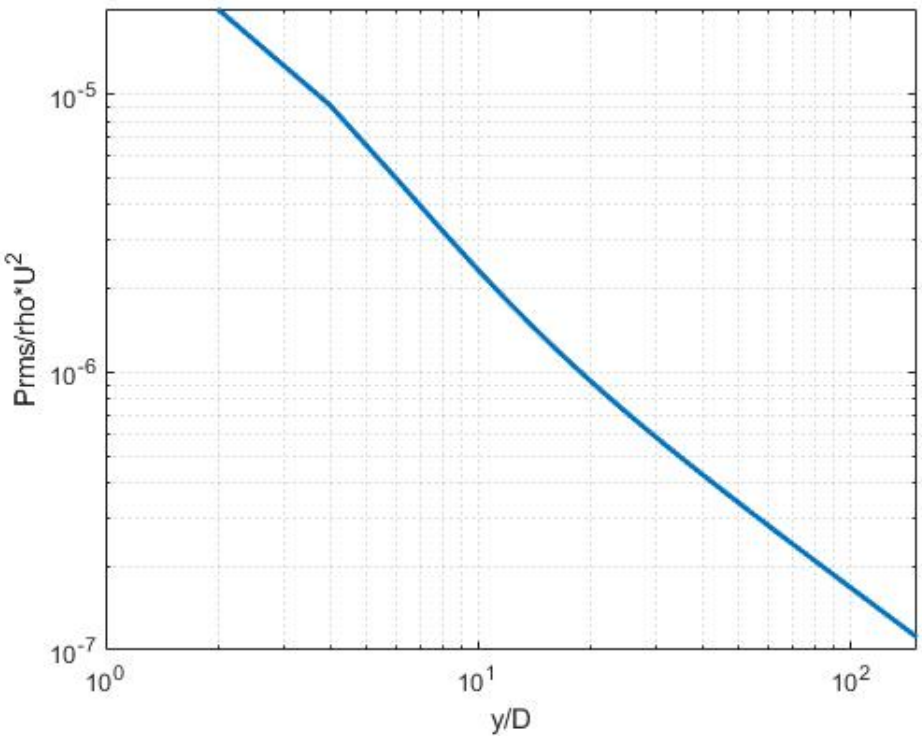

Figure 4.22: Decay of root mean square sound pressure ($\widetilde{P}_{rms} = p'_{rms}/(\rho U^2)$) at the Strouhal frequency obtained using the Curle's analogy implemented in OpenFOAM for side view mirror test case.

By looking at the figure 4.22 we can appreciate that the noise is reducing by getting further away from the side view mirror.
In conclusion, for this particular case the semplifications implemented in the aeroacoustic model are coherent with the ones proposed in the reference paper of J.Ask and L.Davidson [2]. This coherence can be seen also on the proposed results, in particular in the SPL shown in figure 4.18.

5 | Conclusions and future developments

The minimization of the noise emissions in the automotive field is of huge importance for a proper comfort assessment of the driver and the passengers. This is highlighted nowadays because the number of the hybrid and electric vehicles travelling on the roads are continuously growing. Thus the dominant component of the sound at high speed ($> 120\ km/h$) is the aerodynamic one. Starting from this requirement, three different cases have been tested predicting the noise emission and propagation in the far field by employing the Curle's aeroacoustic analogy implemented in OpenFOAM. The final aim is to validate this model and provide a straightforward methodology to predict the radiated sound. The Curle's model has been used to extract the directivity, represented by the dipole, the decay and the intensity of the noise measured in SPL for all the three above mentioned applications.

The main advantage of this model is its simplicity of usage since it is directly incorporated into an OpenFOAM's function and it allows a fast postprocessing on the flow simulation. It also gives results that are qualitatively correct for all the three tested cases. Chapter 2 describes the laminar square cylinder test case, the Curle's analogy predicts correctly the dipole nature of the radiated sound and its decay is described by moving further from the source. The detected dominant frequency is the same as the one of the reference of Ali et. al [1]. On chapter 3 we investigated the noise induced by the BARC, a well documented fluid dynamic benchmark. After validating the flow field, we employed the Curle's analogy to predict the radiated sound noise. Also in this case it is possible to appreciate the correct prediction of the directivity and the decay highlighting the reliability of the model also in turbulent flow conditions. The Sound Pressure Levels measured at different probes in the far field highlights a peak at the correct dominant frequency predicted also in the fluid-dynamic part. In chapter 4, we applied the Curle's aeroacoustic analogy to an automotive case, focusing our attention on the noise induced by the side view mirror. The obtained dipole is detected pointing out also a rotation due to the fact that the acoustic source, i.e. the side view mirror, is not perfectly normal to the flow.

Furthermore, the SPL obtained for this application are comparable with the ones of the J.Ask and L.Davidson reference [2] which employs the same model except for the viscous forces that we are neglecting. All These results are really important to give an initial understanding of the phenomenon.
On the other hand, the obtained results are not in total agreement with the literature pointing out some important limits in the model. The first limit is that the OpenFOAM Curle's aeroacoustic analogy does not consider the retarded time in the noise prediction, leading to an instantaneous propagation of the sound as seen in figure 2.6. This cannot permit to correctly visualize the sound pressure waves and the dipole since the velocity of propagation of the noise from the source to the observer is instantaneous. The model also neglects the volume source of the sound constituting the second big limit of the Curle's aeroacoustic analogy implemented in OpenFOAM. Although this assumption is valid for $Re = 150$, it might fail for the BARC case and definitely it is not valid on the side view mirror test case. Both these limits lead to a non conformity with the data available in literature and they represent the main drawbacks of the model, since we expect that a lot of the induced noise by the side view mirror is generated by the turbulence behind the mirror itself. Although the simplicity of the model introduces inaccuracies, it is still able to provide a proper qualitative understanding of the acoustic phenomenon.
In conclusion we can say that that the Curle's aeroacoustic analogy taken into consideration in this thesis work provides a good methodology to give an initial guess of the noise emission and propagation but needs further improvements to be completely accurate and reliable. Despite the model is relatively simple and easy to use being implemented in OpenFOAM, it is also qualitatively reliable and provides a good understanding of the acoustics.

5.1. Future developments

The future works will be based on the modification of the already existing Curle's analogy in OpenFOAM with the aim to make it much more accurate by adding the contributions of the retarded time and the volume source. By doing so, sampling the results on a plane as done in figure 2.6 would result in appreciating the peaks of the travelling acoustic wave. We also plan to extend the work here proposed by focusing on the side view mirror test case, employing the current methodology to develop noise reduction solution. Moreover, in order to achieve reasonable results for the laminar flow around the square cylinder it would be better to employ a 2D Green function rather than the usual 3D Green function.

Bibliography

[1] M. S. M. Ali, C. J. Doolan, and V. Wheatley. The sound generated by a square cylinder with a splitter plate at low reynolds number. 04 2011.

[2] J. Ask and L. Davidson. The near field acoustics of a generic side mirror based on an incompressible approach. *Fluid Dynamic Center - VOLVO CAR CORPORATION, Göteborg, Sweden*, 2005.

[3] L. Bruno, D. Fransos, N. Coste, and A. Bosco. 3d flow around a rectangular cylinder: A computational study. *Journal of Wind Engineering and Industrial Aerodynamics*, 98, 11 2009.

[4] L. Bruno, M. Salvetti, and F. Ricciardelli. Benchmark on the aerodynamics of a rectangular 5:1 cylinder: an overview after the first four years of activity. 2014.

[5] J. Delfs. *Grundlagen der aeroakustik*. Technische Universität Braunschweig - Institut für Aerodynamik und Strömungstechnik Abteilung Technische Akustik, DLR – Deutsches Zentrum für Luft - und Raumfahrt e.V., Lilienthalplatz 7, 38108 Braunschweig, Germany, 10 2016.

[6] W. Dobrzynski. Zur bedeutung von strömungswechseldrücken auf der karosserieoberfläche für den innenlärm von personenkraftfahrzeugen. *Berlin, Technische Universität, Dissertation*, 1983.

[7] C. Doolan. Flat-plate interaction with the near wake of a square cylinder. *AIAA Journal*, 47, 2009.

[8] M. F. Hannes and C. Munz. Direct aeroacoustic simulation of acoustic feedback phenomena on a side-view mirror. *Journal of Sound and Vibration*, 2016.

[9] M. Helfer. General aspects of vehicle aeroacoustic. *Research Institute of Automotive Engineering and Vehicle Engines, Stuttgart*, 2005.

[10] A. Hirschberg and S. Rienstra. An introduction to aeroacoustics. 1823, 08 2004.

[11] R. Höld, A. Brenneis, and A. Eberle. Numerical simulation of aeroacoustic sound

generated by generic bodies placed on a plate: Part i - prediction of aeroacoustic sources. *In* 5^{th} *AIAA/CEAS Aeroacoustics Conference. Seattle, Washington*, 1999.

[12] M. S. Howe. Theory of vortex sound. *Cambridge texts in Applied Mathematics*, 2003.

[13] H. C. Hsieh. Tyre aeroacoustics using hybrid cfd/caa methods. *Politecnico di Milano, Scuola di ingegneria industriale e dell'informazione*, 2021.

[14] $https://ec.europa.eu/environment/noise/indexen.html$.

[15] $https://mechanics.stackexchange.com/questions/24852/what-is-an-apillar$.

[16] $https://www.researchgate.net/figure/Vortex-Shedding-Across-aCylindrical-Bodyfig1260263818$.

[17] $https://www.scirp.org/(S(351jmbntvnsjt1aadkozje))/reference/referencespapers.aspx?referenceid=1665646$.

[18] O. Inoue, W. Iwakami, and N. Hatakeyama. Aeolian tones radiated from flow past two square cylinders in a side-by-side arrangement. 04 2006.

[19] V. Korchagova, M. Kraposhin, and S. Strizhak. Computational aeroacoustics methods with openfoam v. 1812. 2019.

[20] S. Lele. Computational aeroacoustics - a review. *35th Aerospace Sciences Meeting and Exhibit, Reno,NV,U.S.A.*, 2012.

[21] C. Mannini and G. Schewe. Numerical study on the three-dimensional unsteady flow past a 5:1 rectangular cylinder using the des approach. *Proceedings of the thirteenth International Conference on Wind Engineering, Amsterdam, The Netherlands*, 2011.

[22] M. Marelli. Adjoint-based shape optimization for noise reduction of a wheel. *POLITECNICO DI MILANO, Scuola di Ingegneria Industriale e dell'Informazione, Corso di Laurea Magistrale in Ingegneria Aeronautica*, 2021.

[23] I. Mazzieri, M. Stupazzini, R. Guidotti, and C. Smerzini. Speed: Spectral elements in elastodynamics with discontinuous galerkin: a non-conforming approach for 3d multi-scale problems. *Int. J. Numer. Meth. Eng.*, 12, 2013.

[24] W. Möhring. On vortex sound at low mach number. *Journal of Fluid Mechanics, 85:685 - 691*, 1978.

[25] C. Norberg. Flow around rectangular cylinders: pressure forces and wake frequencies. *Journal of Wind Engineering and Industrial Aerodynamics*, 49, 1993.

[26] A. Okajima. Strouhal numbers of rectangular cylinders. *Journal of Fluid Mechanics*, 123, 1982.

[27] O. Phillips. The intensity of aeolian tones. *Journal of Fluid Mechanics*, 6, 1956.

[28] P. Pivetta. Simulazione aero acustiche: propagazione del suono da una sorgente sonora aerodinamica. Master's thesis, Politecnico di Milano, 2015.

[29] A. Powell. Theory of vortex sound. *Journal of the Acoustic Society of America, 36(1):177 - 195*, 1964.

[30] A. Ribeiro. Unsteady rans modelling of flow past a rectangular 5:1 cylinder: investigation of edge sharpness effects. *Proceedings of the thirteenth International Conference on Wind Engineering, Amsterdam, The Netherlands*, 2011.

[31] E. Ringwall. Aeroacoustic sound sources around the wheels of a passenger car. a computational fluid dynamics study using steady state models to evaluate main sources of flow noise. Master's thesis, Chalmers university of technology, SE-412 96 Göteborg, Sweden, 2017.

[32] T. Rung, D. Eschricht, J. Yan, and F. Thiele. Sound radiation of the vortex flow past a generic side mirror. *In 8^{th} AIAA/CEAS Aeroacoustics Conference. Breckenridge, Colorado*, 2002.

[33] S. Schoder and M. Kaltenbacher. Hybrid aeroacoustic computations: state of art and new achievements. *Journal of theoretical and computational acoustics*, 27(4), 2019.

[34] F. F. Semeraro and P. Schito. Numerical investigation of the influence of tire deformation and vehicle ride height on the aerodynamics of passenger cars. *Fluids*, 7(2), 2022.

[35] R. Siegert, V. Schwartz, and J. Reichenberger. Numerical simulation of aeroacoustic sound generated by generic bodies placed on a plate: Part ii - prediction of radiated sound pressure. *In 5^{th} AIAA/CEAS Aeroacoustics Conference. Seattle, Washington*, 1999.

[36] E. Sjöberg. Implementation of aeroacoustic methods in openfoam. 2016.

[37] A. Sohankar, C. Norberg, and L. Davidson. Low-reynolds number flow around a square cylinder at incidence: study of blockage, onset of vortex shedding and outlet boundary condition. *International Journal of Numerical Methods in Fluids*, 26, 1998.

[38] A. Sohankar, C. Norberg, and L. Davidson. Simulation of three-dimensional flow around a square cylinder at moderate reynolds numbers. *Physics of Fluids*, 2, 1999.

[39] P. R. Spalart. Detached-eddy simulation. *Annual Review of Fluid Mechanics*, 41(1): 181–202, 2009.

[40] M. Strelets. Detached-eddy simulation of massively separated flow. *39th Aerospace sciences meeting and exhibit*, 2001.

[41] T. Tamura, T. Miyagi, and T. Kitagishi. Numerical prediction of unsteady pressures on a square cylinder with various corner shapes. *Journal of Wind Engineering and Industrial Aerodynamics*, 1998.

[42] Z. Wei and A. Kareem. A benchmark study of flow around a rectangular cylinder with aspect ratio 1:5 at reynolds number 1.e5. *In: Proceedings of the thirteenth International Conference on Wind Engineering, Amsterdam, The Netherlands.*, 2011.

[43] C. Williamson. Vortex dynamics in the cyilinder wake. *Annual review of fluid mechanics*, 28, 1996.

List of Figures

List of Tables

List of Symbols

Variable	Description	SI unit
Re	Reynolds number	[-]
Ma	Mach number	[-]
St	Strouhal number	[-]
ρ	Density	$[kg/m^3]$
u	Instantaneous velocity	$[m/s]$
u'	Fluctuating velocity	$[m/s]$
U	Mean velocity	[-]
τ	Viscosity stress	$[Pa]$
δ	Dirach delta	[-]
D	Characteristic length	$[m]$
p	Pressure	$[Pa]$
p'	Acoustic pressure	$[Pa]$
k	Turbulent kinetic energy	$[m^2/s^2]$
ω	Specific dissipation rate	$[1/s]$
ν	Physical kinematic viscosity	$[m^2/s]$
μ	Physical dynamic viscosity	$[Pa \cdot s]$
ϕ	Generic variable	[-]
Δ	Cell length	$[m]$
d	Turbulent length scale	$[m]$
λ	Wavelength	$[m]$

Variable	Description	SI unit
c_0	Speed of sound	$[m/s]$
T	Time	$[s]$
ΔT	Time step	$[s]$
f	Frequency	$[s]$
S	Surface	$[m^2]$
Ti	Turbulence intensity	[-]
α	Incidence angle	$[deg]$
$\overline{y+}$	yPlus	[-]

Acknowledgements

First of all I would like to thank professor Paolo Schito that gave me the opportunity to do this thesis work in the field of aeroacoustics. Furthermore, I would like to thank PhD. candidates Alberto Artoni and Francesco Fabio Semeraro for their huge help and availability in giving prompt feedbacks with their knowledge in every kind of problem that I had to face.
Finally, I would like to thank my family and my girlfriend Cristina for their continuous support during my entire education even in the darkest periods, my university colleagues and my friends.